Aus dem: *Institute of Lung Biology and Disease (Helmholtz Zentrum München)*

Dissertation

zum Erwerb des Doctor of Philosophy (Ph.D.) an der

Medizinischen Fakultät der

Ludwig-Maximilians-Universität zu München

Bridging gaps between in vitro and in vivo data in pulmonary aerosol delivery with focus on pharmacokinetics

vorgelegt von:

Sezer Orak

aus:

Deggendorf

Jahr:

2021

Mit Genehmigung der Medizinischen Fakultät der

Ludwig-Maximilians-Universität zu München

First evaluator (1. TAC member):	*Priv. Doz. Dr. med. Anne Hilgendorff*
Second evaluator (2. TAC-member):	*apl. Prof. Dr. Markus Rehberg*

Dean:	**Prof. Dr. med. Thomas Gudermann**

date of the defense:

21st October 2021

Table of Content

Summary

Pulmonary aerosolized delivery of drugs incorporated into nanocarriers (nanodrugs) by inhalation is a promising route for the prolonged treatment of lung diseases such as pulmonary hypertension or lung rejection after transplantation. Due to the lack of validated *in vitro* testing systems, the PK and efficacy of nanodrugs during the preclinical phase of drug testing has to be measured in animal models.

This work investigates the particokinetics of two nanodrugs, Ptx-NP and L-CsA, which incorporate the active drug Paclitaxel (Ptx) and Cyclosporine A (CsA) into polymeric or liposomal nanocarriers, respectively. The goal of the study was to evaluate the potential of aerosolized drug delivery combined with physiological *in vitro* cell culture models of the lung to predict the clinical outcome with a focus on PK.

The VITROCELL® Cloud 6 system was used to deliver the nanodrugs in aerosolized form to *in vitro* models of the healthy and diseased human alveolar air-blood barrier cultured at air-liquid interface (ALI) conditions, and to analyze the transbarrier transport of the incorporated drugs. ALI conditions showed a direct cell-nanodrug interaction, which allowed clarifying cellular uptake mechanisms (caveolae-mediated endocytosis and passive diffusion) and mirroring real cellular transport rates. In a direct comparison between the healthy and diseased models, no significant differences in the transbarrier transport rates were found, which highlight the prolonged tissue-association of drugs incorporated in nanocarriers. The obtained particokinetics were further combined with physiological-based PK (PBPK) modeling to predict the PK profile of CsA and Ptx (e.g. maximum drug concentration c_{max} in the blood; time until c_{max} is reached (t_{max})) after inhalation. This confirmed that c_{max} levels after inhalation were achieved fast (< 0.25 h). Moreover, the modeling revealed that c_{max} levels after inhalation are typically low, which highlights the advantage of targeting lung diseases by inhalation therapy as this avoids high drug levels in the blood that could lead to systemic toxicities.

Besides the PK, the efficacy of Ptx-NP was investigated. The analysis of Ptx doses in different compartments of the *in vitro* model demonstrated a cell-association of 30% of the initial dose 24 h after the aerosolized delivery of Ptx-NP. Accordingly, the potential of prolonged drug interaction with the diseased tissue *in vitro* could be highlighted. Moreover, a dose of 0.7 µg Ptx/cm² increased FoxO1 transcription – a hallmark of pulmonary hypertension - by a factor of 3 as compared to untreated control.

Consequently, the aerosolized drug delivery to ALI cell culture models of the alveolar tissue barrier combined with PBPK modeling can support the development of drug formulations with a beneficial PK profile in the clinical settings. Moreover, these types of *in vitro* models are well suited to study cellular uptake and transport mechanisms.

List of figures

List of tables

1 Introduction

Lung diseases can be therapeutically targeted via systemic delivery of drugs (e.g. intravenous drug application) or via inhalation [1]. However, systemic delivery of drugs for the treatment of lung diseases demonstrates two significant disadvantages. The administration route can lead to a reduced drug dose in the lung [2, 3] as the applied drug is subjected to enzymatic degradation in eliminating organs (such as the liver) or other degradation ways in the blood stream [1]. Moreover, systemic delivery increases the risk of the onset of adverse events [1, 4]. On the other hand, inhalation therapy targets the lungs directly, which implies that the entire delivered drug dose is initially available in the target organ (lung) and only gradually some of it will get transported in secondary organs. This leads to a high therapeutic index, i.e., it provides high efficacy in the lung relative to the invested amount of drug and it minimizes the risk of adverse (side) effects in secondary organs [5-7].

Inhalation therapies are well established for the treatment of chronic obstructive pulmonary disease (COPD), asthma, and pulmonary infections. For instance, the antibiotics levofloxacin and tobramycin are widely used for the treatment of pulmonary infections in cystic fibrosis patients [8, 9]. For the treatment of asthma and COPD, inhaled corticosteroids are part of the standard therapy [10]. Current trends in inhalation therapy include the use of biologics such as peptides and proteins due to the their specific binding to therapeutic molecular targets in diseased lung tissue and due to the potential of established methods such as antibody engineering to increase the stability in the diseased tissue [11]. Besides COPD, asthma, and pulmonary infections, treatment of lung cancer via inhalation is another important research field [12]. However, some investigated agents (e.g. chemotherapeutic agents such as Paclitaxel for lung cancer) have strong hydrophobic properties, demonstrate poor solubility, and therefore poor tissue penetration, which requires optimization of the drug formulation to guarantee high drug association in the tissue [13, 14].

To increase the drug association in the diseased lung tissue after inhalation and to enhance the solubility of the drug, the incorporation of drugs into nanocarriers (nanodrugs) is a prominent option [15, 16]. One prominent nanodrug example, which will be highlighted in the present work, is the peptide Cyclosporine A incorporated into liposomal nanocarriers (L-CsA) [17]. L-CsA is used to treat bronchiolitis obliterans (BOS), and is currently in the clinical phase III [18]. In addition, the present work has a strong focus on the hydrophobic drug Paclitaxel incorporated into polymeric nanocarriers (NanoPAX). Paclitaxel has shown potential to treat pulmonary arterial hypertension (PAH) in animals [19], and its polymeric formulation is currently in the preclinical development.

After inhalation, the lung retained drug dose is determined by interactions with the lung epithelium [20]. Transport processes characterize these interactions, leading to partial transport of the inhaled drug from the lung directly into the blood (systemic absorption) [21]. Together with distribution and elimination mechanisms in the blood, absorption of a drug by the blood circulation after inhalation is typically referred to as pharmacokinetics (PK) [7], which is an essential element of the regulatory drug approval [22]. Consequently, lung epithelial permeability of drugs is directly linked to pharmacokinetics (blood). Several methods aiming to predict the systemic absorption based on epithelial permeability have been introduced over the past years (for a review see Bosquillon et al. (2017) [23]). These also include *in vitro* strategies ensuring "the principles of the 3Rs (replacement, refinement, reduction" [24] of animal experiments.

The motivation of the present work is to assess epithelial permeability with physiological cell-based models and an *in vitro* air-liquid interface cell exposure system. Transepithelial transport rates will be assessed and used to describe the lung-to-blood transported dose. This will ultimately allow prediction of the pharmacokinetics (PK) profile (in the blood) of L-CsA and NanoPAX after inhalation *in vivo*.

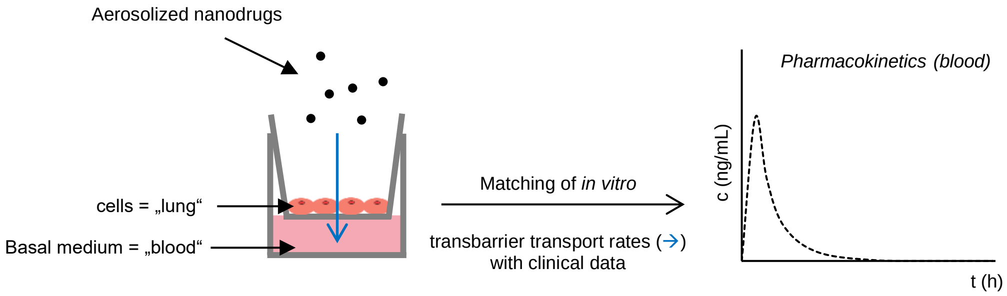

Figure 1.1: Graphical summary of the motivation. Nanodrugs will be aerosolized on *in vitro* cell-based models. The transbarrier transport will be transferred into PK by matching *in vitro* data with relevant *in vivo* data.

The following sections will provide background information on topics related to the main objective of the thesis including the use of nanocarriers for drug delivery to the lung, the role of the lung epithelium in transepithelial transport of aerosolized drugs by various cellular transport pathways, and computational approaches aiming to translate *in vitro* findings on epithelial permeability into relevant *in vivo* pharmacokinetics parameters. Since these issues are addressed with two types of nanodrugs for the treatment of PAH and BOS, some background on these diseases will also be presented here.

1.1 Inhalation of nanodrugs

Inhalation delivers drugs to the lungs of patients directly, which promises a high local dose, fast onset of action, and fewer systemic side effects than oral or intravenous administration of drugs [6, 7]. Typically, nebulizers are used to apply the drugs in aerosolized from the patients [25]. Treatment of lung diseases by inhalation as compared to intravenous application is further promoted by the fact that the presence of drug-metabolizing enzymes in the lung is less in comparison to other organs such as the liver, which prevents the generation of complex metabolites [26]. With regard to patient compliance, inhalation was found to be the most preferred administration way out of six routes of acute breathlessness patients [27].

Barriers in the lung against uncontrolled particle transport into the blood circulation include the lung lining fluid, the lung epithelium, and the endothelium [28].

These barriers determine the retention of the applied drug at the target site (here the lung) and amongst the most relevant processes are the so-called clearance mechanisms, which result in removal of the drug from the lung. The main clearance mechanisms are mucociliary clearance, uptake by alveolar macrophages, and metabolic degradation by lung-associated enzymes [25, 29, 30]. An additional clearance mechanism is trans- or paracellular transport of the drug through the thin epithelial-endothelial (air-blood) barrier (0.2 µm – 0.4 µm [31]), which enables fractional drug transport into the systemic circulation (systemic absorption) [32]. Thus, inhalation typically leads to a least partial transport of the inhaled drug from the lung directly into the blood [21], which is referred to as PK [7]. PK studies are an essential part of clinical drug testing, since they provide insights into the bioavailable dose and – in the context of lung diseases – it is a measure of inadvertent exposure of secondary organs potentially leading to side effects [33-35].

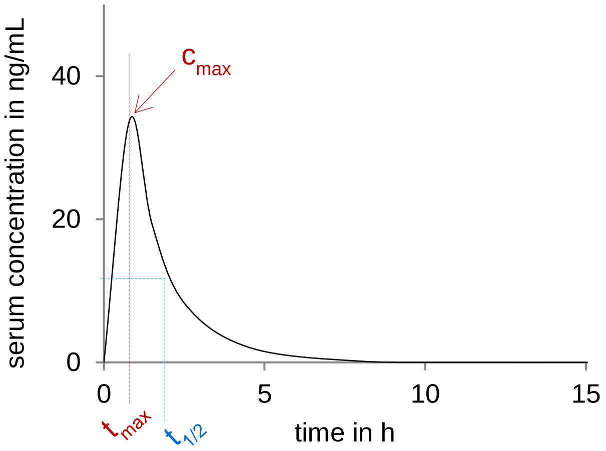

Figure 1.2: Typical PK parameters are the maximum concentration in the serum (c_{max}), the time until c_{max} is reached (t_{max}), and the half life time ($t_{1/2}$).

Although drugs can be cleared in different ways, the goal of inhalation therapy for lung diseases is to achieve a high concentration in the lung [7]. To increase the residence time of an inhaled drug in the lung, various drug delivery carriers were developed in the last years [36]. Interestingly, a drug can be modified by different physicochemical methods to act as a drug reservoir with sustained-release properties itself [36]. One example includes Paclitaxel (Ptx)-crystals, which were developed to treat non-small cell lung cancer [13, 37]. However, more often the drug molecules are loaded on various types of nanocarriers, which are designed to provide specific and efficient drug release [38]. Prominent examples for nanocarriers in inhalation therapy include polymeric and liposomal nanocarriers [39], which allow the “particle-based” application of drugs [40].

One commonly used compound for polymeric nanocarriers is Poly(lactic-co-glycolic acid) (PLGA) due to its non-toxic, biocompatible, and biodegradable properties [39, 41]. Polymeric nanocarriers show significant advantages such as adjusted drug release rate, enhanced penetration into lung lining fluid, and the possibility of specific cell targeting [42]. One example is Budesonide incorporated into PLGA-nanocarriers, which displays enhanced tissue penetration and thus enhanced efficacy [43]. Another example for successful drug loading into PLGA-nanocarriers is Rifampicin [44].

In addition to polymeric nanocarriers, liposomal drug formulations for inhalation therapy have already been in focus since the 1990s [45-48]. Liposomes are lipid vesicles consisting of a lipid bilayer (for hydrophobic drugs) and an aqueous core suitable for hydrophilic drugs [39]. Liposomal formulations exhibit significant advantages in comparison to conventional formulations. For example, tobramycin in a liposomal formulation applied to rats demonstrated enhanced efficacy in the treatment of a bacterial infection [49] and liposomal beclomethasone showed superior lung retention in asthma patients [50]. Increased lung retention was also found for liposomal amikacin, which was detectable even 50 hours after administration in healthy volunteers [51].

In conclusion, current strategies in inhalation therapy often focus on the design of nanocarrier systems to enhance the tissue penetration of drugs and to avoid fast clearance of drugs by various mechanisms, which have a strong impact on the PK profile of a drug.

1.2 Physiological-based pharmacokinetic (PBPK) modeling

To predict the PK of drugs already in the preclinical phase, physiologically based pharmacokinetic (PBPK) models can be applied. They are computational models describing the distribution of drugs over time throughout the entire organism [52, 53]. Moreover, these models consider different parts/organs of the body and drug exchange amongst them via the blood circulation and possibly

other drainage systems such as the lymphatic network [53]. Chemical properties of the drug (e.g. molecular weight and solubility) and biological parameters (e.g. enzymatic degradation or transbarrier transport rate) are linked by mathematical approaches (transport equations) to describe the contribution of different organs to the fate of the drug after administration [54, 55]. These equations include drug-organ-specific rate constants, which often have to be determined empirically from either *in vitro* or *in vivo* (animal) models or from previously obtained clinical data [56]. In fact, the term “physiologically-based” implied the need for access to these kinds of data. One important output of these models is the PK profile of the drug (in the blood) after drug administration [54], which is one of the key parameters required for regulatory approval of a new drug [57].
A simplified PBPK model structure with transport rates indicated by arrows amongst different organs of the body is illustrated in figure 1.2.

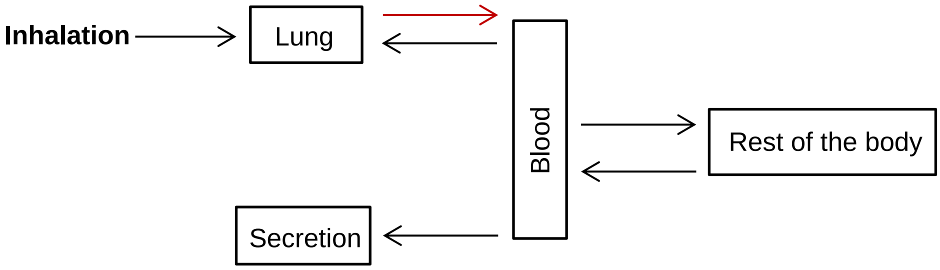

Figure 1.3: Simplified structure of a PBPK model. A PBPK model describes drug exchange amongst different organs/parts of the body by transport rates (indicated by arrows).

Several PBPK models focusing on the fate of drugs after inhalation were described in the past years. A model highlighting the relevance of the application route (inhalation vs. intravenous administration) was successfully implemented by Fridén et al. (2018), promising to allow selection of appropriate doses for the onset of action [58]. A model to analyze the influence of lung surface liquids (e.g. mucus) on the PK of a liposomal nanocarrier (liposomal Ciprofloxacin) after inhalation was published by Finlay et al. (2018) [59]. Campbell et al. (2015)[60] reported a model of butadiene, which included metabolic degradation of the drug in the lung. It was found that the experimentally determined systemic concentration after butadiene inhalation in rats, mice, and humans was comparable to the model that did not include metabolic activity [60]. Moreover, Weber and Hochhaus (2013) presented a PBPK model that included mucociliary clearance and drug deposition in different compartments of the lung [56].

Due to the complex lung structure and the various drug clearance processes, PBPK modeling in inhalation therapy still requires further optimization [61].

As PBPK models require access to physiological relevant characteristic parameters (mainly rate constants) from “different sources of literature data, *in vitro* data, or educated guesses” [56], one option to improve the output of PBPK models is to optimize the predictive power of *in vitro* models.

1.3 Epithelial permeability studies

One of the key parameters of reliable PBPK models for inhaled drugs is the rate of transport of the drug/nanocarrier across the epithelial-endothelial tissue barrier from the lung into the blood, often referred to as permeability [23]. This is an important parameter as the epithelial-endothelial (air-blood) barrier influences the clearance of lung deposited drugs [26, 32].

Epithelial permeability can be investigated by *in vitro* cell models on commercially available Transwell® inserts. However, there is a large variety of potentially suitable cell-based *in vitro* models both in terms of cell type and culture conditions. Both aspects were considered for selection of the most suitable *in vitro* cell model for the nanocarrier-based drugs investigated in the present study.

With regard to culture conditions, epithelial permeability studies can be run under air-liquid interface (ALI) or submerged conditions (figure 1.1). At ALI conditions, the cells are supplied with growth medium only from the basal side, whereas submerged cell culture supplies the cells completely with growth medium [62]. As the human lung presents an interface between air and blood [31], ALI cultures are a more physiological way to simulate the lung *in vitro* [63].

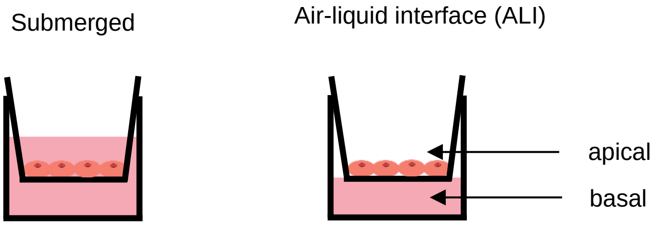

Figure 1.4: Comparison of cell culture conditions on Transwell® inserts. While cells are completely covered with medium at submerged conditions, Air-liquid interface culture (ALI) supplies the cells only from below (basal compartment). ALI cultures provide a more physiologic model for inhalation therapy and drug transport into the blood (basal compartment).

Another key issue for any cell-based *in vitro* model is the selection of the most suitable cell type, which will depend on the particular scientific question to be addressed. For pulmonary drug absorption into the blood, a model for the alveolar air-blood barrier appears to be most suitable but frequently bronchial epithelial cells have been used for absorption/permeability studies mainly due to limitations with currently available alveolar barrier models [64]. Nevertheless, each of these cell culture models has advantages and limitations mainly related to the simulation of all involved physiological conditions (e.g. shear stress, flow conditions, and involvement of immune cells) [65]. An overview of frequently used cell types with a discussion of their advantages and limitations is provided by Bur and Lehr (2008) [66]. The most frequently used cell types for transport studies include bronchial (Calu-3, 16HBE14o-) [67, 68], and alveolar epithelial cell lines (A549, NCI-H441, hAELVi) [68-70].

For many drugs, there is a good correlation between *in vitro* epithelial permeability and *in vivo* drug absorption into the blood. ALI cultured Calu-3 cells were used to study the transport of dextran molecules of various sizes by Grainger et al. (2009)[71]. It was shown that the mass transported through the *in vitro* barrier correlated linearly with the clearance of dextran molecules (e.g. by absorption) of the same molecular weights (sizes) from a canine lung [71, 72]. Similarly, Mathia et al. (2002) found a linear correlation of the transport profiles for various molecules (e.g. Lucifer yellow or mannitol) obtained from ALI cell models and a rat lung [67].

In spite of the good correlation between *in vitro* and *in vivo* permeability, there are fundamental differences between transport rates observed for submerged and ALI cell cultured models. For instance, Trammer et al. (2008)[73] have shown that a liposomal formulation of Cyclosporine A (L-CsA), which is used to treat lung rejection after lung transplantation [17], exhibited a weaker permeability across a Calu-3 cell monolayer than a propylene glycol formulation of this drug. In this study, the Calu-3 cells were cultured at submerged conditions, and thus the cells were covered with growth medium in the basal and apical compartment of a Transwell® insert, respectively. The drug formulations were pipetted into the apical compartment of the Transwell® insert and linear transport into the basal compartment was measured [73]. In contrast to this, Schmid et al. (2017)[68] used an A549 cell monolayer, which was exposed to L-CsA in aerosolized form. It was shown that L-CsA was transported with an initial burst into the basal compartment [68].

Meindl et al. (2015)[74] reported a direct comparison of permeability between submerged and ALI conditions. Various molecules (e.g. fluorescein, budesonide) were delivered to the cells and the epithelial permeability was investigated. It was found that the ALI culture demonstrated faster transport rates [74], suggesting that ALI culture facilitates the permeability of the used compounds. In conclusion, ALI transport rates are typically higher and have a burst-like temporal profile.

The concept of combining *in vitro* cellular transport rates with PBPK modeling of pulmonary applied nanoparticles was presented by Bachler et al. (2015)[52]. Gold nanoparticles of different sizes were nebulized onto ALI cultured A549 cells (alveolar epithelial cells) and transport rates were derived from the temporal dose of nanoparticles in the basal compartment. Moreover, transport rates of these nanoparticles were combined with PBPK modeling to predict organ doses for the same set of gold nanoparticles intratracheally instilled to mice [52].

There are numerous cell-based *in vitro* permeability assays, which have predictive capacity for *in vivo* transport rates of inhaled drugs/nanocarriers. Historically, most of the *in vitro* data has been obtained with cells at submerged conditions, albeit ALI cells are more physiologic. Quantitative comparison between *in* *vitro* and *in vivo* transport rates are rare and typically require complex computational PK modeling.

1.4 Enhancing the *in vivo* relevance of *in vitro* models

The prediction of relevant *in vivo* parameters is typically referred to as *in vitro-in vivo*-correlation (IVIVC) [67, 75]. Although different IVIVC strategies were developed, physiologically more relevant models are required to optimize the predictive power of *in vitro* results [76, 77].

One strategy to improve the predictive power of *in vitro* models includes the addition of further cell lines or the use of primary cells. For instance, the simple A549 cell model on commercially available Transwell® inserts was further extended by adding endothelial cells, mast cells, and macrophage-like cells [78]. This tetra-culture model was used to analyze the effect of nanometer and micrometer-sized silver particles on cell viability, cytotoxicity, generation of reactive oxygen species, and pro-inflammatory response [79]. Furthermore, dendritic cells and alveolar macrophages were added to the A549 cell model on Transwell® inserts to analyze the interplay of particle uptake by the cells [80, 81]. Also, primary cell models of the alveolar epithelium have recently been presented [82].

However, even the most complex multi-cell mode of the alveolar barrier has limitations. One major drawback of the human lung cell culture on commercially available Transwell® inserts is that their thickness (ca. 10 µm) is much larger than that of the basement membrane of the pulmonary air-blood barrier (< 1 µm) [83]. Therefore, alternative membranes and scaffolds for the growth of lung cell lines have been developed [83, 84], mirroring another strategy to increase the *in vivo* value of *in vitro* models. Unlike Transwell® inserts, scaffolds have the advantage of getting modified by different physiological parameters [85]. For example, the addition of shear stress was shown to influence cellular transport of molecules significantly [86]. Another strategy to improve the biomimetic characteristics of cell-line based *in vitro* models of the alveolar barrier is the addition of surfactant or even lung lining fluid [79].

Finally, improving the experimental setup can increase the predictive power of *in vitro* models. Aerosolized drug delivery is one example for more physiologically simulating the clinical conditions during inhalation therapy under *in vitro* laboratory conditions. Most currently available *in vitro* technologies for aerosol-cell delivery are limited in terms of delivery rate, i.e. exposure times exceed the clinically acceptable range of up to a few minutes per application [87]. One of the few exceptions the Air Liquid Interface Cell Exposure (ALICE) technology for liquid drugs, which was first published by Lenz et al. (2009) to deliver nanoparticles and molecules to cells grown on Transwell® inserts [88], and then refined into the ALICE Cloud system for dose-controlled, aerosolized drug delivery to ALI cell culture models of the lung [89]. Meanwhile, the latter system was commercialized as VITROCELL® Cloud 6.

1.5 Advantages of air-liquid interface cell exposure

As mentioned, human lung cell culture is either carried out at submerged or at ALI conditions. Over submerged conditions, ALI culture demonstrates several different outcomes.

First of all, ALI culture demonstrates different transbarrier transport rates in comparison to submerged cell culture. In detail, a burst-like transport profile can be observed when molecules and nanodrugs are delivered to cells at ALI conditions [68, 74].

Another difference concerns the response to environmental nanoparticle exposure. Ghio et al. (2013)[90] have shown that ALI cultured human bronchial epithelial cells demonstrated a reduced inflammatory response to air pollution particles in comparison to submerged cultured cells. They found that the hypoxic conditions at submerged conditions together with the particles led to inflammation. Thus, ALI culture demonstrates increased availability of oxygen, preventing the hypoxic conditions that could occur at submerged conditions [90]. Decreased inflammatory response to allergen coated nanoparticles was also shown for hAELVi cells at ALI conditions compared to submerged conditions [91].

ALI culture further displays faster onset of drugs. In a direct comparison between both cell culture modes by Lenz et al. (2009), the ALI culture led to faster uptake of the proteasome inhibitor Bortezomib [89]. As mentioned by Röhm et al. (2019), this can be led back to the fact that ALI exposure decreases the degree of protein aggregation, which happens at submerged conditions [92]. Another advantage of ALI culture and exposure relates to the dosimetry. Contrary to submerged cell models, ALI exposure guarantees a direct measure of the cell-delivered dose [63]. This advantage can be used to directly measure the onset of effects after nanoparticle exposure [88, 93].

Finally, ALI culture was shown to resemble essential *in vivo* characteristics. ALI culture of human induced pluripotent stem cells was shown to promote the differentiation into an alveolar epithelium phenotype [94], and to resemble the transcriptome of the airway epithelium [95].

All in all, ALI culture of lung cells has significant effects on the transbarrier transport of drugs/nanodrugs/nanoparticles, inflammatory responses, differentiation, and on the estimation of the onset dose in toxicological studies. However, the clinical relevance of these differences still has to be validated.

1.6 Transport mechanisms for nanodrugs

Epithelial permeability for drugs or nanodrugs depends on the barrier function of the human lung and the transport of these compounds across the barrier [20]. The barrier function is characterized by tight junction proteins [96, 97]. They are assembled by the transmembrane proteins Occludin, Claudin, and Junctional adhesion molecules (JAMs) that are linked to the Actin cytoskeleton via the cytoplasmic proteins ZO-1, ZO-2, and ZO-3 [98].

Transport across biological barriers can be distinguished between paracellular and transcellular transport [20]. Tight junctions control the paracellular transport of the lung epithelium [99], which is the transport of molecules or particles between the cells [20, 100]. The other way is transcellular transport, which requires cellular uptake of particles or molecules [20]. Endocytosis is one prominent transcellular transport pathway that can be distinguished into four classes: caveolae-mediated endocytosis, clathrin-mediated (receptor-mediated) endocytosis, macro-pinocytosis, and phagocytosis [101, 102]. Differences in the endocytosis classes concern the entry mechanism of nanoparticles or nanodrugs [103], which lead to the presence of different intracellular protein complexes with the nanoparticles or nanodrugs [104]. Although there are different mechanisms of entry, similarities can be found in the fate after the uptake. For nanodrugs, a protein-nanodrug complex originates, which fuses with the lysosome after cellular uptake and several intermediate steps, finally leading to the release of the drug inside the cell [105, 106].

The hydrophilicity plays a crucial role in the determination of paracellular or transcellular uptake. Small hydrophilic molecules or ions can pass an epithelium via the paracellular route, while lipophilic molecules rather demonstrate cell-uptake, possibly due to interactions with the lipid bilayer [26, 107]. Another point, which determines para- or transcellular uptake, is the size [26]. This parameter has extensively been studied for environmental nanoparticles, such as polystyrene nanoparticles [100, 108] or latex nanoparticles [109]. Here, it can be concluded that nanoparticles > 100 nm prefer transcellular uptake pathways, while smaller nanoparticles bypass the cells (paracellular transport) [110].

The role of size and charge in the transport mechanisms can also be transferred to nanodrugs. The size of drug loaded nanocarriers (nanodrugs) typically ranges from 50 nm – 1000 nm [15]. Thus, transcellular uptake can be expected, which was reported by several groups: Stolnik et al. (2018) have shown that caveolae mediated endocytosis and clathrin mediated endocytosis were involved in the uptake of 80 – 100 nm-sized cationic liposomes by A549 cells [111]. The involvement of clathrin mediated endocytosis was also confirmed in the A549 cellular uptake of 155.2 nm-sized cationic liposomes by Huang et al. (2018) [112]. Wu et al. (2015)[113] investigated the role of the charge on cellular uptake of liposomes by A549 cells. Starting with anionic 100 nm-sized liposomes, they modified the liposomes with peptides, which resulted in a positive surface charge. This significantly increased the cellular uptake [113].

As epithelial permeability not only depends on the transport of nanodrugs but also on the barrier function [20], changes in this function is investigated extensively in the context of lung diseases. Tight junctions are dynamic structures, meaning that they can be subject to environmental changes [114, 115]. For instance, these changes include inflammatory conditions in the lung, which were found to alter tight junction expression [116-118]. In detail, epithelial tight junctions were affected, leading to higher permeability [116-119].

In conclusion, epithelial permeability is a crucial parameter as it determines the dose of inhaled nanodrugs in the lung and can be subject to lung diseases.

1.7 Molecular and cellular mechanisms of pulmonary arterial hypertension (PAH)

Pulmonary arterial hypertension (PAH) is characterized by enhanced pulmonary arterial pressure due to the remodeling of blood vessels [120, 121]. Besides smooth muscle cells, endothelial cells are involved in the remodeling via increased proliferation and resistance to apoptosis [122]. In addition, endothelial-to-mesenchymal transition (EMT) leads to further remodeling of the vascular system in the lung via an increase of the smooth muscle cell phenotype [123].

FoxO1 signaling, which is involved in the regulation of cellular proliferation, is a promising target of PAH since the transcriptional activity of FoxO1 was found to be downregulated in smooth muscle cells isolated from PAH patients [19]. The phosphorylation of FoxO1 leads to the deactivation of its transcriptional activity by exclusion from the nucleus [124]. Besides its role in the regulation of proliferation, FoxO1 is a repressor of the Claudin-5 gene, which regulates the assembly of tight junction proteins [124, 125]. It was found that phosphorylated FoxO1 increased the amount of Claudin-5 transcripts in acute lung injury, which can be interpreted as a rescue mechanism to recover barrier integrity [126].

Inflammation is one of the various factors that are involved in the development of PAH [127]. Increased TNF-α levels were found in the serum of PAH patients, and TNF-α was shown to promote vascular remodeling, leading to impaired barrier properties of the lung endothelium [128-130]. Besides TNF-α, activated Signal Transducer and Activator of Transcription 3 (STAT3) was evaluated as another key driver involved in the development of endothelial dysfunction [131]. Activated STAT3 was further shown to increase the survival and proliferation of smooth muscle cells and to increase immune responses [131, 132].

As mentioned above, the endothelial barrier is directly affected in PAH [130, 133]. A healthy endothelial barrier modulates vascularity and acts anti-inflammatory due to the barrier properties guaranteed by tight junction proteins [134]. In the endothelium, these proteins are Occludin and Claudin, which are further associated with proteins of the ZO-family [135]. In endothelial dysfunction as a key element of PAH [122], tight junctions are subject to mitigation [136]. This is directly promoted by inflammatory cytokines such as TNF-α and IL-6 [137-139].

In summary, PAH is characterized by changes in the endothelial barrier integrity of the lung. Transcriptional changes activated by inflammatory cytokines are among the mechanisms that contribute to the altered barrier properties.

1.8 Paclitaxel for the treatment of PAH

Paclitaxel (Ptx) is a drug with cytotoxic and anti-cancer activities, which were discovered in 1965 as a result of a plant screening program initiated by the National Cancer Institute (NCI) and US department of agriculture (USDA) [140].

In the field of PAH, Ptx was found to restore FoxO1 activity in a rat model of PAH by dephosphorylating FoxO1 [19, 141]. Moreover, Ptx promoted pro-apoptotic and anti-proliferative capacities of hyper-proliferative smooth muscle cells [19]. Also, physiological parameters, such as the thickness of pulmonary arteries were significantly reduced in a PAH rat model [142].

Meanwhile, the application of the drug was further refined and combined with sustained release approaches, e.g. liposomal Ptx [143]. Ptx incorporated into 100 – 200 nm-sized lipid nanocarriers showed a significant increase in the cytotoxicity of murine melanoma cells [144]. Add to this, the levels of pulmonary metastases have been significantly decreased in a murine lung cancer model [144]. This reduction was also shown for a murine model of renal cell carcinoma [143]. In an *in vitro* model of lung deposition, the Ptx formulation incorporated into the lipid nanocarriers demonstrated a 17-fold increase in the deposition as compared to the conventional formulation without nanocarriers [145]. Furthermore, Ptx-crystals (NanoPac®) showed anti-tumor properties in a rodent lung cancer model by promoting immune cell infiltration [13, 37]. Prolonged action at the target site was also shown for Ptx incorporated into 22 µm-sized PLGA particles [146].

In summary, Ptx shows high potential to reverse the transcriptional changes that are involved in PAH.

1.9 Liposomal Cyclosporine A (L-CsA) for the treatment of Bronchiolitis Obliterans Syndrome (BOS)

A lung disease with epithelial barrier damages and dysfunction is bronchiolitis obliterans (BOS) [147, 148]. BOS is linked to lung rejection after lung transplantation [149], and characterized by fibrosis of the lung epithelium [150]. Moreover, epithelium-mesenchyme transition (EMT) is involved in the development of the disease [151]. EMT is linked to a reduction in gene expression of epithelial tight junction proteins [152]. This limited expression leads to changes in the barrier function [153], which finally promote the EMT [154]. Disease-related cytokines are IL-8, IL-1β, and TNF-α, which was found to be the key player in the initiation of EMT [151].

One therapeutic option for BOS treatment is to target immune responses after lung transplantation, e.g. by Cyclosporine A (CsA) [155]. CsA is a cyclic peptide consisting of eleven amino acids [156], and exhibits its action through inhibition of the calcineurin phosphatase activity in T-cells, leading to silencing of immune response gene expression [157].

A clinical study on inhalable CsA was carried out by Corcoran et al. (2014) on lung transplantation patients. The study could highlight the effective lung retention of CsA [158]. To further increase the retention, liposomal nanocarrier formulations of CsA were developed. A liposomal formulation of the drug was already investigated by Letsou et al. on animals in 1999 [45]. In patients, L-CsA was successfully applied via inhalation by Behr et al. (2009)[17]. Most importantly, adverse side effects were overall not observed using the nanocarrier formulation of CsA [17]. Toxic effects were also not observed in a L-CsA study from 2019, and in addition, lung function and survival of lung transplant patients were improved [18].

All in all, L-CsA demonstrated safety and efficacy in treating BOS.

2 Key questions

This work investigates the potential of currently available non-primary cell-based *in vitro* models of the alveolar air-blood barrier to mimic biokinetics and efficacy of inhalable nanocarrier-based drugs (nanodrugs) observed under *in vivo* (animal) or clinical conditions. This overall objective was subdivided in the following key questions:

- Which challenges do we encounter in the use of simple *in vitro* models on commercially available Transwell® inserts?
- How are liposomal and polymeric nanocarriers transported into and through *in vitro* lung epithelial cells at ALI conditions?
- How does a more physiological model of the air-blood barrier, which includes endothelial cells, affect the transport of nanodrugs?
- How can *in vitro* models support clinical development of nanodrugs?
- How do lung diseases affect the transport of nanodrugs?

3 Material

3.1 Devices

Description	Name	Supplier	Purpose
Air-Liquid Interface Cell Exposure System	VITROCELL® Cloud 6	VITROCELL Systems, Waldkirch, Germany	Nanodrug exposure
Analytical balance	Mettler AT250	Mettler-Toledo Inc., Ohio, USA	Preparation of reagents
Cell counting chamber	Neubauer improved white-line	Paul Marienfeld GmbH & Co. KG, Lauda-Königshofen, Germany	Cell culture
Cell culture incubator	Heraeus BBD 6620	Thermo Fisher Scientific Inc., Waltham, USA	Cell culture
Epithelial Volt-Ohmmeter (EVOM)	Millicell ERS-2	Merck KGaA, Billerica, USA	Transepithelial electrical resistance (TEER) measurements
Fluorescence microscope	Olympus BX51	Olympus Corp., Tokyo, Japan	Fluorescence Imaging
Inverted microscope with phase contrast	Axiovert 25	Carl Zeiss AG, Oberkochen, Germany	Cell counting
Laminar hood	Herasafe KS 12	Thermo Electron LED GmbH, Langenselbold, Germany	Cell culture
Micro plate reader (absorption & fluorescence)	Safire 2	Tecan Trading AG, Männedorf, Switzerland	Functional assays
Micro plate reader (luminescence)	GloMax	Promega Corporation, Madison, USA	Functional assays
Refrigerated centrifuge	Sigma 3K15	Sigma Laborzentrifugen GmbH, Osterode am Harz, Germany	Cell culture
Refrigerated centrifuge	Hettich Universal 32R	Andreas Hettich GmbH & Co. KG, Tuttlingen, Germany	Functional assays
Scanning Electron Microscope (SEM)	Zeiss Crossbeam 340	Carl Zeiss AG, Oberkochen, Germany	SEM
Shaker	DUOMAX 1030	Heidolph Instruments GmbH & Co. KG, Schwabach, Germany	Functional assays
Spectrophotometer	NanoDrop1000	Peqlab, Erlangen, Germany	RNA
Water bath	Julabo MB13	Julabo GmbH, Seelbach, Germany	Cell culture
Vacuum coater	Leica EM ACE200	Leica Camera AG, Wetzlar, Germany	SEM

3.2 Consumables

Name	Supplier	Catalog number	Purpose
96-Well plate (black) for fluorescence measurement	Greiner Bio-One GmbH, Frickenhausen, Germany	655086	Fluorescence measurements
96-Well-Platte (white) for luminescence measurement	Thermo Fisher Scientific Inc., Waltham, USA	136101	Luminescence measurements
96-Well-Platte (transparent) for absorption measurement	Thermo Fisher Scientific Inc., Waltham, USA	260836	Absorption measurements
50 mL-centrifuge tubes	Corning Inc., New York, USA	352070	Cell culture & functional assays
Aluminum stubs for SEM	Agar Scientific Ltd., Stansted Mountfitchet, England	AGG301F	SEM
Cell scraper	Techno Plastic Products AG, Trasadingen, Switzerland	99002	RNA isolation
Costar® Transwell® inserts (3.0 µm) for 6-well cell culture plates (in Ptx-NP studies)	Corning Inc., New York, USA	3452	Cell culture and exposure
Falcon® Permeable Support for 6-well Plate with 3.0 µm transparent PET Membrane	Corning Inc., New York, USA	353091	Cell culture and exposure
Filtering paper (for Bradford)	GE Healthcare Europe GmbH, Freiburg, Germany	10311841	Protein assay
T75 cell culture flask with filter	Greiner Bio-One GmbH, Frickenhausen, Germany	658175	Cell culture
T75 cell culture flask without filter	Greiner Bio-One GmbH, Frickenhausen, Germany	658190	Cell culture (media preparation)

3.3 Reagents

Name	Supplier	Catalog number	Purpose
1x Dulbecco’s Phosphate Buffered Saline (PBS)	Thermo Fisher Scientific Inc., Waltham, USA	14190094	Cell culture & functional assays
0.25% Trypsin-EDTA solution	Sigma-Aldrich Corp., St. Louis, USA	T4049	Cell culture
0.4% Trypan blue solution	Thermo Fisher Scientific Inc., Waltham, USA	15250061	Cell culture
1x Glo Lysis Puffer	Promega Corp., Madison, USA	E2661	Cell lysis (protein)
1N HCl	Merck KGaA, Darmstadt, Germany	1090571000	Lactate dehydrogenase (LDH) assay
Avanti Polar Lipids Extruder Set with Block	Sigma-Aldrich Corp., St. Louis, USA	610000	Fluorescence Resonance Energy Transfer (FRET) liposomes
Blue Dextran 2000	GE Healthcare, Buckinghamshire, United Kingdom	17036001	Dextran blue assay
BODIPY FL Phallacidin dye	Thermo Fisher Scientific Inc., Waltham, USA	B607	Staining
Bovine serum albumin	Bio-Rad Laboratories Inc., Hercules, USA	5000007	Protein assay
Buffer RLT	Qiagen, Venlo, Netherlands	79216	Cell lysis (RNA)
Cholesterol	Thermo Fisher Scientific Inc., Waltham, USA	A11470	FRET liposomes
Chloroform	Sigma-Aldrich Corp., St. Louis, USA	C2432	FRET liposomes
Cytotoxicity detection kit	Roche Diagnostics GmbH, Mannheim, Germany	11644793001	LDH assay
Distilled ultrapure water	Thermo Fisher Scientific Inc., Waltham, USA	10977035	Cell culture & functional assays
Dulbecco's Modified Eagle Medium/Nutrient Mixture F-12 (DMEM/F-12)	Thermo Fisher Scientific Inc., Waltham, USA	31330038	Cell culture
DMEM/F-12 without phenol red	Thermo Fisher Scientific Inc., Waltham, USA	11039021	Cell culture
Dichloromethane	Sigma-Aldrich Corp., St. Louis, USA	270997	FRET liposomes

Name	Supplier	Catalog number	Purpose
DiD	Thermo Fisher Scientific Inc., Waltham, USA	D7757	FRET liposomes
DiI	Thermo Fisher Scientific Inc., Waltham, USA	D3911	FRET liposomes
Fetal bovine serum (FBS)	Biochrom GmbH, Berlin, Germany	S0615	Cell culture
Gentamycin solution	SERVA Electrophoresis GmbH, Heidelberg, Deutschland	47991	Cell culture
Glutaraldehyde	Sigma-Aldrich Corp., St. Louis, USA	G5882	SEM
Halt^{TM} Phosphatase Inhibitor	Thermo Fisher Scientific Inc., Waltham, USA	78444	RNA isolation
Hexamethyldisilazane	Sigma-Aldrich Corp., St. Louis, USA	440191	SEM
Lactate dehydrogenase standard	Roche Diagnostics GmbH, Mannheim, Germany	10127230001	LDH assay
Luciferase assay reagent: ONE-Glo	Promega Corp., Madison, USA	E6120	Interleukin-8 (IL-8) assay
Methanol	Sigma-Aldrich Corp., St. Louis, USA	322415	FRET liposomes
Mounting medium with 4′,6-Diamidin-2-phenylindol (DAPI) dye	Thermo Fisher Scientific Inc., Waltham, USA	P36935	Actin-DAPI staining
Penicillin-streptomycin solution	Thermo Fisher Scientific Inc., Waltham, USA	15140122	Cell culture
Protein staining solution	Bio-Rad Laboratories Inc., Hercules, USA	5000006	Protein quantification
RIPA buffer	Thermo Fisher Scientific Inc., Waltham, USA	89901	RNA isolation
RNeasy® Plus Mini Kit	Qiagen, Venlo, Netherlands	74136	RNA isolation
Sodium citrate-hydrochloric acid buffer solution	Sigma-Aldrich Corp., St. Louis, USA	S6639	FRET liposomes
Soy Lecithin	Thermo Fisher Scientific Inc., Waltham, USA	J61675	FRET liposomes
TNF-α	Thermo Fisher Scientific Inc., Waltham, USA	PHC3015	Disease modeling
Triton-X100	Sigma-Aldrich Corp., St. Louis, USA	X100	FRET liposomes
Water-soluble tetrazolium salt (WST-1)	Roche Diagnostics GmbH, Mannheim, Germany	11644807001	Metabolic activity assay

3.4 Software

Name	Source	Purpose
CellSens Dimension, Version 1.5	Olympus Corp., Tokyo, Japan	Fluorescence Microscopy control
GraphPad Prism 8	Graphpad Software, Inc., San Diego, USA	Statistical analysis
ImageJ, Version 1.48	National Institutes of Health, Bethesda, USA	Microscopy picture modification tool
Microsoft Office 2010	Microsoft Corp., Washington, USA	Data analysis and generation of figures
Magellan, Version 7.2	Tecan Trading AG, Männedorf, Switzerland	Data analysis software for absorption and fluorescence measurements
SigmaPlot 12.0	Systat Software Inc., San José, USA	Statistical analysis
VisiView	Visitron Systems GmbH, Puchheim, Germany	Live Cell Imaging Microscopy Control

3.5 Cell lines

Name	Organism	Morphology	Tissue	Growth
A549-Luc(IL-8)	*Homo sapiens*, Human	epithelial-like	Adenocarcinoma of the lung	adherent
EA.hy926	*Homo sapiens*, Human	endothelial	somatic cell hybrid	adherent

4 Methods

Cell-based *in vitro* models were established on commercially available Transwell® inserts and cultured at air-liquid interface conditions (ALI). The VITROCELL® Cloud 6 system was used to deliver inhalable nanocarrier-based drugs to the *in vitro* models. The transport of the drugs across the cellular barrier was monitored and combined with physiologically-based pharmacokinetic (PBPK) modeling to predict the PK in clinical conditions. Moreover, the fate of the nanocarrier-drugs was analyzed by incorporation of fluorescent dyes and particle size analysis.

4.1 Cell culture

The epithelial A549-Luc(IL-8) reporter cell line, a human lung alveolar epithelial type II-like cell line, which was stably transfected with a luciferase reporter gene under the control of the of interleukin-8 (IL-8) promoter (IL-8: pro-inflammatory cytokine) [159], was cultivated in DMEM/F-12 at 37 °C and 5% CO_2. The medium was supplemented with 1% Gentamycin, 1% Penicillin-Streptomycin, and 10% fetal calf serum.

The endothelial cell line EA.hy926 was cultivated in DMEM/F-12 supplemented with 1% (v/v) Penicillin-Streptomycin and 10% fetal calf serum.

For the A549-Luc(IL-8)/EA.hy926 coculture, cell seeding density of the endothelium and strategy were adapted as previously described by Klein et al. (2013) [78]. Briefly, Transwell® inserts (Costar, 3.0 µm pore size) were turned upside down, and the EA.hy926 cell suspension was added. After an adhesion time of 2 h, inserts were placed back into the culture plate and the A549-Luc(IL-8) cell suspension was added, resulting in an epithelial-endothelial model of the air-blood barrier. Cells were allowed to achieve confluency for 4 days and were cultured for 24 h at ALI conditions before the aerosolization of different nanocarriers.

For the *in vitro* modeling of pulmonary hypertension, EA.hy926 cells were challenged by TNF-α. In detail, cells were seeded into T75 flasks at a density of $0.27 \cdot 10^6$ cells/cm². On the third day after cell seeding, the growth medium was replaced with TNF-α-supplemented medium to achieve a dose of 9 ng/cm² and 18 ng/cm², respectively (see figure 4.1). After 24 h, the A549-Luc(IL-8)/EA.hy926 coculture was seeded on Transwell® inserts as described above.

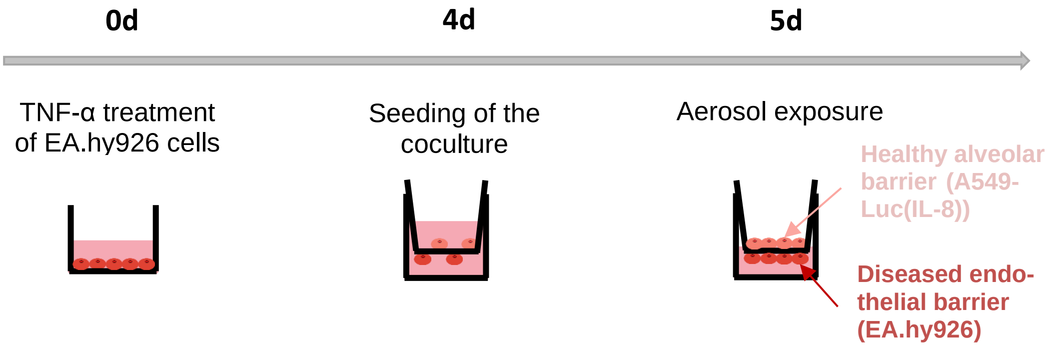

Figure 4.1: Timeline of the disease modeling. Only endothelial cells (EA.hy926 cell line) were challenged by TNF-α before the establishment of the coculture with epithelial cells (A549-Luc(IL-8) cells).

Liposomal Cyclosporine A (L-CsA), liposomes with an incorporated FRET pair (FRET liposomes), and a polymeric nanocarrier system loaded with Ptx (Ptx-NP) were delivered to cellular models of the air-blood barrier.

The FRET pair encapsulated liposomes were developed as described previously [160]. In brief, 10 mg of soy lecithin and 2 mg of cholesterol were dissolved in a 2:1 mixture of chloroform and methanol. The FRET probes (DiI and DiD) solution in dichloromethane was added to the lipid mixture before the evaporation of the solvents under vacuum at 40 °C to form a thin film layer. The liposomes were prepared by a thin-film dispersion method, where 2 mL of PBS solution (pH 7.4) was added to the lipid film. Thereafter, the resulting mixture was incubated at 40 °C without a vacuum for 30 min. The final concentration of the FRET pair in the liposomes was 40 µg/mL. Finally, the liposome size was reduced by extrusion with a 100 nm filter membrane. Fluorescence intensity was analyzed by an excitation wavelength of 505 nm and an emission wavelength of 705 nm, respectively.

Different batches of L-CsA and Ptx-NP were kindly provided by Breath Therapeutics GmbH (Munich) and by Alexandra Dalla-Bona and Tobias Gessler from the Justus-Liebig University Gießen, respectively. The exact content of the formulations is proprietary, but L-CsA encapsulates Cyclosporine A into the lipid bilayer of the liposomal carrier, the liposomes are typically between 100 and 200 nm in diameter and they withstand nebulization with a vibrating mesh nebulizer (as used here) without damaging the liposomes (see Schmid et al. (2017), [68]). Lyophilized L-CsA was taken up in 0.25% NaCl to obtain a stock suspension of 15.1% (w/v).

Ptx-NP incorporate Paclitaxel into a shell consisting of the polymers polyvinyl alcohol and poly(lactic-co-glycolic acid, the polyester polylactic acid, and tocophersolan [161]. The size range of Ptx-NP is within 140 and 200 nm. Lyophilized Ptx-NP were taken up in PBS/dH_2O 1:1000 to achieve a stock suspension of 4% (w/v).

Dynamic Light Scattering (DLS) analysis was carried out with a Zetasizer Nano ZS90 to obtain the diameter of the nanodrugs before and after nebulization.

4.3 Air-Liquid Interface Cell Exposure (ALICE) with the VITROCELL® Cloud 6 system

The VITROCELL® Cloud 6 system, first introduced in an early version as Air Liquid Interface Cell Exposure (ALICE) technology in 2009 [88], and then refined into the so called ALICE-Cloud technology [89], was used for dose-controlled delivery of aerosolized nanocarriers to models of the air-blood barrier. To aerosolize the nanodrugs, a vibrating mesh nebulizer Aeroneb Pro® was used.

In detail, the wells of the VITROCELL® Cloud 6 were filled with 13 mL PBS. After a preheating period of 2 h to 37 °C, Transwell® inserts were placed into the wells and the signal of the quartz crystal microbalance (QCM) was set to zero. To avoid that the aerosol cloud generated by the VITROCELL® Cloud 6 system "escapes" via the lateral openings of the Transwell® insert into the basal medium, so-called media covers (provided by VITROCELL® Systems) were used, which close the lateral openings. For biokinetics analysis, 500 µL of the respective nanodrug formulation (L-CsA: 15.1% (w/v), Ptx-NP: 4% (w/v)) was nebulized on the cells. A sufficient deposition, which is the even distribution of an aerosolized drug in the system, was guaranteed using the quartz crystal microbalance (QCM), which is integrated in the Cloud system for real-time dosimetry.

After the sedimentation period of 5 min, the Transwell® inserts were placed back in the 6-well plate to contact the bottom of the Transwell® insert membrane and cell culture medium. It is important to mention that t = 0 h in our *in vitro* biokinetics studies of various nanocarriers corresponds to the end of the aerosol delivery period (5 min). Consequently, the transport of nanodrugs before 5 min could not be clarified.

4.4 Transbarrier transport analysis of aerosolized nanodrugs

Sample processing was adapted from a study of nebulized L-CsA by Schmid et al. (2017) [68]. The apical compartment (contact-side of the cells with the air) was rinsed three times with 500 µL 0.9% NaCl to wash the nanodrugs from the epithelial barrier. The basal compartment (medium below the cells) was transferred into a cup by pipetting. Finally, the Transwell® insert membrane containing the cells was cut out and transferred into a cup containing 1.5 mL deionized water. To lyse the cells, the cup was frozen in liquid nitrogen and thereafter thawed in a 37°C water bath (cell compartment). This was repeated three times. The Ptx or CsA concentration in the prepared samples was analyzed by the project partners in Gießen and in Munich, respectively, via HPLC-MS/MS. It is important to mention that the concentration of the free drug was measured (CsA or Ptx, respectively). For L-CsA, the liposomal shell was destroyed with Acetonitril prior to the analysis.

For biokinetics analysis, a membrane-only control (insert without cells) was included to correct for the influence of the membrane on the biokinetics, a mathematical approach was applied. The Transwell® insert was separated into three compartments that are referred to as cells/apical compartment, membrane compartment, and basal compartment (Fig. 4.1).

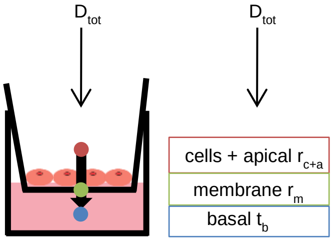

Figure 4.2: Compartments in the Transwell® insert setup. D_{tot} describes the cell-deposited aerosolized drug dose of the respective nanodrug. r_{c+a} describes the fractional amount of D_{tot} in the cells and (apically) attached to the cells. Furthermore, r_m describes the fractional drug dose attached to the perforated membrane on with the cells are grown. Finally, t_b describes the fractional amount of the drug in the basal compartment.

D_{tot} describes the cell-delivered dose of the drug after aerosolization of the respective nanodrug formulation. The transported amount of the drug into the basal compartment is described as t_b. For the membrane-only control, the dose, which was retained by the membrane, can be described by (1-1).

$$r_m = 1 - t_{b,0} \tag{1-1}$$

When cells are present on the membrane, the membrane itself and the cells build a barrier against drug transport into the basal compartment.

$$D_{tot} \cdot (1 - r_{c+a}) \cdot (1 - r_m) = t_b \tag{1-2}$$

Inserting (1-1) in (1-2) and setting D_{tot} as 100% result in equation (1-3):

$$r_{c+a} = 1 - t_b/t_{b,0} \tag{1-3}$$

D_{tot}:	Cell-delivered dose per Transwell® insert after nebulization
r_m:	Dose retained by the membrane

r_{c+a}:	Intracellular and cell-associated dose
t_b:	transmitted dose into the basal compartment when cells are present
$t_{b,0}$:	transmitted dose into the basal compartment for a membrane-only control

Thus, the dose of the drug in the cellular/apical compartment, which is referred to as cell-associated dose in the presented work, is the amount of the drug transmitted by the cell layer, normalized to the transmitted dose of the Transwell® insert membrane without any cells.

It is important to mention that this approach can be used to study the apical and cellular retained dose of aerosolized drugs. To calculate the cell-retained drug dose only, the following procedure was applied for Ptx-NP: The membrane was cut out after three washing steps with 0.9% NaCl from the Transwell® insert. Then, the membrane was taken up in 1.5 mL deionized water in a cup. This cup was frozen in liquid nitrogen and thereafter thawed in a water bath to achieve cell lysis. The procedure was repeated three times. The measured Ptx dose in the cup was then normalized to the cell-delivered Ptx dose (100% = (19.8 ± 1.5) µg). In addition, the Ptx storage of a membrane-only control was measured and subtracted from the cellular setups.

4.5 Functional Assays

The effects of the aerosolized nanodrugs on cellular parameters were assessed by several functional assays.

Metabolic activity (cellular viability) was analyzed by WST-1 assay. After a 15 min incubation period with the reagent, the conversion into formazan was analyzed via absorbance measurement at a wavelength of 490 nm. The absorbance was normalized to the absorbance of a sham control, which was exposed to the solvent of the used nanodrugs.

The inflammatory response of the A549-Luc(IL-8) cells was assessed by a luciferase assay system. Luciferase expression correlates to the activation of the IL-8 promoter in these cells [162]. After cell lysis and centrifugation, the luciferase assay reagent ONE-Glo™ was added to the supernatant. Thereafter, the bioluminescence was monitored and normalized to the total protein level. Then, the activity was expressed as fold increase compared to the sham control.

Lactate dehydrogenase (LDH) assay was performed to evaluate possible cytotoxic effects after cell exposure. The release of LDH was measured by an absorbance reader and normalized to the release of LDH by a cell lysate (high control = 100% cytotoxicity).

Barrier quality was assayed by using Blue Dextran 2000 as previously described by Horvath et al. (2015) [84]. In brief, the translocation of 0.5 mL 1% dextran blue solution in PBS from the apical into the basal compartment was measured after 2 h by an absorbance reader (Magellan) at 600 nm and normalized to the transport of the dye across a membrane without cells (= 100% dextran blue translocation). It is important to mention that cells were cultured at submerged conditions for the dextran blue assay with 1 mL phenol red free growth medium in the basal and 0.5 mL growth medium in the apical compartment, respectively.

Finally, An Epithelial Volt-Ohmmeter (EVOM) was used to measure the transepithelial electrical resistance (TEER) of the *in vitro* models of the air-blood barrier. The TEER technique is a method to validate the epithelial integrity and tightness [163].

For Ptx-NP, also mRNA expression of FoxO1 transcription as a hallmark of pulmonary hypertension was investigated in endothelial cells EA.hy926 as described in the next section.

4.6 RNA isolation and qPCR analysis

As described, an epithelial-endothelial coculture of A549-Luc(IL-8) and EA.hy926 cells was used for the Ptx-NP experiments.

To isolate the RNA of the endothelial cell line (EA.hy926), the Transwell® insert membrane was cut out. Then, 300 µL lysis buffer (Buffer RLT®) was added to the endothelial side of the membrane. After an incubation period of 10 min in the fridge, the endothelial cells were scratched off with a cell scraper. After that, the lysate was used to isolate the RNA with the RNeasy® Plus Mini Kit according to the manufacturer’s instructions. Finally, RNA concentrations were analyzed with a spectrophotometer (NanoDrop 1000®) before qPCR analysis in collaboration with project partners analogues to [19].

4.7 Study of mechanisms of cellular uptake

Pathways of cellular uptake of nanodrugs were analyzed by the use of inhibitors of caveolae-mediated endocytosis (Filipin), clathrin-mediated endocytosis (Pitstop-2) and pinocytosis (Amiloride). Concentration and incubation time (10 min) were adapted from a previously reported study [101]. These are summarized in table 4.1.

Table 4.1: Concentration of the applied cellular uptake inhibitors, adapted from Engelberg et al. (2018)[101]

	Concentration at submerged conditions (µM)	Mass dose per area (µg/cm²)*
Filipin	1.5	0.4
Pitstop-2	25	4.2
Amiloride	1000	81.2

* considering a medium volume of 60 µL and a cell growth surface area of 0.17 cm² using µ-Slides VI 0.1 by ibidi GmbH, Martinsried, Germany

However, the reported inhibitor concentrations for submerged cell culture experiments were converted into doses in the present study since dose rather than concentration governs the bioactivity of substances at ALI conditions [89]. Confluent A549-Luc(IL-8) cells on Transwell® inserts were incubated with 300 µL respective inhibitor directly on the cells for 10 minutes at 37°C. Mass doses as listed in table 4.1 were applied. Then, the cells were washed twice with PBS and exposed to aerosolized nanodrugs. To analyze possible inhibition, the cells were washed after exposure three times with 500 µL 0.9% NaCl at various time points. The drug dose was thereafter analyzed in the washout by fluorescence analysis.

4.8 Microscopy

To visualize the effects of the aerosolized nanodrugs on the cell morphology, the actin cytoskeleton of the cells was stained with boron-dipyrromethene (BODIPY) in 1% BSA in PBS for 1. Then, the mounting medium with DAPI was used to visualize the cell nuclei. Finally, the slides were visualized with the 40x objective on a fluorescence microscope (Olympus BX51).

The incorporation of FRET liposomes was visualized by the Cy3 filter of the microscope.

Live cell imaging was performed with cells on the Transwell® insert after the nebulization of the FRET liposomes. The inserts were placed in dishes with 1.5 mL growth medium suitable for microscopy (Nunc™ Glass Base Dish). An excitation wavelength of 490 nm and an emission wavelength of 700 nm (long pass) were used. Intensity settings and image analysis were performed with ImageJ or VisiView.

To visualize the pores of the Transwell® inserts, Scanning Electron Microscopy (SEM) was performed. The membrane of the inserts was cut with a scalpel and fixed in 6% (v/v) glutaraldehyde afterwards. Then, the membranes were dehydrated in gradient ethanol solutions followed by hexamethyldisilazane for 15 min. Next, parts of the membranes were mounted onto aluminum stubs and sputter-coated using a Leica EM ACE200 vacuum coater. Finally, the membranes were imaged by a Zeiss Crossbeam 240 electron microscope with an acceleration voltage of 2 kV. The SEM microscopy of the prepared samples was performed by Ali Doryab (Helmholtz Zentrum München) (figure 5.3).

4.9 Modeling of nanodrug deposition at submerged conditions

ALI exposure by the VITROCELL® Cloud 6 technology leads to direct deposition of Ptx-NP on cells. For comparison with results from cell culture experiments under standard submerged cell culture conditions (Figure 1.4), one has to consider that at submerged conditions, nano- and micro particles are pipetted into the cell culture media and initially uniformly dispersed throughout the entire medium volume. Depending on the size, shape and density of the NPs as well as the height of the medium column in the well (typically 0.3 – 0.5 cm), it can take between a few minutes to a few days until all of the available NPs are deposited onto the cells at the bottom of the well [164]. Thus, the fraction of the particles that reach the cells at submerged cell culture conditions was calculated with the sedimentation, diffusion and dosimetry model (ISDD) described by Hinderliter et al. (2010)[164], which allows the calculation of cell-delivered doses. The input parameters to calculate the deposition fraction of Ptx-NP at submerged conditions are summarized in table 4.2.

Table 4.2: Summary of the input parameters for the ISDD model for determination of cell-delivered Ptx-NP dose at submerged cell culture conditions

	Value	**Reference**
Volume-weighted median diameter of Ptx-NP (nm)	260	-
Area of the Transwell® insert (cm²)	4.2	Costar® Manual
Effective material density of polymeric nanoparticles (g/cm³)	1.25	Vauthier et al. (1999) [165]
Height of the cell culture medium on top of the cells (cm)	0.48[a)]	-

a) $h = V/A = 2\ cm^3/4.2\ cm^2 = 0.48\ cm$

The ISDD modeling according to Hinderliter et al. (2010)[164] was performed by Dr. Ali Farnoud (Helmholtz Zentrum München).

4.10 Matching *in vitro* and *in vivo* data with focus on PK

Inhalation of aerosolized nanodrugs leads to lung deposition and time-dependent partial transport into the blood [21], which is referred to as PK. Here, the term lung-to-blood transport was introduced to describe the drug fraction transported from the lung into the blood. The lung-to-blood transport was assessed *in vitro* by aerosolization of L-CsA on A549-Luc(IL-8) cells (= “lung”) and measuring the CsA translocation into the basal medium (= “blood).

To match the *in vitro* findings with *in vivo* human (i.e. clinical) data, serum CsA levels after inhalation (published by Kappeler et al. 2020[166]) and the peripheral lung deposition of L-CsA (published by Behr et al. 2009[17]) were used. This was done with a relatively simple computational approach, which is henceforth referred to as “simple discrete modeling”. This modeling approach included three compartments (lung, blood, and “loss compartment” (e.g. liver)), which are summarized in figure 4.2B

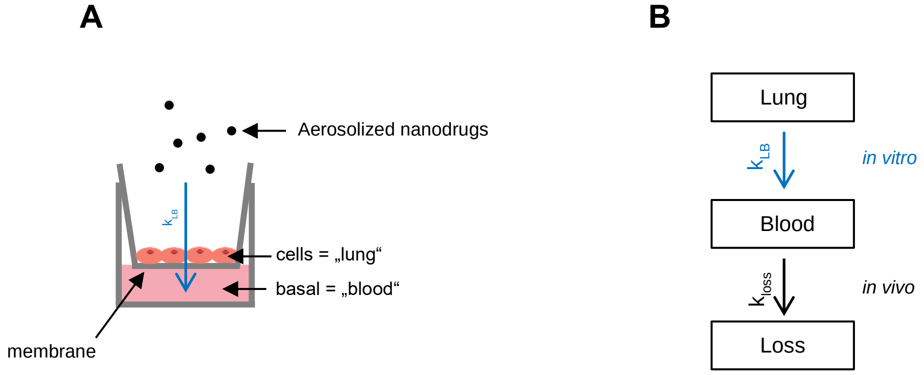

Figure 4.3: A relatively simple physiologically based PK (PBPK) model which relies on cell-based *in vitro* transbarrier transport rates to predict *in vivo* pharmacokinetic data of inhaled (nano-)drugs. **Panel A**: Nanodrugs (L-CsA and Ptx-NP) were nebulized onto an alveolar epithelial cell barrier model (A549 w/o EA.hy926) at the ALI. Then, transbarrier transport of the drugs from the apical side into the basal medium was measured to obtain the *in vitro* transport rate k_{LB}. **Panel B**: Combined with the loss rate of the drug from the blood (k_{loss}), which can either be obtained from *in silico* models or from *in vivo* data, the PK profile of the drugs in humans can be predicted (adapted from Bachler et al. (2015)[52]).

A similar, but more complex multi-organ approach was presented by Bachler et al. (2015) [52], who focused more on the multi-organ distribution of inhaled NPs rather than the blood concentration. The governing equations and the numerical approach of solving them are described in the Appendix for L-CsA as example.

A conceptually similar but more advanced PBPK model was implemented in collaboration with Dr. Ali Farnoud (Helmholtz Zentrum München) using a Python™ code to solve the inter-compartmental transport equations (figure 5.11). This model was adapted from Weber and Hochhaus (2013)[56]. Besides the three compartments, which were used in the simple modeling approach described above, a remainder compartment was introduced. This compartment described the kinetics of absorption of CsA from and release of CsA to the plasma induced by the rest of the body (everything except lung, blood and secretion organs).

4.11 Statistical analysis

Results are presented as mean from biological replicates and error bars typically represent the SEM from three biological replicates unless stated otherwise. In addition, fluorescence (FRET liposomes) and absorbance of products in functional assays (LDH, WST-1, dextran blue) was measured in four technical replicates. For TEER measurements, three positions of the electrodes per condition were measured.

A one-way analysis of variance (ANOVA) was conducted to test the statistical significance of endpoint measurements (24 hours). To analyze statistical significance from data as a function of time (e.g., in biokinetics studies), a two-way ANOVA was used. Statistical significance was indicated by stars: * $p \leq 0.05$, ** $p \leq 0.01$, *** $p \leq 0.001$, **** $p \leq 0.0001$. SigmaPlot was used for obtaining regression parameters in simple discrete PBPK modeling. GraphPad Prism 8.0.0 was used for statistical analysis and generation of graphs.

5 Results

5.1 Transbarrier transport of Cyclosporine A-laden liposomes (L-CsA)

One of the goals of this study was to analyze the transbarrier transport of aerosolized liposomal Cyclosporine A (L-CsA) across A549-Luc(IL-8) cells cultured Transwell® inserts and its translation into the corresponding clinical PK profile of L-CsA. The study was carried out in three steps, which are

1) Validation of the dose-controllable delivery of L-CsA by the VITROCELL® Cloud 6 system
2) Analysis of the CsA transport across an A549-Luc(IL-8) monolayer cultured on Transwell® inserts as a model of the air-blood barrier
3) Finding possible differences in the CsA transport under conditions leading to a loss of epithelial integrity
4) Bridging gaps between the *in vitro* findings and clinical data by computational approaches

5.1.1 Evaluation of dose-controllable delivery of L-CsA

To allow a dose-controllable delivery of aerosolized liposomal Cyclosporine A (L-CsA) to the *in vitro* model of the air-blood barrier, the deposition of L-CsA was assessed by the quartz crystal microbalance (QCM) of the VITROCELL® Cloud 6 system. The QCM was placed in one of the wells and the active quartz crystal was located at the exact position of the cells cultured in Transwell® inserts. Thus, the dose measured by the QCM is equal to that of the exposed epithelial cells [93]. The stock suspension of L-CsA (15.1% (w/v) in 0.25% (w/v) NaCl was diluted in several steps, and the cell-deposited dose for each dilution was assessed by the QCM. First, the expected fractional nanodrug deposition for nebulization of 200 µL of 15.1% (w/v) L-CsA was calculated from the QCM-measured mass dose per area (scaled to the total area of the VITROCELL® Cloud 6 chamber (146.56 cm²)) and compared to the theoretically possible value, if 100% of the invested drug would reach the bottom of the Cloud system.

This yielded a deposition factor of 0.69 (figure 5.1A), i.e., 69% of the invested drug deposited on the bottom of the Cloud chamber, where the cells are located. Using this information, the cell-deposited L-CsA dose can be calculated from the concentration of the L-CsA suspension. It could be shown that for a series of different L-CsA concentrations (between 3.0 and 75.5 mg/mL), the expected and the L-CsA deposition assessed by the QCM correlated with r > 0.99 (figure 5.1B). Hence, the cell-deposited L-CsA dose can be targeted by selecting the appropriate concentration of the L-CsA suspension. Nevertheless, as measure of quality control the QCM always served as additional measure of dose monitoring during VITROCELL® Cloud exposure experiments.

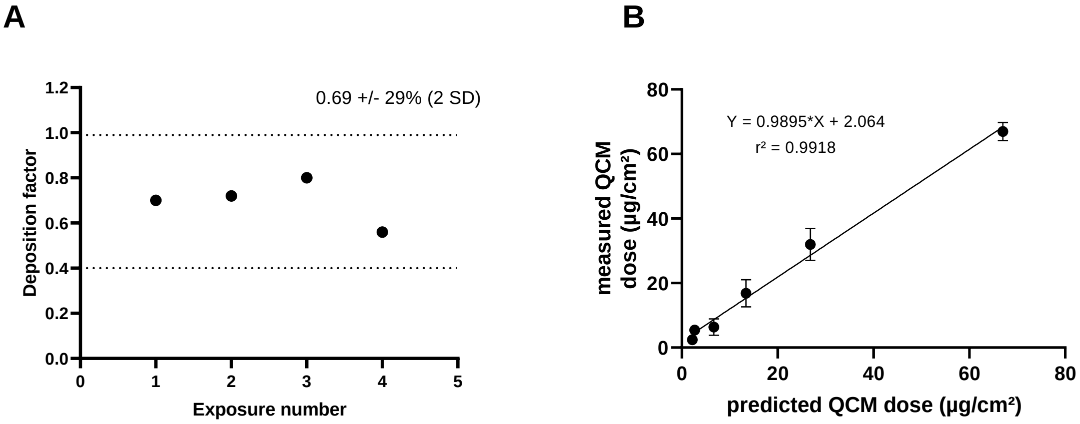

Figure 5.1: Assessment of L-CsA deposition in the VITROCELL® Cloud 6 System with a quartz crystal microbalance (QCM). **Panel A**: A mean deposition factor of 0.69 was obtained. Accordingly, 69% of the L-CsA dose in the nebulizer was evenly distributed on the bottom of the VITROCELL® Cloud exposure chamber, where the cells are located. **Panel B**: Linear regression analysis of QCM-measured and deposition factor-predicted L-CsA dose for all of the formulation ingredients (cell-delivered dose) over the entire dynamic range (1 – 70 µg/cm²). Since the fractional dose of CsA in the formulation is 0.057%, a QCM dose of 70 µg/cm² corresponds to a CsA dose of 0.04 µg/cm². Thus, the VITROCELL® Cloud 6 technology was capable of detecting the cell-delivered L-CsA dose. Error bars represent the SEM from three independent experiments.

5.1.2 Transbarrier L-CsA transport studies

After the dose-controllable delivery of L-CsA by the VITROCELL® Cloud 6 system was ensured, the transbarrier transport of CsA across A549-Luc(IL-8) cells cultured at the ALI was investigated next. As mentioned above, the model is characterized by three compartments (figure 5.2A): the apical compartment (contact side of the cells with the air), the basal compartment (medium below the cells), and the cell compartment (cells on Transwell® inserts).

For the transport studies, 500 µL of a 15.1% (w/v) L-CsA stock solution was applied in aerosolized form to the cells with the VITROCELL® Cloud 6 system yielding a cell-delivered CsA dose of 2.4 ± 0.3 (SD) µg/cm^2. The CsA concentration in each compartment (after dissolution of the liposome with a detergent) was assessed for a monitoring period of 24 hours and normalized to the total amount of CsA per Transwell® insert.

The fractional CsA dose in the basal (blood) compartment for the setup with cells significantly increased from 3% to 62% (Fig. 5.2B, blue line) over the entire monitoring period. Interestingly, a similar maximum fractional CsA dose of 68.5% in the basal compartment was also found for the membrane-only control (black line) during the entire time period (even the earliest time point of 7 min). This indicates that the membrane itself retains ca. 32 % of the delivered CsA dose independent of the presence of the cells. For the assessment of fractional transcellular transport of CsA, this needs to be taken into account, by normalizing the fractional basal CsA dose to 0.68, the maximal possible value for aerosol transport measurements with the type of Transwell® inserts used here. A more detailed derivation of this numerical correction was presented in the methods section. With this correction, only weak CsA apical and cell-association (5%,) was found after 24 hours (figure 5.2C, red line). On the other hand, 88% of the theoretical expected CsA dose was transported across the cell barrier within 4 h without significant increase at 24 h (figure 5.2C, blue line).

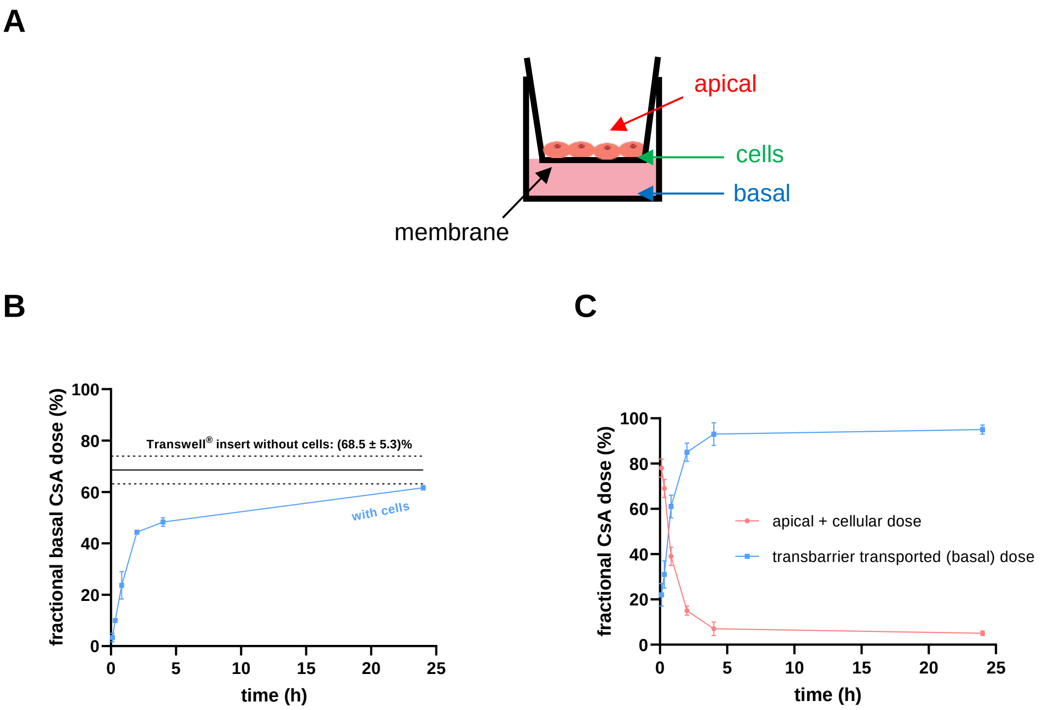

Figure 5.2: Biokinetics of liposomal Cyclosporine A (L-CsA) across the compartments of A549-Luc(IL-8) cells grown on Transwell® inserts. **Panel A:** Schematic depiction of the different Transwell® insert compartments for which the drug dose was determined. **Panel B:** The fraction of CsA in the basal compartment (with cells) was increasing with an initial burst (steep slope, blue line) to a maximum value of 62%. The membrane itself (without cells) retained 31.5% of the delivered CsA (black line), but the corresponding basal CsA fraction of 68.5% was reached immediately after nebulization. **Panel C:** Same data as in panel B, but corrected for the influence of the membrane on the maximal possible basal dose. The blue line represents the translocation into the basal compartment corrected for the membrane influence. The red line represents the fractional CsA dose in the apical and cell compartment. There was only slight cell-association of CsA as 88% of the theoretically possible CsA dose per insert was found in the basal medium after 24 h (and even after 4 h). Data are normalized to the total CsA dose per Transwell® insert ((10 ± 1) µg) and presented as mean ± SEM (n = 11 independent experiments).

To understand the reason for the membrane retained CsA dose on the Transwell® insert, the membrane was visualized by scanning electron microscopy (SEM) (figure 5.3). The SEM analysis revealed a highly non-uniform distribution of the $8 \cdot 10^5$ pores/cm^2 (Corning Falcon® manual) with 3.0 µm diameter resulting in a relatively low porosity of 5.65% of the total Transwell® insert area (4.2 cm^2). Combined with the relatively non-uniform distribution of the pores, this results in numerous non-porous regions with a cross sectional dimension of

30 µm and more. Aerosol droplets of ca. 5 µm diameter depositing in these regions will not be able to transfer their nanocarriers through the membrane, which explains the measured membrane retained dose of 31.5%.

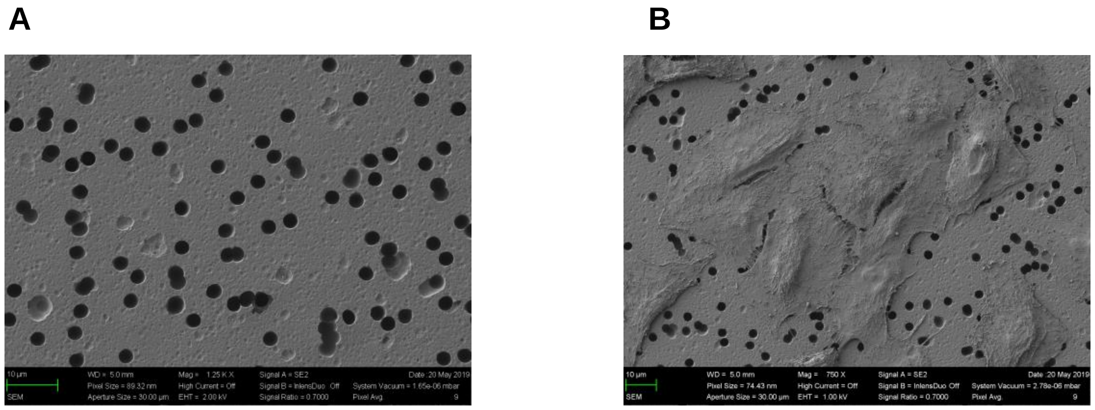

Figure 5.3: Scanning electron microscopy pictures of a membrane-only control **(Panel A)** and an insert membrane with A549-Luc(IL-8) cells **(Panel B)**. Areas, which are not stamped by pores, were evident. Accordingly, the storage of an aerosolized drug is also possible in the cell-free setup. Non-confluency in panel B is visible due to sample preparation. Scale bars are 10 µm.

5.1.3 Transbarrier transport of L-CsA across an inflamed model of the air-blood barrier

To analyze L-CsA transport across the air-blood barrier model under inflammatory conditions, A549-Luc(IL-8) cells were challenged with different TNF-α doses added from below (basal compartment) 24 h before the exposure to L-CsA.

The addition of TNF-α significantly influenced the barrier integrity of the model. ZO-1 prevalence decreased 1.4-fold for 16.1 ng/cm^2 (figure 5.4, quantification in figure 5.5), which was correlated with a 4.0-fold increase in epithelial permeability for the paracellular transport marker dextran blue (figure 5.6A). The IL-8 activity of the cells increased up to 100-fold (relative to unchallenged control) in a TNF-α concentration-dependent manner (figure 5.6B), showing pro-inflammatory activation of the epithelial cells. On the other hand, their metabolic activity was not decreased for any of the tested TNF-α doses (figure 5.6C), which is a prerequisite for the conduction of reliable biokinetics studies. Hence, the L-CsA biokinetics studies with pro-inflammatory stimulated cells were performed with the highest TNF-α dose of 16.1 ng/cm^2.

As seen in figure 5.7D, even severely pro-inflammatorily stimulated A549 cells (100-fold IL-8 induction) did not affect the temporal profile of the cell-associated CsA dose (apical plus cell compartment) and hence also not the transbarrier transport of L-CsA across the inflamed alveolar epithelial barrier model (figure 5.7D). Since paracellular transport was 4-fold enhanced under those conditions, this indicates that CsA is not transported across the cell barrier via the paracellular route.

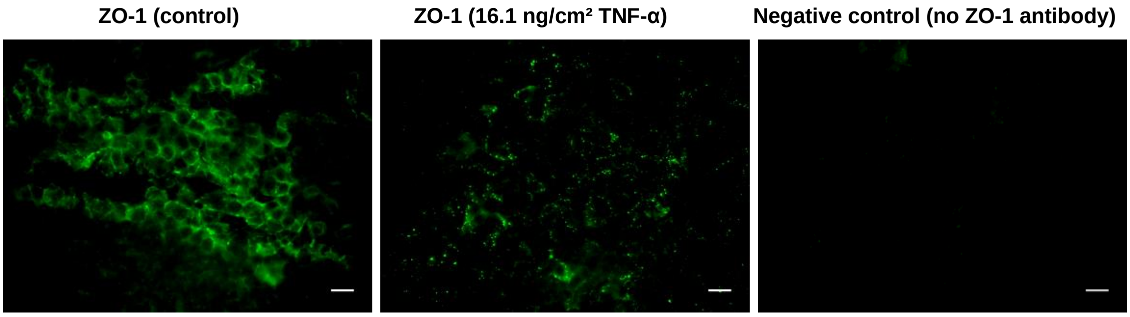

ZO-1 (control)

ZO-1 (16.1 ng/cm² TNF-α)

Negative control (no ZO-1 antibody)

Figure 5.4: Tight junction (ZO-1) staining of A549-Luc(IL-8) cells. **Panel A:** ZO-1 staining without TNF-α (unchallenged control). **Panel B:** Reduced ZO-1 expression after addition of 16.1 ng/cm^2 of TNF-α via the basal medium (24 h incubation time) relative to unchallenged control. **Panel C:** Negative (technical) control without the addition of a primary antibody against ZO-1. Scale bar: 10 µm

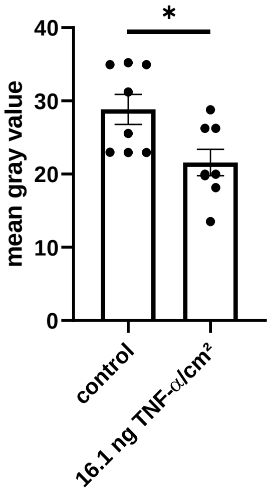

Figure 5.5: Quantification of ZO-1 staining (figure 5.4) with ImageJ. * $p \leq 0.05$

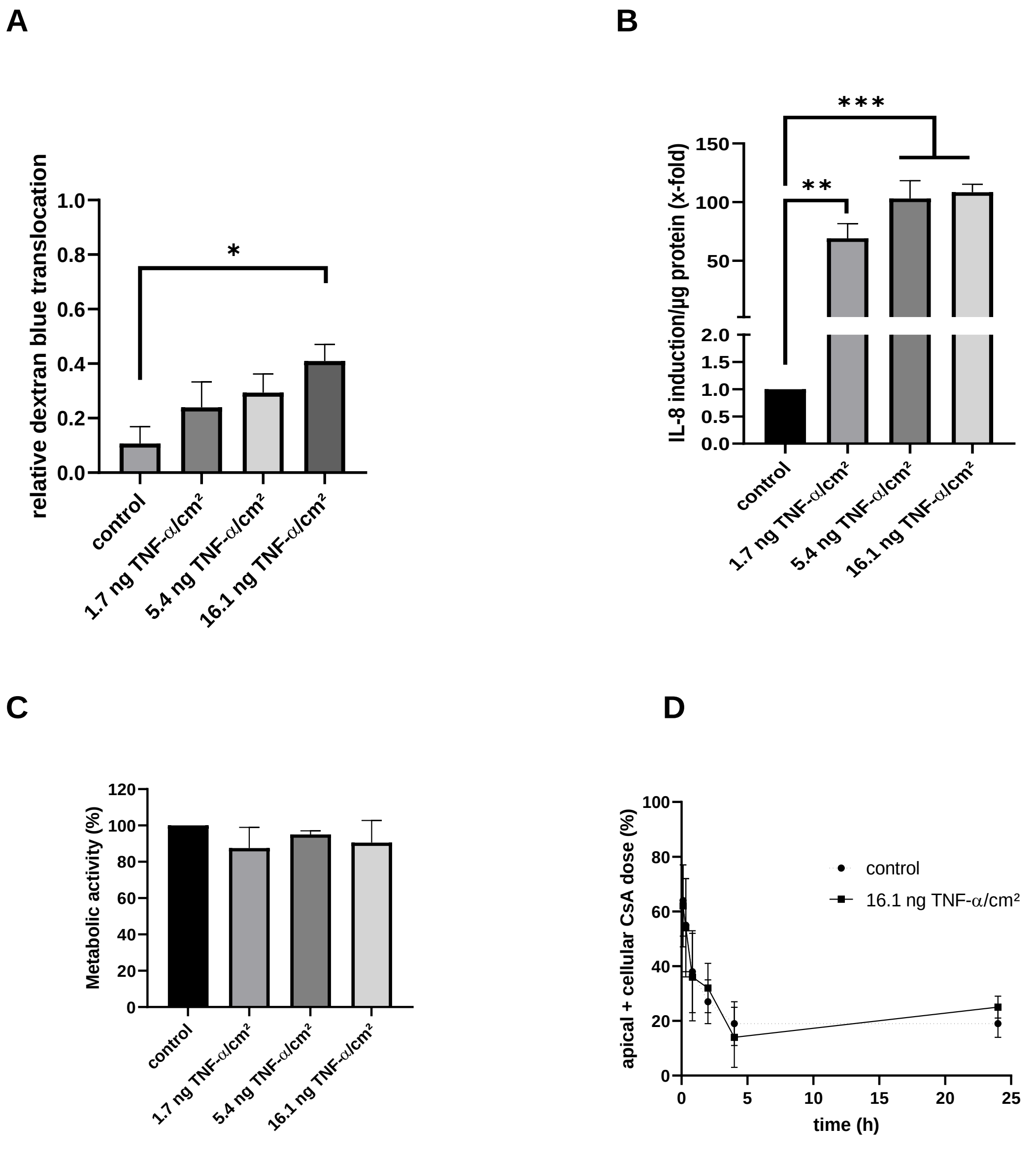

Figure 5.6: Effects of pro-inflammatory challenge via TNF-α incubation (24 h) on IL-8 expression (promotor activation), barrier integrity, metabolic activity, and L-CsA biokinetics of A549-Luc(IL-8) cells. **Panel A:** Compared to the negative control, there was a statistically significant (4-fold) increase in paracellular barrier permeability for the highest TNF-α dose only. **Panel B**: TNF-α induced a dose-dependent up to 100-fold activation of the IL-8 promoter (as compared to the negative control), which was statistically significant even for the lowest dose ($p < 0.0075$). **Panel C:** There was no decrease in metabolic activity (WST-1) up to the highest TNF-α dose of 16.1ng/cm^2. **Panel D:** L-CsA biokinetics across A549-Luc(IL-8) cells, which were challenged with 16.1 ng/cm^2 TNF-α 24 hours before exposure to L-CsA. Although the paracellular barrier integrity for large molecules was reduced by a factor of four (panel A), the CsA dose associated with the cells (apical+cellular compartment) was not decreased as compared to unchallenged control. Data are normalized to the total CsA dose per Transwell® insert ((11 ± 1) µg) and presented as mean ± SEM (n = 3 independent experiments). * $p \leq 0.05$, ** $p \leq 0.01$, *** $p \leq 0.001$, **** $p \leq 0.0001$

5.1.4 Matching *in vitro* CsA transbarrier transport rates with the clinical CsA PK profile after inhalation

The *in vitro* results presented in the previous paragraphs will now be put into context with clinical L-CsA PK data.

Clinical pharmacokinetic data of L-CsA (time course of CsA serum levels) were published by Breath Therapeutics GmbH[166]. In this study, double-lung transplant patients inhaled 10 mg L-CsA as 0.4% (w/v) L-CsA suspension, which is identical to the one used for *in vitro* testing in the present work, and CsA plasma levels were monitored from 15 min to 24 h after inhalation (figure 5.7). The PK profile showed a concentration maximum of 57.42 ng/mL in the blood, but the monitoring time did not start early enough to reveal the peak concentration (c_{max}) and the associated time (T_{max}) until peak concentration is reached, which are key parameters of PK profiles [166].

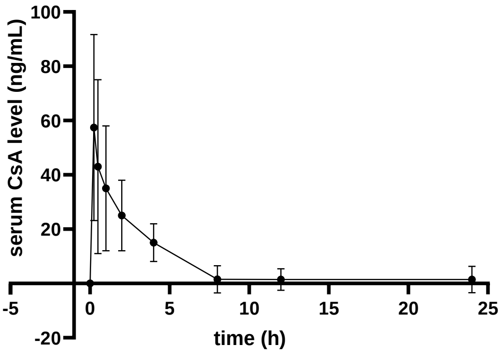

Figure 5.7: Pharmacokinetic profile of inhaled L-CsA in double-lung transplant patients. The maximum CsA plasma concentration of 57.42 ng/mL is reached at the earliest sampling time (15 min). The plasma concentration of 0 ng/mL at 0 min equals the plasma level 15 min prior to the start of the inhalation. These data were obtained by Breath Therapeutics GmbH and published in [166]. Error bars represent the mean ± SD of CsA plasma concentrations of n = 7 patients.

For translation of the *in vitro* into the *in vivo* (clinical) data, various modeling approaches were used. For the first *simple discrete modeling*, three compartments were introduced according to Figure 5.10:

1) Lung compartment, in which L-CsA deposits after inhalation (here: *in vitro* and *in vivo* parameters were used)
2) Blood compartment, which describes the lung-to-blood transported amount of CsA, leading to a dose in the blood (PK) (predicted from *in vitro* parameters and compared to *in vivo* results).
3) Loss (removal) compartment, which describes the depletion of CsA in the blood as a result of metabolic CsA degradation and/or excretion (here, *in vivo* parameters were applied).

For connection of *in vitro* input parameters with the clinically observed CsA blood concentrations the following steps were performed:
First, the lung deposited L-CsA dose in lung transplant patients was obtained from the L-CsA inhalation study by Behr et al. (2009) [17], which was conducted with the same type of L-CsA (from Breath Therapeutics, formerly Pari Pharma, Germany) and a similar type of nebulizer (eFlow, vibrating mesh nebulizer, Pari Pharma) as was employed in our *in vitro* study. Behr et al. (2009) reported a peripheral L-CsA lung deposition of 22% of the nominal dose (here: 2.2 mg) from radiometric measurements [17].
Second, L-CsA transport rates across the air-blood barrier of the lung were derived from the *in vitro* data reported in chapter 5.1.2. The time-dependent transport rates k_{LB} across the A549-Luc(IL-8) cell (lung) barrier corresponds to the slope of the basal CsA profile reported figure 5.2C. In this simple discrete modeling, the k_{LB} was calculated for each time layer by dividing the fractional change in basal CsA dose of adjacent measurement points by the corresponding time interval. It is evident from figure 5.8 that the resulting transport rates were about constant at 1.42/h during the first two hours of the *in vitro* experiment. At 4 h, the transport rate dropped by a factor of 3.5, reaching zero within experimental uncertainties for 8 h and later. This rapid drop in k_{LB} is likely due to exhaustion of the CsA dose available in the donor compartments (apical, cell). These lung-blood transport rates k_{LB} represent the fractional CsA dose per time (relative to the time-dependent CsA dose in the associated with the epithelial cells/lung), which is transported from the cells (lung) into the medium (blood) for *in vitro* (*in vivo*) conditions.

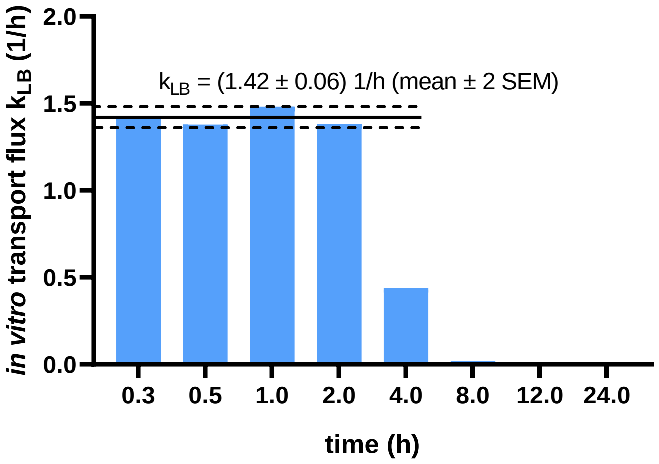

Figure 5.8: The calculated L-CsA *in vitro* transport rates k_{LB} from the lung into the blood were constant (1.42 1/h) during the first 2 h of the *in vitro* experiment (figure 5.2C). At 4 h, the transport rate dropped by a factor of 3.5 and reached zero (within experimental uncertainties) at 8 h.

Third, a mean fractional loss rate k_{loss} of 0.51/h of CsA from the blood was calculated analogously to step 2 using the later time points of the L-CsA profile of our clinical PK data and taking the average value over all time points (figure 5.9).

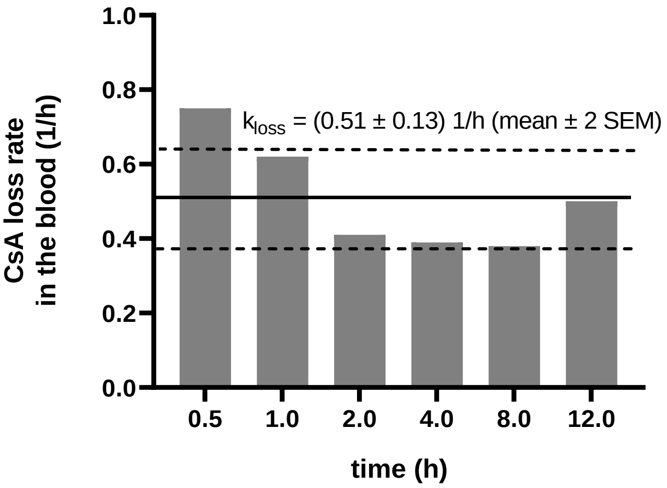

Figure 5.9: The relative loss rate of 0.51/h serum CsA was calculated from the later time points of our clinical PK data (0.51/h) (Figure 5.7).

Starting from the initial conditions of 2.2 mg L-CsA in the lung (all other compartment contain initially zero L-CsA) and an assumed human blood volume of

5.75 L [167], the equations listed in Appendix A.1 were applied for each time layer of the clinical PK data (figure 5.7), and the resulting CsA PK data (figure 5.10B, blue line) were plotted together with the clinical data (figure 5.10B, grey line). It is evident that the modeled and the measured values agree within estimated experimental and modeling uncertainties of factor of 2 for the first two hours. However, they deviate for later times since the modeled curve decays much faster than the measured one.

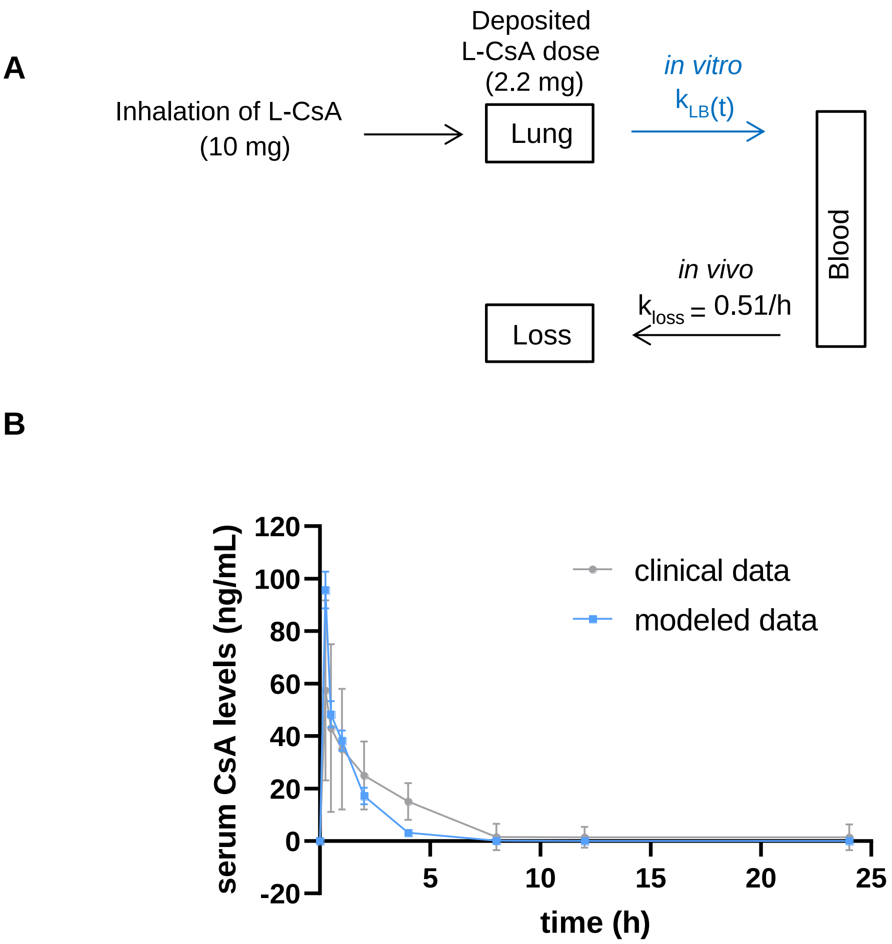

Figure 5.10: Simple discrete modeling of the PK of inhaled L-CsA and comparison to clinical data for lung transplant patients. **Panel A:** Scheme of simple discrete modeling approach and the *in vitro* and *in vivo* derived transport rates of CsA from the lung into the blood (k_{LB}) and out of the blood (k_{loss}). **Panel B:** Comparison of modeled (grey) and measured (blue) PK curves, which showed agreement within estimated experimental uncertainties (ca. factor of 2) at least within the first two hours, which are most important for calculating the systemically available L-CsA dose (clinical data from Figure 5.7). Error bars for the modeled data were calculated applying Gaussian error propagation on the *in vitro* L-CsA transport rates (figure 5.2B).

One of the main over-simplifications made in the *simple discrete modeling* approach is that the initial sequestering of some of the L-CsA in the blood in the entire rest of the body (remainder) and its subsequent gradual (partial) release from there into the blood is not included in the model. In the advanced modeling approach, this compartment (remainder) was included (figure 5.11A) and the resulting transport equations (Appendix A.2) were numerically solved with a Python program written by Dr. Ali Farnoud (member of research group of Dr. Otmar Schmid, Helmholtz Zentrum München). The transport rates from the blood into the remainder (k_{BR}) and vice versa (k_{RB}) were obtained by minimizing the difference between modeled and measured L-CsA concentrations in the blood (figure 5.11B). It is evident that there is excellent agreement between modeled and measured L-CsA PK profile for the first two hours (model 1 and model 2) and even over the entire modeling period of 8 h if the remainder compartment is included (model 2).

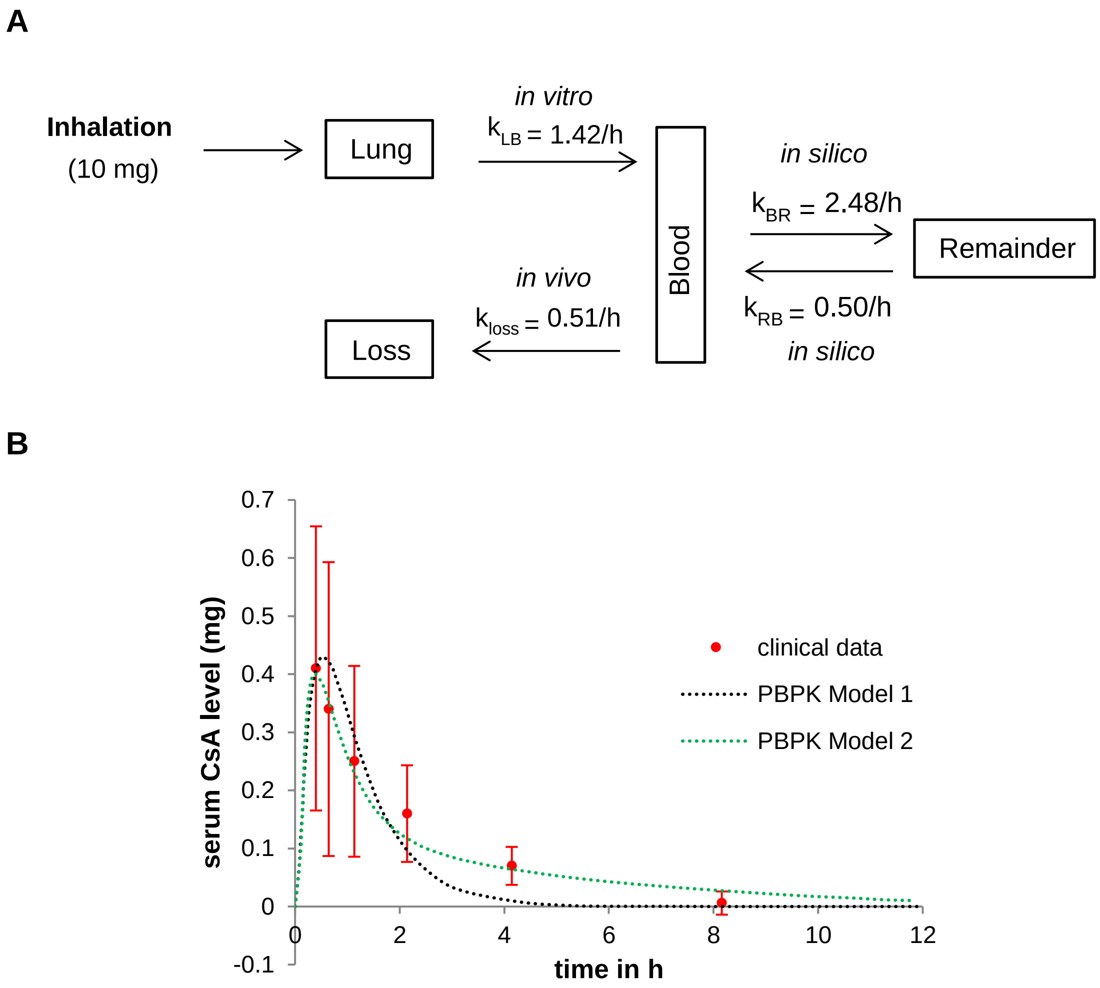

Figure 5.11: Advanced PBPK models for inhaled L-CsA and comparison to clinical data for lung transplant patients. **Panel A:** Scheme of advanced PBPK modeling approaches using (infinitely) small time steps (continuous modeling) and up to four compartments, namely lung, blood, loss (removal), and remainder (rest of body) compartment (model 2). For model 1, the remainder compartment was not considered (analogous to *simple discrete modeling*). The lung, blood, and loss transport rates were adopted from the *simple discrete modeling* (see figure 5.10) and the transport rates in and out of the remainder (rest of body) were obtained by numerical minimization of the difference between modeled and measured L-CsA blood concentrations. **Panel B:** Comparison of modeled (dotted lines) and measured (red symbols) PK curves shows excellent agreement over the entire modeling period (up to 8 h) for model 2 (with remainder), but much less good agreement for time points later than 2 hours, if the remainder is not included (model 1) (clinical data from Figure 5.7).

This demonstrates that *in vitro* transport rates obtained with the VITROCELL® Cloud 6 technology can serve as useful (physiologically-based) input parameter for simple and advanced PBPK modeling of inhaled L-CsA.

5.2 Prediction of clinical maximum drug plasma concentration in inhalation therapy

Currently, *in vitro* transbarrier transport data are limited to a very small number of drugs and t for submerged cell culture models, which results in a slower *in vitro* kinetics profile as reported for ALI conditions [74]. Hence, it is unclear if these data can be used for the prediction of the clinical outcome at all.

In an effort to shed light on the effect of different types of inhaled drugs (with/without carrier systems) and of the role of drug carriers on PK curves, published clinical PK profiles, which reported the maximum (peak) drug concentration in the blood c_{max}, were investigated in this thesis (table 5.1). The data comprise eleven different studies using five different types of drugs (Levofloxacin, Tobramycin, Ciprofloxacin, Ciclosporin A, and Amikacin), one of them without liposomes (Ciclosporin A), one of them with a mixture of free and liposomal drug (Ciprofloxacin) and two with a liposomal formulation (liposomal Amikacin, liposomal Ciclosporin A). Most of the drugs were part of the treatment regimen for cystic fibrosis (CF) patients, but Ciclosporin A and Ciprofloxacin were inhaled by post-lung transplant patients (prevent bronchiolitis obliterans, BOS) and non-CF bronchiectasis, respectively. It is also important to note, that four different types of nebulizers were employed, including a so-called “investigational” eFlow (Pari, Munich, Germany), a vibrating mesh nebulizer optimized by Pari for each of the specific drugs (used in 7 studies), as well jet nebulizers (Pari LC Plus, “sidestream, disposable jet nebulizer”) and an ultrasonic nebulizer (Wisto Senior). Considering that all of these nebulizers have different output rates, droplet size distributions, delivery efficiencies, and that patients can have very different ways of applying/handling a nebulizer, it can be expected that for a given drug dose in the nebulizer, the lung-delivered dose is likely to vary by at least a factor of 2 [168].

The eleven c_{max} levels of the different drugs were plotted against the dose of the drug in the nebulizer, henceforth referred to as nominal dose (figure 5.12). Shapiro-Wilk test revealed a Gaussian distribution of the entire data set ($p = 0.30$). The data were fitted with linear regression curves forced through zero (intercept = zero) and the fits were plotted for each individual drug type (dashed lines) and for all of the data as a whole (black line), excluding levofloxacin for reasons discussed below. With $R^2 = 0.92$ for the overall fit, it can be said that 92% of the variability of c_{max} can be related to the variation of the nominal dose). In other words, the nominal dose in the nebulizer is a strong determinant of the maximum plasma concentration not only for a specific type of drug, nebulizer, and disease type/state but even independent of all of these parameters. Accordingly, one of the most important PK parameters, namely c_{max}, can be approximately predicted from

$$c_{max} = \frac{2.7 \cdot 10^{-6}}{mL} \cdot D_{nom} \tag{5-1}$$

with D_{nom} and 2.7×10^{-6}/mL representing the nominal dose (drug dose in nebulizer) and the slope of the “all data” linear regression presented in figure 5.12, respectively.

The observed ratio of c_{max} and nominal dose (slope) varies between $1.7 \cdot 10^{-6}$ and $3.4 \cdot 10^{-6}$ mL^{-1} (mL^{-1} = ng/mL/mg) with free and liposomal Ciprofloxacin and Tobramycin marking the lower and upper bound, respectively (figure 5.12). This 2-fold spread is surprisingly small considering the expected substantial variability induced by numerous parameters, including the use of different types of drugs and nebulizers as well as differences in disease type and state and proficiency of nebulizer handling by the patient. For Levofloxacin, an extremely large slope of $7.1 \cdot 10^{-6}$ mL^{-1} was observed, which is more than 2-fold larger than the maximum slope of the other drugs. The inclusion of Levofloxacin into the overall (“all data”) linear regression analysis would have substantially weakened the quality of the linear regression analysis performed for the remaining nine studies. Possible reasons for this “poor” agreement of Levofloxacin with the other drugs will be discussed in the discussion section.

Table 5.1: Summary of the maximum drug concentration c_{max} in the blood of patients after inhalation with a nebulizer. The nominal dose refers to the dose in the nebulizer.

Therapeutic drug	**Nominal dose (mg)**	**nebulizer**	**hydrophilic/hydrophobic**	**Cmax (ng/mL)**	**Ratio c_{max}/nominal dose (10^{-6} mL^{-1})**	**Patient characteristics**	**Ref.**
Levofloxacin	180	investigational Pari eFlow	intermediate lipophilic	1280	7.1	CF patients, FEV1 60 - 70%	Geller 2011 [169]
Levofloxacin	240	investigational Pari eFlow	intermediate lipophilic	1710	7.1	CF patients, FEV1 60 - 70%	Geller 2011 [169]
Tobramycin	300	Pari LC Plus (jet nebulizer)	hydrophilic	1120	3.7	CF patients, FEV1 > 40%	Geller 2003 [170]
Tobramycin	374[a]	ultrasonic nebulizer (Wisto Senior)	hydrophilic	1270	3.4	CF patients, FEV1 ~ 30%	Touw 1997 [171]
Liposomal Cyclosporine A	10	investigational Pari eFlow	hydrophobic	57.4	5.7	lung transplant patients	Breath Therapeutics [166]
Cyclosporine A	214.7[a]	Sidestream disposable jet nebulizer	hydrophobic	371.7	1.7	lung transplantation, FEV1 > 70%	Corcoran 2014 [158]
Liposomal Amikacin	70	investigational Pari eFlow	hydrophilic	220	3.1	tabular results ,CF, FEV1 ~ 60%	Clancy 2013 [172]
Liposomal Amikacin	140	investigational Pari eFlow	hydrophilic	380	2.7	tabular results, CF, , FEV1 ~ 60%	Clancy 2013 [172]
Liposomal Amikacin	280	investigational Pari eFlow	hydrophilic	950	3.4	tabular results, CF, FEV1 ~ 60%	Clancy 2013 [172]
Liposomal Amikacin	560	investigational Pari eFlow	hydrophilic	1290	2.3	tabular results, CF, FEV1 ~ 60%	Clancy 2013 [172]
Mixture of free and liposomal Ciprofloxacin	210[b]	Pari LC sprint nebulizer	hydrophobic	180	8.6	Non-cystic fibrosis bronchiectasis patients, FEV1 > 25%	Fröhlich 2017 [173]

a) emitted dose

b) 150 mg liposomal Ciprofloxacin + 60 mg free Ciprofloxacin

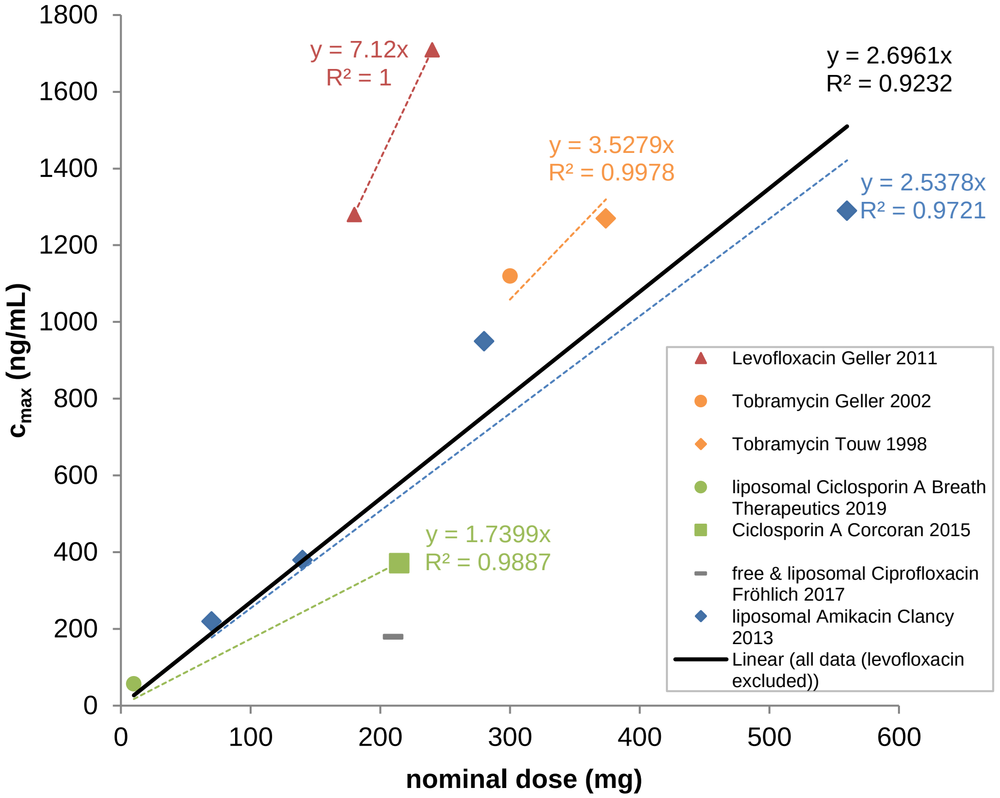

Figure 5.12: The maximum plasma concentration of an inhaled drug correlates well (solid line, r = 0.96) with the nominal drug dose in the nebulizer (data from table 5.1). Levofloxacin was considered as outlier due to the observed high c_{max} levels. Shapiro-Wilk test showed the normality of the data.

Table 5.1 and figure 5.12 also contain data from both liposomal CsA (L-CsA) and molecular CsA. For molecular CsA, the ratio of c_{max} to nominal dose (D_{nom}) is 1.7, which is relatively similar (1.6-fold lower) to the slope of the overall regression curve (2.7). On the other hand, for L-CsA the c_{max} to D_{nom} ratio of 5.7 is 2.2.-fold larger than the slope of the overall regression curve. Thus, the c_{max} values from both molecular and liposomal CsA can be predicted within a factor of 2.2 from equation 5-1.

It is also noteworthy that the c_{max} to D_{nom} ratio for liposomal CsA is 3.4-fold larger than that of molecular CsA. Thus, liposomes appear to enhance somewhat but not drastically lung-blood transport of hydrophilic drugs such as CsA. This indicates that the c_{max} of inhaled CsA can be predicted quite well (within a factor of ca. 2) from the nominal dose in the inhaler based on the slope from the overall data analysis ($c_{max} = 2.7 \times 10^{-6}/\text{mL}\ D_{nom}$ with D_{nom} representing the nominal dose). One hypothesis for why liposomal CsA may actually reach the blood faster than molecular CsA could be that liposomal CsA formulations releases the CsA molecules once the liposomes reach the epithelial barrier. However, it is not clear, if this is really what happens with liposomal CsA. In order to further investigate the transport mechanisms associated with liposomal CsA, fluorescently labeled (FRET) liposomes were manufactured and leveraged to shed light on this issue.

5.3 Manufacturing of FRET liposomes for cellular uptake studies

In the *in vitro* biokinetics study with L-CsA, the concentration of the CsA molecule was assessed with HPLC-MS/MS after digestion of the liposomal carrier with Acetonitrile. Thus, this method does not reveal if the CsA molecules are transported across the cell barrier as part of the liposomal carrier or as a free molecular drug. However, this can be assessed with fluorescently labeled liposomes.

5.3.1 Decrease of the FRET intensity after liposome lysis

To gain more insights into cellular interaction with liposomal nanocarriers, a FRET (Fluorescence (or Förster) Resonance Energy Transfer) pair was incorporated into the lipid bilayer of liposomes. FRET occurs if a donor and acceptor fluorophore are in a distance between 1 – 10 nm, and the emission spectrum of the donor overlaps with the excitation spectrum of the acceptor fluorophore [174]. It was thus hypothesized that only intact liposomes would guarantee the prerequisites for a FRET to occur.

To confirm the functionality of the FRET liposomes, the FRET signals prior and after the disintegration of the liposomes with 0.2% Triton-X100 were investigated. After nebulization of FRET liposomes into the growth medium, the medium was diluted with Triton-X100. A 1.2-fold dilution of the cell culture medium with Triton-X100 showed a statistically significant loss in FRET fluorescence intensity (excitation/emission wavelength: 505 nm/705 nm) by a factor of 4 (figure 5.13A). Furthermore, a 5-fold and 10-fold dilution with Triton-X100 led to further reduction of the FRET signal (< 7%). This confirms that only intact liposomes have a strong FRET signal, which is the prerequisite for monitoring the structural integrity of FRET liposomes. DLS measurements revealed a volume-weighted mean diameter of 130 nm (figure 5.13B). Further, they revealed a polydispersity index (PDI) of 0.119 before the nebulization and a PDI of 0.283 after the nebulization, respectively (data not shown). The PDI is a direct measure for the distribution of the liposomes and should be below 0.3 for aerosolized delivery of liposomes [175] [176]. Taking into account the results obtained by Schmid et al. (2017)[68], we interpret the slight increase as deformation of the liposomes during the aerosolization process. Finally, DLS measurements in the basal medium showed no intact liposomes after aerosolization of FRET liposomes on A549-Luc(IL-8) cells, indicating a loss of liposomal integrity after cellular interactions (figure 5.13C).

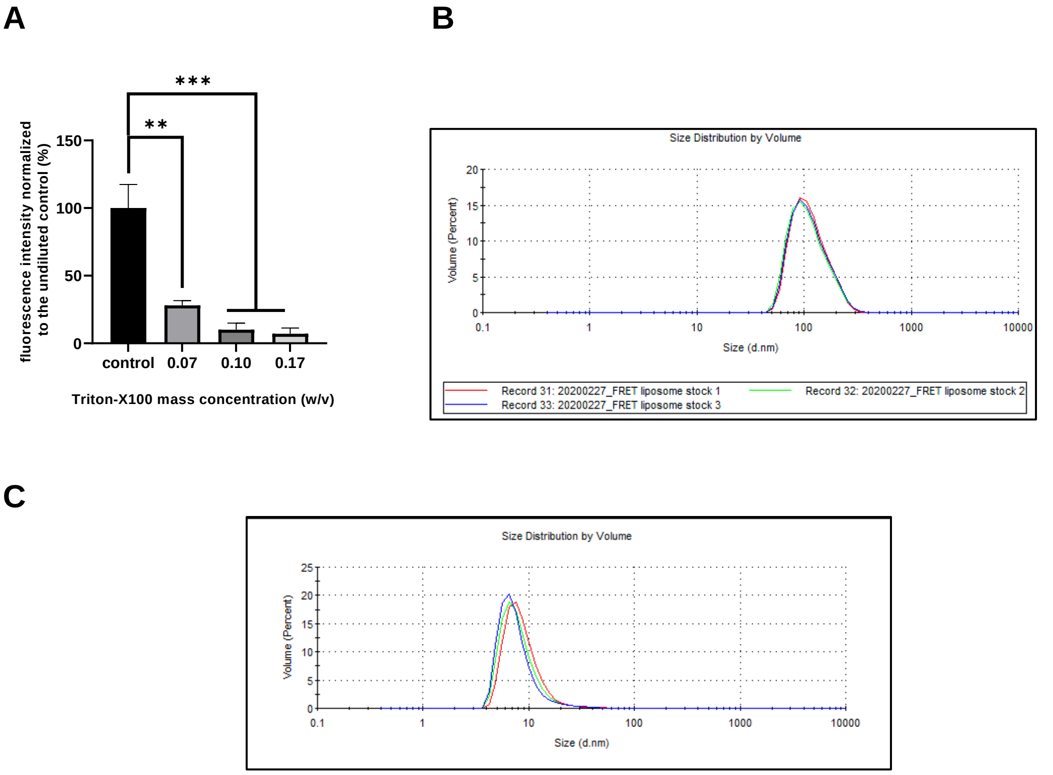

Figure 5.13: Characterization of FRET liposomes with respect to particle size and functionality. **Panel A:** Increasing lysis of FRET liposomes in suspension with increasing Triton-X100 confirmed the functionality of FRET liposomes, i.e., only intact liposomes provide a strong fluorescent signal (ex/em = 505 nm/705 nm; DiI and DiD dye) **Panel B:** A volume-weighted mean particle diameter of 130 nm was obtained. **Panel C:** The absence of particle sizes > 100 nm after nebulization of FRET liposomes on A549-Luc(IL-8) cells indicates a loss of liposomal integrity after cellular interactions. Data are presented as mean ± SEM (n = 3 independent experiments). ** $p \leq 0.01$, *** $p \leq 0.001$

5.3.2 Weak transcellular transport of intact liposomes at ALI conditions

The degree of transbarrier transport of FRET liposomes was investigated after nebulization. For this, the FRET liposomes were aerosolized on A549-Luc(IL-8) cells on Transwell® inserts at ALI conditions ($V_{\text{aerosolized}}$ = 50 µL, cell-delivered dose = 2.8 µg/cm^2) and transbarrier transport was assessed by monitoring the FRET signal in the separate compartments (cell-associated, basal) for 24 h. A membrane-only control (no cells) was included to evaluate the effects of the Transwell® insert membrane on the transport.

While the cell-free Transwell® insert transmitted 100% of the deposited liposomes into the basal medium, only ca. 23% of intact liposomes reached the basal medium in the presence of cells, but this within 1 h (fig. 5.14A). This is in disagreement with the DLS measurements (figure 5.13C), which showed no intact liposomes in the basal compartment after cell exposure and will be discussed later in the discussion. The fraction of intact liposomes in the cell compartment (after washing off of the liposomes attached apically to the cells) decreased from 49% to 20% within 7 h, while a similar trend, but on a much lower dose level, was observed for the membrane-only case (reduction from 14% to 5% within 7 h of the liposome fraction tightly attached to the membrane) (figure 5.14B). On the apical side (not tightly attached to the cells or membrane), the initially observed liposome fraction of 44% decreased within 2 h to 9% and even to 3% within 24 h in the presence of cells, while no statistically significant signal could be observed in the absence of cells (figure 5.14C, red line). It is important to note that the data presented in panel A-C (figure 5.14) are normalized to the sum of the fluorescence intensity (at the first time point; 7 min after nebulization) in all compartments (basal, apical, cells/membrane) of the ALI cell culture. Hence, these data represent relative distributions, which add up to 100% for each time point; assessment of the fraction of intact liposomes relative to the delivered dose is not possible from these values but will be addressed in figure 5.15. The relatively high cell-association of intact FRET liposomes reported in panels B and C of figure 5.14 was confirmed with fluorescence microscopy (figure 5.14D), where the yellow areas indicate co-localization of the fluorescent dye DiI (red) with the actin cytoskeleton (green).

Taken together, figure 5.14 reveals that intact liposomes were predominantly associated with A549-Luc(IL-8) cells and did not penetrate much (ca. 20% relative to time-dependent dose of intact liposomes; see figure 5.15) across the cell barrier into the basal medium even after 24 h.

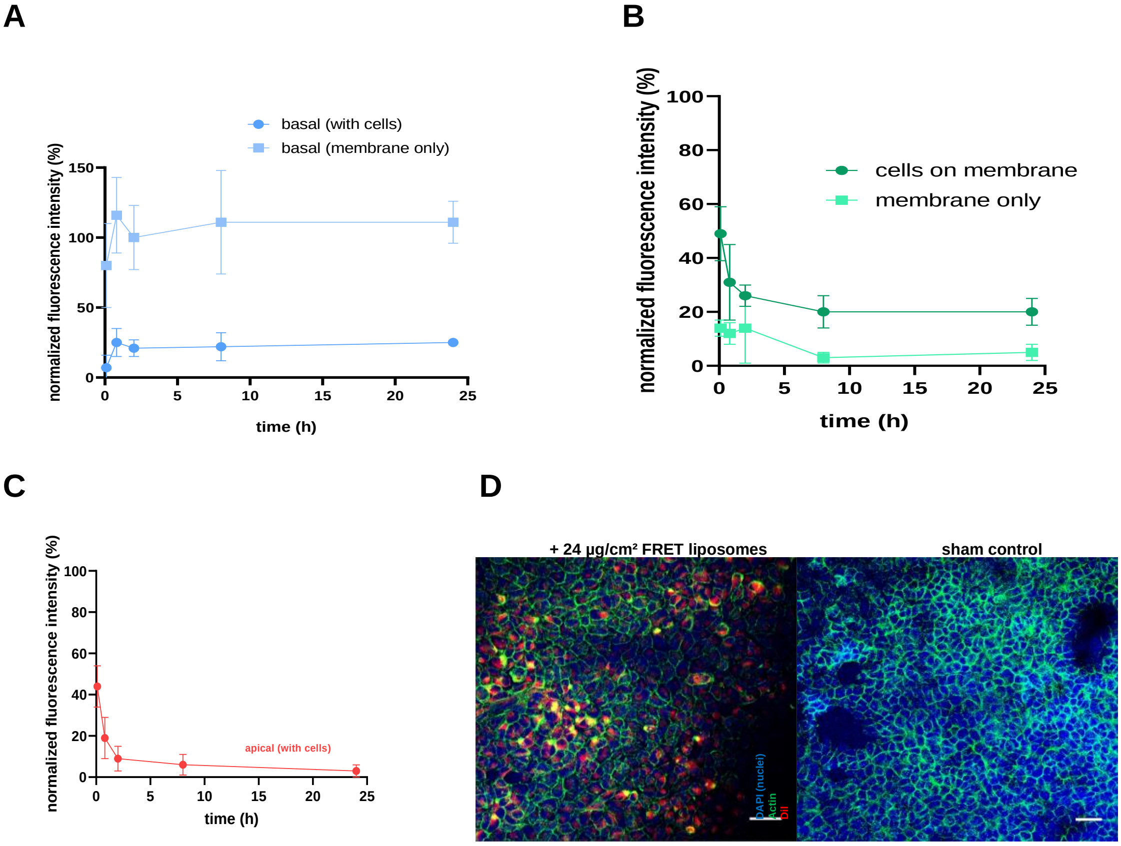

Figure 5.14: Relative fraction of intact nebulized FRET liposomes in the different compartments of the ALI cell culture model (apical, cell/membrane, basal) consisting of a confluent layer of A549-Luc(IL-8) cells. **Panel A:** While 100% of the liposomes are transferred as intact liposomes across the membrane of the Transwell® insert only (no cells), only 23% of intact liposomes reached the basal compartment in the presence of cells. **Panel B:** Correspondingly, the fraction of intact liposomes in the cell compartment was reduced from 49% to 20% within 7 h, while this fraction of tightly membrane-attached liposomes reduced from 20% to 5% within 7 h in the absence of cells (membrane-only). **Panel C**: The fraction of cell-associated FRET liposomes decreased from 44% at 7 min after delivery to zero at 24 h. No apical fluorescence was detected for the membrane-only control (data not shown). **Panel D**: Relatively uniform distribution of cell-associated intact FRET liposomes (red) overlaid with F-actin (green) and cell nuclei (blue) (scale bar: 10 µm). Data (A-C) are normalized to the total fluorescence intensity observed at the first observed time point (7 min) in all compartments (basal, apical, cells/membrane) of the Transwell® insert and presented as mean ± SEM (n = 3 independent experiments).

To determine the degree of liposome degradation after deposition on the cells, the loss of total fluorescence intensity from all compartments was analyzed over time. A significant reduction in total fluorescence intensity from 100% to 74% was measured for 48 min (0.8 h) after the nebulization (figure 5.15A). This value decreased further until it reached an asymptotical value of 48% at 8 h. No loss of fluorescence intensity was observed for the membrane-only control, which was almost entirely dominated by the basal compartment (figure 5.15B). This indicates that liposomes are stable in the cell culture medium. Thus, the reduced fluorescence intensity in panel A has to be due to the degradation of liposomes being in contact with cells. It is likely that the strong decrease of fluorescence signal in the apical compartment is not solely due to liposome degradation, but also due to transport into and through the cell compartment (into the basal medium).

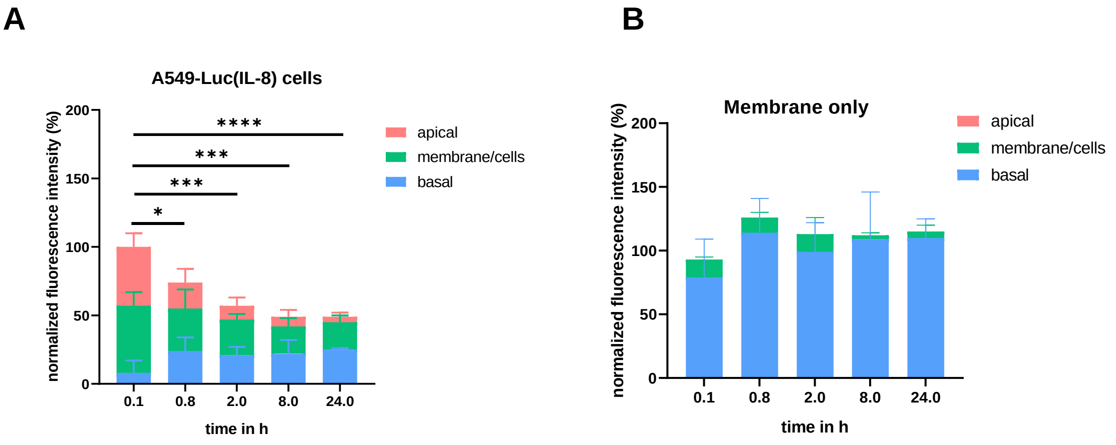

Figure 5.15: Fluorescence intensity over time after nebulization of FRET liposomes onto A549-Luc(IL-8) cells. **Panel A:** The total intensity significantly dropped from the initial value (set to 100%; measured at 7 min) to 48% within the 24 h-monitoring periods for cell-covered Transwell® inserts. **Panel B:** In contrast, no statistically significant dynamics in fluorescence intensity was observed for the membrane-only setup. Data represent mean ± SEM (n = 3 independent experiments). * $p \leq 0.05$, ** $p \leq 0.01$, *** $p \leq 0.001$, **** $p \leq 0.0001$

5.3.3 Cellular uptake of FRET liposomes by caveolae-mediated endocytosis

To further analyze cellular uptake of FRET liposomes, various possible cellular uptake pathways were blocked with specific inhibitors, namely pinocytosis (Amiloride), clathrin-mediated endocytosis (Pitstop-2) and caveolae-mediated endocytosis (Filipin). After a 10 min inhibition period, A549-Luc(IL-8) cells at the ALI were exposed to aerosolized FRET liposomes. At different time points after liposome nebulization, the intact liposome fraction in the apical compartment of the Transwell® insert setup was measured by washing the apical compartment three-times with 500 µL 0.9% NaCl, and then analyzing the wash-out for FRET fluorescence. The FRET fluorescence was thereafter normalized to the total FRET fluorescence measured in all three compartments at the first sampling time (7 min, i.e., 0.1 h).

In general, there was no significant difference in FRET fluorescence for control (no inhibitor) and inhibited cells (figure 5.16) except for the 0.8 h time point, where Filipin inhibited cellular uptake, indicating that caveolae-mediated endocytosis is the dominant active cellular uptake mechanism of FRET liposomes. The statistically significant increase in fluorescence (FRET) signal for Amiloride after 24 h is considered an outlier since it is unlikely that intact FRET liposomes will migrate back from the basal to the apical side only for one of the applied inhibitors, especially if we take into account that FRET liposome transport without inhibitors was completed after 2 hours (see figure 5.14C).

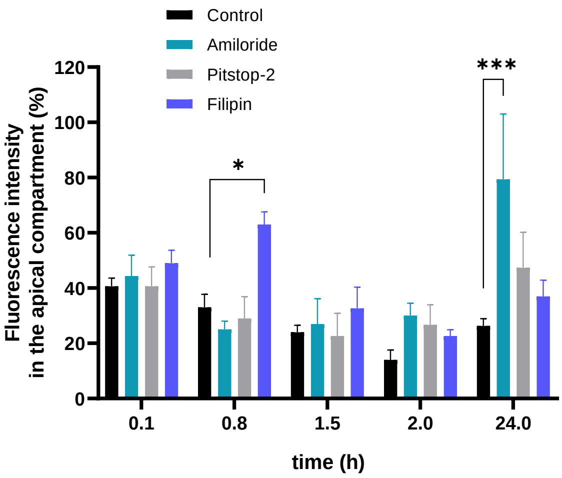

Figure 5.16: Investigation of cellular (A549) uptake mechanisms of aerosolized liposomes measured by FRET fluorescence intensity in the apical compartment after application of various cellular uptake inhibitors. Only Filipin showed significant inhibition after 0.8 h compared to control, indicating that caveolae-mediated endocytosis was involved in cellular uptake of FRET liposomes. Data are normalized to the initial fluorescence intensity after 7 min in all compartments of the Transwell® insert and presented as mean ± SEM (n = 3 independent experiments). * $p \leq 0.05$, *** $p \leq 0.001$ (tested against control (black bars))

Further insight into the temporal profile of cellular (FRET) liposome uptake was obtained with live cell imaging, which focused on the apical side of the cell layer. For control conditions (no inhibitor), the maximum uptake of FRET liposomes was detected after 12 min as indicated by the reduced intensity and patchy profile of the FRET signal (figure 5.17A) due to partial cellular uptake of the liposomes. These features were not observed to the same degree after application of Filipin (figure 5.16B) confirming again the involvement of caveolae-mediated endocytosis as an uptake pathway of FRET liposomes. Moreover, the appearance of micron-sized fluorescence hotspots can be interpreted as evidence for gradual agglomeration of the FRET liposomes on the apical side of the membrane.

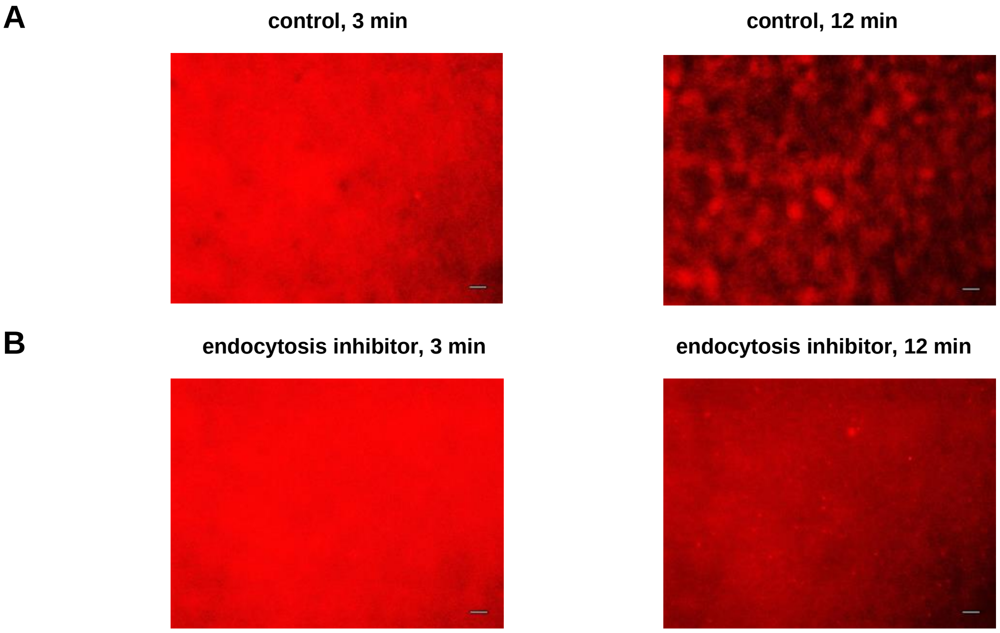

Figure 5.17: Cellular (A549) uptake of aerosolized FRET liposomes monitored with live-cell imaging (red signal). **Panel A:** For the absence of any uptake inhibitor (control), substantial cellular uptake of liposomes was evident at 12 min from the reduced and patchy FRET intensity as compared to the 3 min image. **Panel B:** After inhibition of caveolae-mediated endocytosis (Filipin), a spatially more uniform FRET signal is found at 12 min and the appearance of “hot spots” is evidence for gradual agglomeration of the liposomes on the apical side of the cells. Scale bar: 10 µm

5.4 Biokinetics of Paclitaxel loaded polymeric nanocarriers (“Ptx-NP”)

In addition to L-CsA, we also investigated the biokinetics of another inhaled nanodrug, Paclitaxel-loaded nanocarriers (Ptx-NP). Ptx-NP are currently in pre-clinical development to treat pulmonary arterial hypertension. Since endothelial cells are among the main target cells of Ptx-NP, the *in vitro* model of the air-blood barrier consisting of A549-Luc(IL-8) cells as epithelium was extended with an endothelial cell line (EA.hy926) co-cultured on the basal side of the Transwell® insert setup.

Two different formulations were tested:

- a fast-releasing Ptx-NP formulation (Ptx-NPF)
- a slow-releasing Ptx-NP formulation (Ptx-NPS)

5.4.1 Evaluation of dose-controllable delivery of Ptx

Analogous to the L-CsA study, dose-controlled aerosolized delivery of Ptx-NP was performed with the VITROCELL® Cloud 6, which is equipped with an Aeroneb Pro® vibrating mesh nebulizer and a quartz crystal microbalance (QCM) for real-time measurement of the cell-delivered Ptx-NP dose.

In a first step, the QCM was evaluated for its capacity to allow the prediction of the cell-delivered Ptx dose. This is important, since the QCM measures not only Ptx, but also the mass of the NPs used as nanocarrier and soluble formulation compounds (e.g., for pH buffering). Hence, the observed QCM signal was compared to the actual Ptx dose determined by extraction of Ptx from the apical, cell, and basal compartment of ALI A549-Luc(IL-8) cell culture model (table 5.2) and subsequent Ptx dosimetry with HPLC-MS/MS. Here, 500 µL of 4% (w/v) Ptx-NPF suspension was nebulized on two different ALI cell culture models, namely a A549-Luc(IL-8) (epithelial cell line) cells and a coculture consisting of A549-Luc(IL-8) and EA.hy926 cells (endothelial cell line) as well as membrane-only (no cells) as control.

Figure 5.18 shows an exemplary real-time deposition result of the QCM after nebulization of 4% (w/v) fast-releasing Ptx-NPF. It is important to mention that the wells of the aerosolization system are filled with 13.5 mL PBS and that the system was preheated to 37°C before nebulization to ensure a sufficient deposition efficiency [93]. Thus, the QCM signal monitors Ptx-NPF deposition but is overlaid by humidity artefacts in the system (figure 5.18, before 12 min). The removal of the lid after 12 min leads to drying of the QCM and a correct measure of Ptx-NPF deposition.

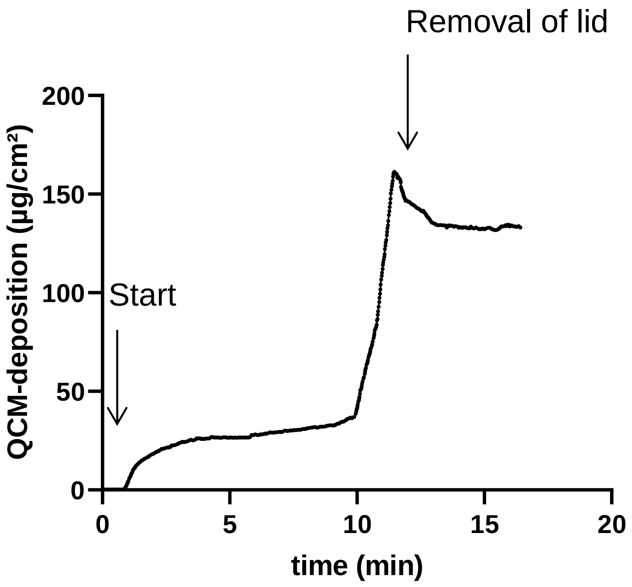

:

Figure 5.18: Real-time monitoring of fast releasing Ptx-NPF deposition onto the quartz crystal microbalance (QCM) of the VITROCELL® Cloud 6 system. After aerosolization of 500 µL 4% (w/v) fast-releasing Ptx-NPF solution, a deposition of 133 µg/cm² (NP plus Ptx loading) on the QCM could be achieved. Thus, the cell-delivered dose can be assessed in real-time with the QCM. “Start” indicates start of nebulization. Only after removal of the lid of the exposure chamber, the deposited Ptx-NP droplets dry, allowing the QCM to accurately measure the deposited Ptx-NP mass.

From the QCM signal, which represents the mass from both the NPs and the Ptx, the Ptx dose can be calculated from the experimentally determined Ptx loading efficiency (measured routinely during Ptx-NP production phase), which was 4.3%. Hence, the Ptx mass dose (D_{Ptx}) can be calculated from the QCM signal (D_{QCM}) according to

$$D_{Ptx} = Load_{Ptx} \cdot D_{QCM} \qquad (5\text{-}2)$$

where $Load_{Ptx}$ is the Ptx loading efficiency of the nanocarriers (here 4.3%).

It is evident from table 5.2 that the QCM-derived Ptx dose is by a factor of 1.44 (± 11%, SD) larger than the analytically determined dose in the Transwell® inserts (where the cells are located). This could be interpreted as a lower effective loading efficiency (3.0% = 4.3%/1.44), which might occur due to artefacts introduced during storage and/or transport of the formulation (from our partner Giessen to Munich). However, this could also be due to differences in drug deposition onto the QCM and the Transwell® inserts (where the cells are located). In any case, the relatively constant ratio of QCM and Ptx dose in the inserts (11% SD) allows for accurate real-time prediction of the cell-delivered Ptx dose after nebulization of the Ptx-NP formulation.

In conclusion, the QCM of the VITROCELL® Cloud 6 technology could be used to determine the amount of drug per Transwell® insert and to allow for dose-controlled delivery of Ptx as Ptx-NP to the cells.

Table 5.2: The Ptx dose calculated from the QCM data was 44 ± 6% larger than the Ptx dose in the Transwell® inserts (on the cells) as determined by HPLC-MS/MS. Since the positive bias of the QCM prediction is 44% (± 11% SD relative to 44%), the QCM data can serve as real-time dose monitor with an accuracy of 13%. Data are expressed as mean ± SEM (n = 3)

Exposed Cells	**Measured deposition of the fast-releasing Ptx-NP formulation by the QCM (µg/cm²)**	**Calculated Ptx-deposition (loading efficiency = 4.3%) (µg/cm²)[a]**	**Measured Ptx-mass in insert via HPLC-MS/MS (µg/cm²)[b]**
A549-Luc(IL-8)-Luc(IL-8)	105 ± 4	4.52 ± 0.18	3.19 ± 0.52
Coculture (A549-Luc(IL-8) /EA.hy926)	121 ± 23	5.20 ± 0.89	3.86 ± 0.41
Membrane-only (no cells)	132 ± 21	5.68 ± 0.81	3.67 ± 0.60

a. The Ptx dose on the QCM was calculated from a drug loading efficiency of 4.3% measured by our colleagues who manufactured the Ptx-NP formulation.

b. The Ptx dose was assessed by HPLC-MS/MS for every compartment of the Transwell® insert setup (basal, cells, apical) and then summed up for comparison with the QCM-measured dose

5.4.2 Effects of Ptx-NP on viability and barrier integrity of the model of the air-blood barrier

To ensure meaningful results from the Ptx-NP biokinetics studies, the absence of cellular toxicity and reduced barrier integrity is essential. Hence, these parameters were analyzed before performing biokinetics studies. 100 µL, 300 µL, and 500 µL of a 4% (w/v) Ptx-NP stock solution (slow and fast-releasing) in deionized water were nebulized, and the deposition was assessed by the QCM. The cell-delivered doses were calculated in µg Ptx/cm² from the measured QCM mass dose and the Ptx loading of Ptx-NP ((4.8 ± 0.6)% (w/w)) according to equation 5-2. Aerosolized Ptx-NP (fast and slow-releasing) did not lead to adverse effects on barrier integrity, pro-inflammatory response, and cytotoxicity 24 h after exposure (figure 5.19B-E and figure 5.20B-D). Furthermore, Actin staining of the cytoskeleton confirmed the integrity of A549-Luc(IL-8) cells after exposure to Ptx-NP (figure 5.17F). On the other hand, cell viability was somewhat reduced to about 50% for 6.4 µg Ptx/cm² (both formulations) (figure 5.19A, figure 5.20A) and for 3.8 µg Ptx/cm^2 (slow-releasing only) (figure 5.20A).

Comparable TEER values were found for the mono- and coculture (figure 5.19D), and Ptx-NP exposure did not change the barrier integrity of the cells.

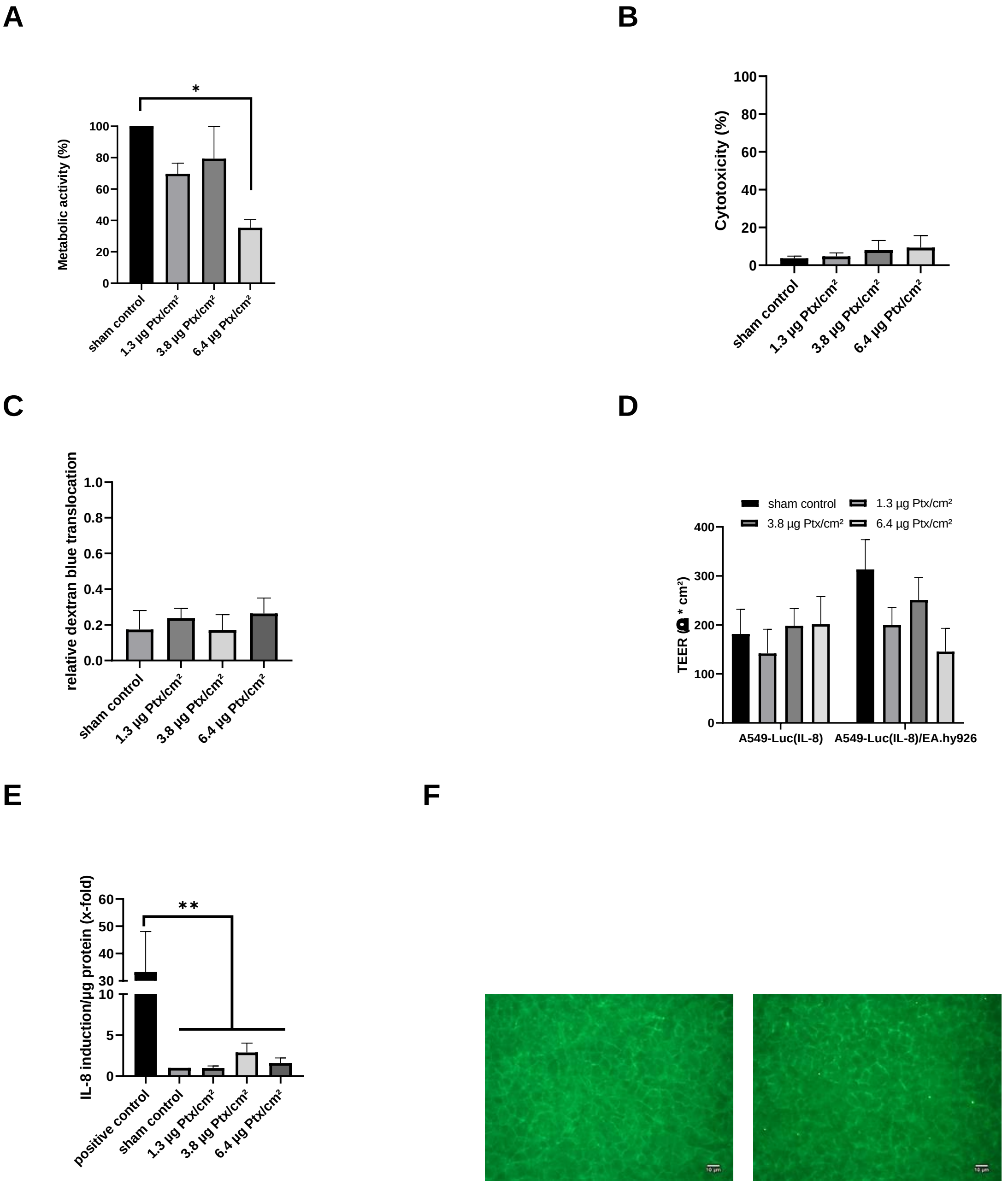

Figure 5.19: Effects of the fast-releasing Ptx-NPF formulation on cellular parameters (24 h postexposure). **Panel A**: No loss in metabolic activity (viability) of A549-Luc(IL-8) epithelial cells in a coculture with EA.hy926 endothelial cells was seen, except for the highest dose of 6.4 µg Ptx/cm² as compared to the sham control (vehicle). **Panel B:** The LDH assay showed non-significant cytotoxic effects of the coculture model for any of the tested doses. **Panel C, D**: The dextran blue assay of the coculture model and TEER measurements indicated that Ptx-NP did not negatively affect the integrity of the cell barrier. **Panel E**: Ptx-NPF did not induce pro-inflammatory response (IL-8 induction) of A549-Luc(IL-8) cells in a coculture with EA.hy926 cells as compared to the sham control (TNF-α stimulation was used as positive control). **Panel F**: Actin staining (green) of the cytoskeleton of A549-Luc(IL-8) cells confirmed confluence of the cell layer, typical morphology of A549-Luc(IL-8) cells, and integrity of the barrier model. Scale bar: 10 µm. For the sham control of panel A, an outlier was removed from further statistical testing. Data are presented as mean ± SEM (n = 3 independent experiments). * $p \leq 0.05$, ** $p \leq 0.01$

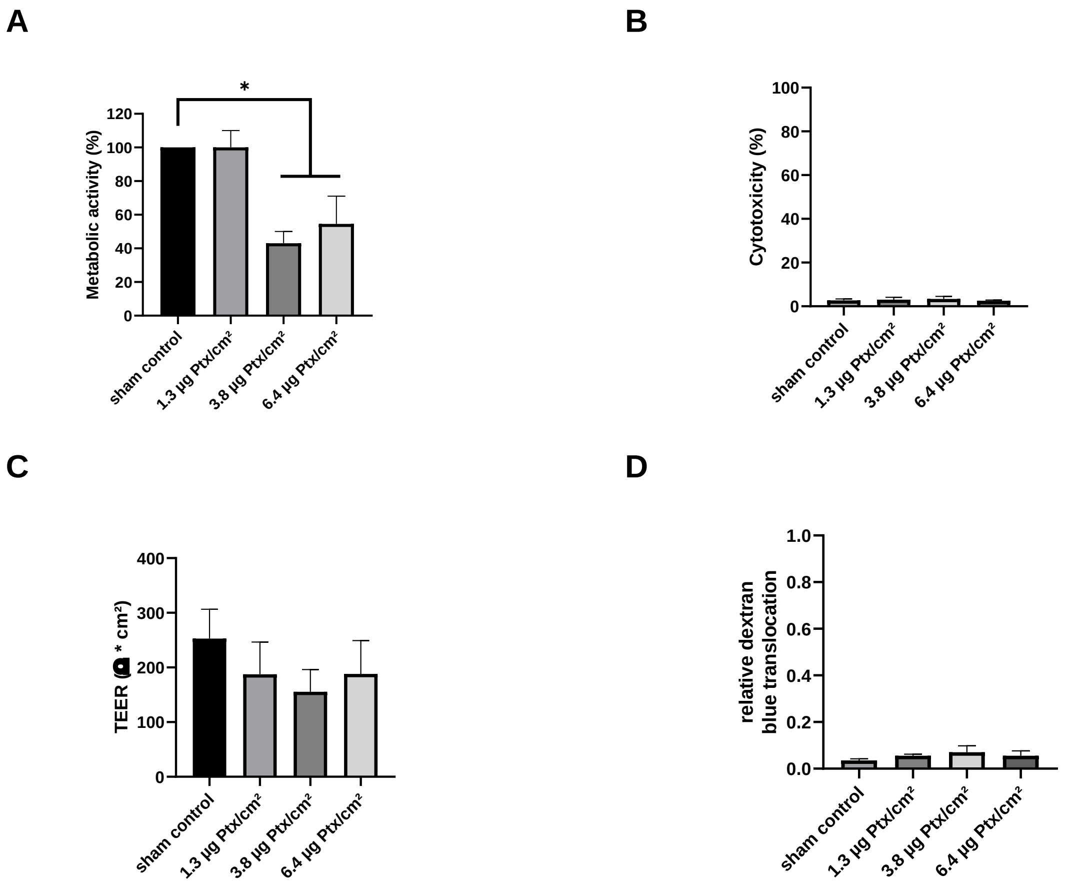

Figure 5.20: Effects of the slow-releasing Ptx-NPS formulation on cellular parameters after 24 h. **Panel A:** A significant decrease in metabolic activity (viability) of A549-Luc(IL-8) cells in a coculture with EA.hy926 cells to about 50% was observed for 3.8 µg/cm^2 and 6.4 µg/cm^2. **Panel B:** Non-significant effects on the cytotoxicity could be revealed. **Panel C, D:** TEER measurements and dextran blue assay confirm the intact barrier integrity of the coculture model even for the highest dose. Data are expressed as mean ± SEM (n = 3 independent experiments). * $p \leq 0.05$

The experiments with placebo Ptx-NP (slow-releasing) indicated that the reduced metabolic activity after 24 h could be attributed to the nanoparticles, not to the paclitaxel loading (figure 5.21). In the placebo experiments, similar doses as compared to the verum exposure were used (presented as Ptx$_{eq}$, eq = equivalent).

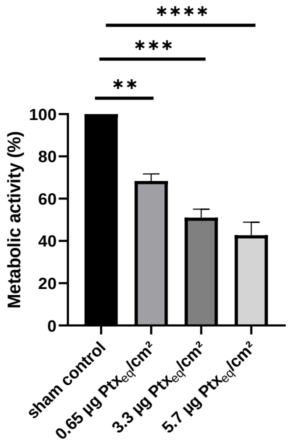

Figure 5.21: Effect of placebo slow-releasing Ptx-NPS on the metabolic activity of A549-Luc(IL-8) cells. A significant decrease in metabolic activity (cell viability) could be observed after 24 h. Hence, the observed loss in viability for Ptx-loaded NP is due to the polymeric nanocarrier (for the highest two doses; see figure 5.20 A). Data are expressed as mean ± SEM (n = 3 independent experiments). * $p \leq 0.05$, ** $p \leq 0.01$, *** $p \leq 0.001$, **** $p \leq 0.0001$

Since the barrier integrity was not impaired, but high doses are expected to be needed for efficacy studies, the Ptx-NP biokinetics studies were performed for the highest dose level (ca. 6.4 µg Ptx/cm^2). On the other hand, for this dose, reduced metabolic activity was found after 24 h, which might affect cellular uptake and/or transcellular transport. However, most of the NP-Ptx transport occurs during the first 2 h after exposure (see below), which did not show any reduction in cell viability (figure 5.22). Thus, 6.4 µg Ptx/cm^2 was considered a suitable dose level for both biokinetics and efficacy studies.

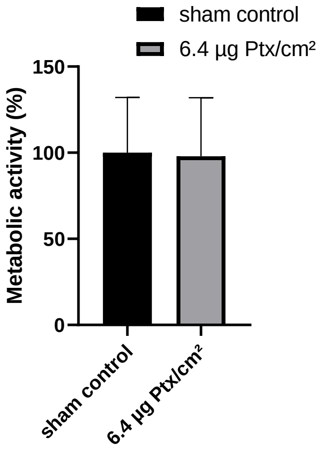

Figure 5.22: Effect of slow-releasing Ptx-NPS on the metabolic activity of A549-Luc(IL-8) cells after 2 h. There was no reduction in metabolic activity. Data are expressed as mean ± SEM (n = 3 independent experiments)

5.4.3 Transbarrier transport of Ptx-NP for the mono- and coculture model of the air-blood barrier

Similar to the L-CsA biokinetics study, Ptx-NPF and Ptx-NPS were nebulized on two *in vitro* models of the air-blood barrier. The influence of the Transwell® insert membrane on the biokinetics was accounted for as described in the methods (equation 1-3). The doses were normalized to the cell-delivered Ptx dose per Transwell® insert (100% = (21 ± 2) µg Ptx), but ca. 15% of this dose was already transported to the basal medium in the VITROCELL® Cloud system, i.e., prior to starting the biokinetics study in a separate multiwall plate.

The biokinetics of both Ptx-NP formulations revealed a burst-like increase for both cell models (figure 5.21), which means that steep initial transport rates into the basal compartment were obtained 4 h after aerosolization. Then, the transport was flattening as almost all of the available Ptx has been transported into the basal compartment.

No significant difference in the translocation profile was observed for both cell models (epithelial A549-Luc(IL-8) and coculture model (A549-Luc(IL-8) and endothelial EA.hy926 cells) for both Ptx-NP formulations, except for slow-releasing Ptx-NPS under monoculture conditions (figure 5.23C), which showed a ca. 2-fold reduced transbarrier transport (ca. 30%, blue line) and corresponding higher Ptx storage in the cell-apical compartment of ca. 70% as compared to ca. 30% for all other cases (figure 5.23A, B & D, green line).

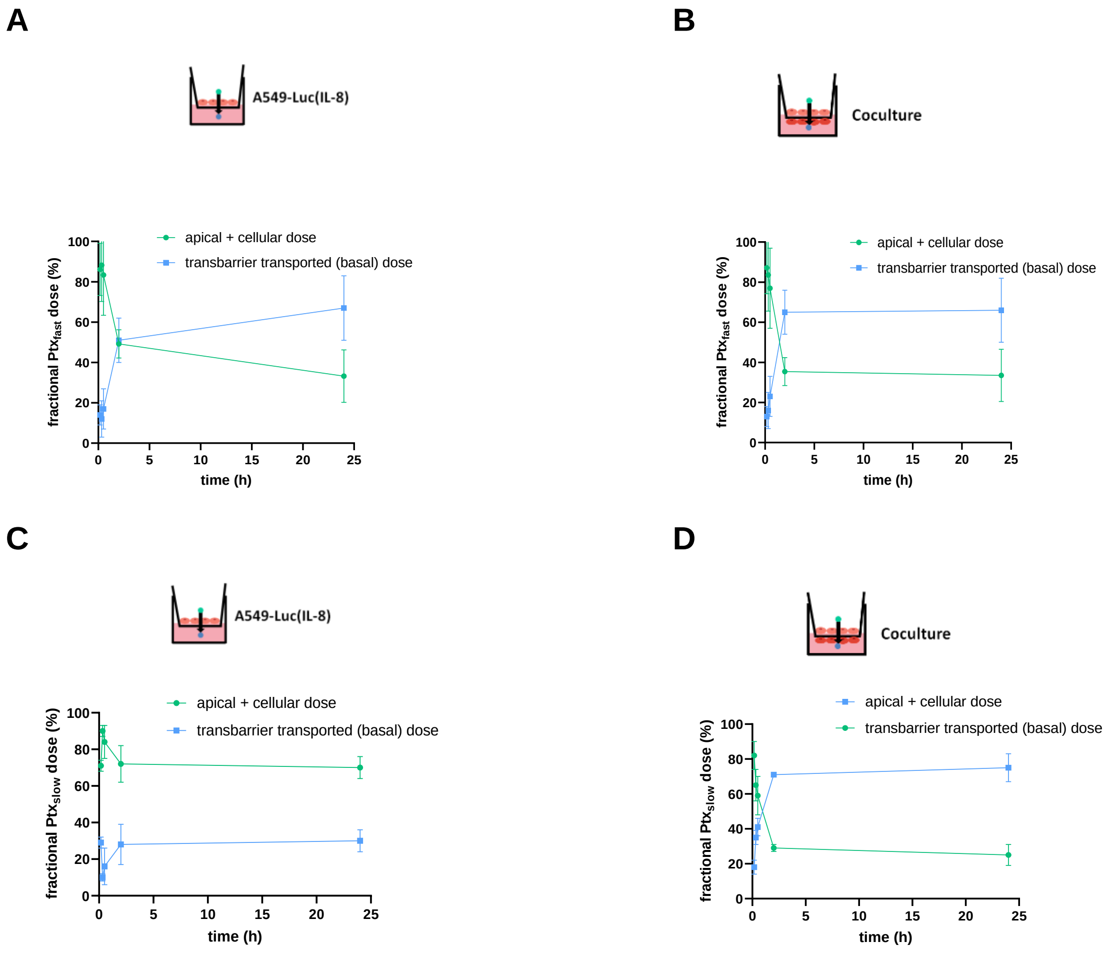

Figure 5.23: Biokinetics of two different aerosolized Ptx-NP formulations in two cell culture models expressed as the temporal profile of the Ptx dose in the cell plus apical compartment and the basal compartment (transbarrier transport). **Panel A, B:** For the fast-releasing Ptx-NPF, 65% of the Ptx dose is transported across the barrier within 2 h without significant dependence on the type of cell culture. **Panel C:** For the slow-releasing Ptx-NPS in the monoculture model, the transbarrier transport was about 2-fold reduced (to ca. 30%) as compared to Ptx-NPF (panels A and B). **Panel D:** The same biokinetics profile as in panels A & B (for Ptx-NPF) was observed for the slow-releasing Ptx-NPS in the coculture model. Data are normalized to the delivered Ptx dose per Transwell® insert ((21 ± 2) µg) and expressed as mean ± SEM (n = 3 independent experiments).

As demonstrated by this biokinetics study, the addition of an endothelial cell line on the basal side of the Transwell® insert did not increase the barrier tightness of the cell culture model with respect to Ptx-NP (figure 5.23). This was further investigated by analysis of dextran blue translocation as a paracellular transport marker, which was routinely measured for each of the Ptx-NP exposures prior to Ptx-NP application. The presence of endothelial cells (EA.hy926) increased paracellular transport moderately from (1.7 ± 0.2)% to (5.4 ± 0.5)% (figure 5.24).

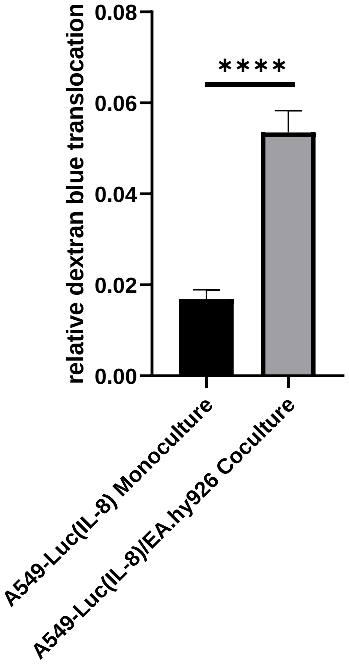

Figure 5.24: Investigation of the dependence of paracellular transport on mono- (A549) and coculture cell culture model (A549 & EA.hy926) based on dextran blue transport into the basal compartment (within 2h). The presence of endothelial cells (EA.hy926) increases paracellular transport from (1.5 ± 0.2)% to (5.4 ± 0.5)%. Data are expressed as mean ± SEM (n = 12 independent experiments). **** $p \leq 0.0001$

Thus, inclusion of an endothelial cell line (EA.hy926) did not substantially affect the barrier permeability of A549 cells, neither for Ptx-NP (no significant effect) nor for paracellular transport (moderate decrease).

In conclusion, burst-like transport profiles of both types of Ptx-NP formulations (fast and slow release) were observed reaching an asymptotic transport value of ca. 70% (30% retained by cells) without significant difference between the monoculture and coculture model, except for the low transport of Ptx-NP (only 30% transport across cell barrier).

5.4.4 Extension to the coculture model leads to enhanced storage of Ptx

The assessment of the biokinetics revealed the storage of Ptx in the apical and cell compartment even after 24 h. For a more in-depth analysis of the Ptx fraction, which was taken up by the cells, the loosely attached Ptx fraction (apical) was removed via several washing and freeze-thaw cycles as described in the method section. The membrane attached Ptx fraction was subtracted to account for membrane artefacts. For these experiments, the measured Ptx dose was normalized to the cell-delivered Ptx dose (100% = (21 ± 2) µg).

The experiments showed that the addition of endothelial cells significantly increased the intracellular Ptx storage after Ptx-NP exposure for every investigated time point (figure 5.25A,B, grey bars). In addition, slow-releasing Ptx-NPS showed superiority in terms of intracellular drug accumulation as Ptx was present for every investigated time point and as the stored fraction after 24 h was 1.7-fold increased. Overall, the results indicate that endothelial cells led to additional Ptx transport, which increased the cellular Ptx storage.

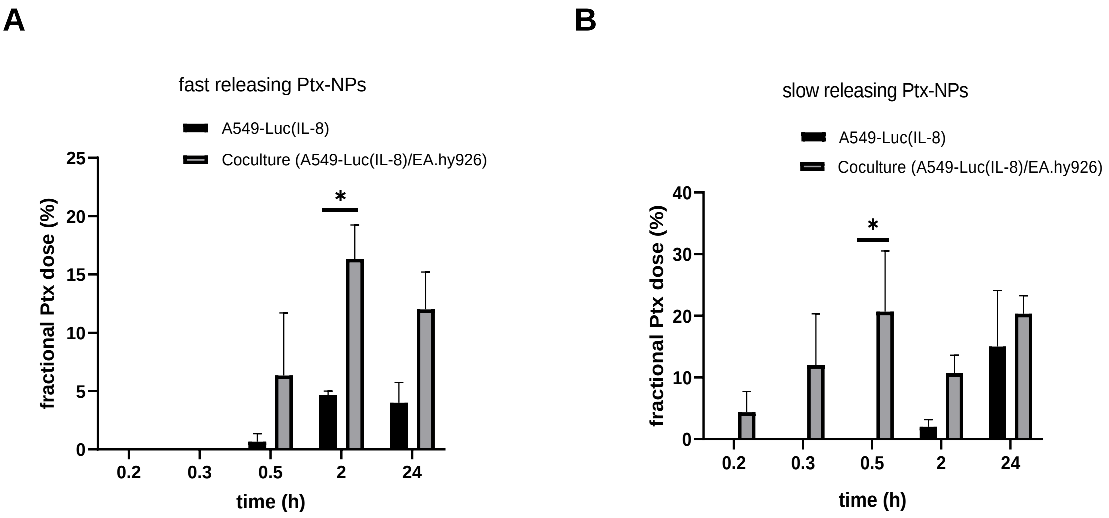

Figure 5.25: Storage of Ptx in the cell-compartment of the coculture model after the nebulization of fast- and slow-releasing Ptx-NP formulations. The cellular Ptx dose is larger for the coculture model, especially for the intermediate time points (0.5 and 2h), where this trend is statistically significant for one of the two formulations each. The onset of Ptx accumulation in the cells started earlier for slow-releasing Ptx-NPS. The cell-retained Ptx fraction was preferentially found in the endothelial cells, which are target cells for the treatment of pulmonary hypertension. Data are normalized to the delivered Ptx dose per Transwell® insert ((21 ± 2) µg) and expressed as mean ± SEM (n = 3 independent experiments). * $p \leq 0.05$

5.4.5 Particle size analysis of Ptx-NP

Further investigation of the biokinetic fate of slow-releasing Ptx-NP in the A549-Luc(IL-8) epithelial barrier model was performed by measurements of the volume-weighted size distribution of aerosolized Ptx-NP by dynamic light scattering (DLS) in the apical and basal compartment. Intact Ptx-NP with a typical diameter of ca. 200 nm were found in the apical compartment for up to 2 h, but not at 24 h anymore (figure 5.26A). In contrast, no intact Ptx-NP of ca. 200 nm were found in the basal compartment (figure 5.26B). The particles with a size of 5 – 8 nm in the basolateral medium is consistent with the presence of fetal calf serum in the cell culture medium (figure 5.26D). In contrast to cell-covered Transwell® insert membranes, the transport across a membrane-only control revealed intact nanocarriers in the basolateral medium (figure 5.26C). Thus, the A549 cell barrier appears to be impermeable by Ptx-NP. On the other hand, Ptx was found in the basolateral medium (figure 5.23 and 5.25), which suggests that Ptx is released from the nanocarriers.

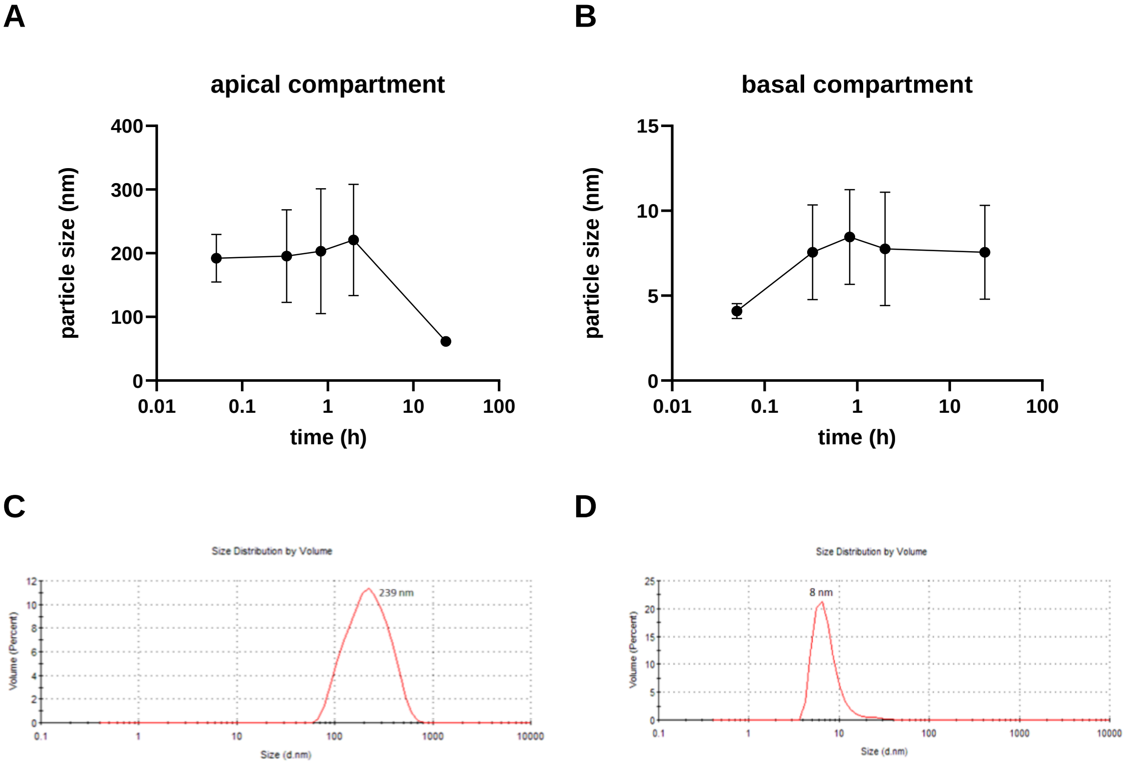

Figure 5.26: Further investigation of slow-releasing Ptx-NPS transbarrier transport by (volume-weighted) DLS size distribution measurements on the apical and basal side of A549-Luc(IL-8) cells. **Panel A:** 200 nm Ptx-NP (DLS size measurement) were found for up to 2 h on the apical side of the cells. **Panel B:** No evidence for 200 nm Ptx-NP was found in the basal compartment. **Panel C:** Transport of intact nanocarriers (NP) into the basal medium (mean diameter: 239 nm) was observed for the membrane-only control (after 24 h). **Panel D:** DLS size measurement of the growth medium (including fetal calf serum) without any NPs revealed the presence of proteins with a typical particle diameter of 8 nm. Data in panels A and B are expressed as mean ± SEM (n = 3 triplicates).

5.4.6 Caveolae-mediated endocytosis as the uptake mechanism of Ptx-NP

It was shown that while nanocarriers themselves were not transported across A549-Luc(IL-8) cells, Ptx molecules were. Hence it is conceivable, that intact nanocarriers were taken up the cells via one of the endocytosis uptake pathways and subsequently Ptx was released from the cells into the basolateral medium. Various cell uptake inhibitors (Filipin, Amiloride, and Pitstop-2) were used to identify such a pathway for fast-releasing Ptx-NPF (35 µg/cm^2; here loaded with Rhodamine dye instead of Ptx), analogues to the FRET liposome cellular uptake study.

For Amiloride and Pitstop-2 treated cells, the decrease of fluorescence intensity in the apical compartment due to uptake and transport into the basal medium did not differ significantly from the control (figure 5.27A, black bars). Consequently, the pathways that were blocked by Amiloride (pinocytosis) and Pitstop-2 (clathrin-mediated endocytosis), respectively, were not involved in the uptake of fast releasing Ptx-NPF. In contrast to this, an increase in the fluorescence was measured for the cells that were inhibited by Filipin (figure 5.27B, blue line). This indicated caveolae-mediated endocytosis as the uptake mechanism of Ptx-NP by A549-Luc(IL-8) cells. In combination with the obtained DLS results, it could be shown that cellular uptake into the cells was facilitated by caveolae-mediated endocytosis of the nanocarriers, but Ptx transport into the blood (here basal medium) required a release of Ptx from the nanocarriers. Hence, the nanocarriers themselves were not transported across the barrier built by A549-Luc(IL-8) cells.

The Filipin experiments were also conducted for the coculture model of the air-blood barrier. Here, no significant differences in comparison to the control were revealed (figure 5.27C). In consideration of the observed higher paracellular transport for dextran blue by the coculture model, this result showed that the addition of the endothelial cell line led to additional transport.

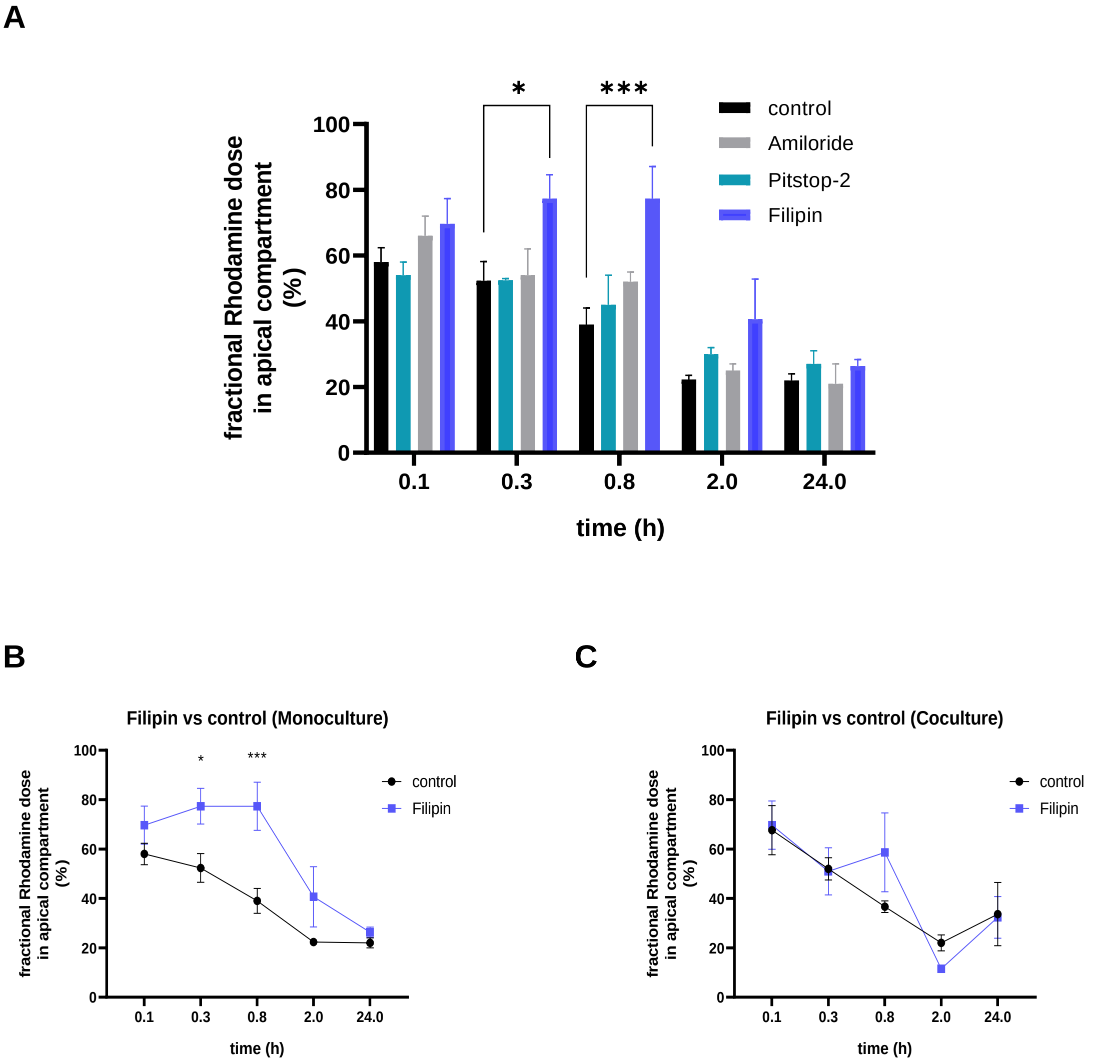

Figure 5.27: Investigation of endocytic cellular uptake mechanisms for fast releasing Ptx-NP. **Panel A, B:** The removal of (fast-releasing) Ptx-NPF (35 µg/cm²; Rhodamine loaded) from the apical side of A549-Luc(IL-8) cells showed the cellular uptake kinetics. Similar to Figure 5.21, the asymptotic dose of ca. 20% was achieved within 2 h after exposure. Inhibition of various types of endocytic uptake with specific inhibitors revealed that caveolae-mediated endocytosis, which is blocked by Filipin, governed the cellular uptake of Ptx-NP. **Panel C:** The epithelial-endothelial coculture model displayed no effect of Filipin on removal of Ptx-NPF from the apical compartment indicating that additional transport routes by endothelial cells were involved. Data in panels B and C are normalized to the initial rhodamine fluorescence in all compartments (basal, apical, cells/membrane) and expressed as mean ± SEM (n = 3 independent experiments). * $p \leq 0.05$, ** $p \leq 0.01$, *** $p \leq 0.001$ (tested against control, black bars)

5.4.7 Efficacy of Ptx-NP

As Ptx-NP are currently in preclinical development as therapeutic option against pulmonary arterial hypertension (PAH), their effect on PAH-relevant genes (FOXO1A, FOXO3A, GADD45, and SOD2) was investigated. As the EA.hy926 cell line expresses these genes, this cell line served as target to investigate the efficacy. Shortly, slow-releasing Ptx-NP were aerosolized at not to low toxicity doses (1.4 – 6.4 Ptx/cm^2; see figure 5.20) onto the coculture model of A549-Luc(IL-8)/EA.hy926 cells. The RNA of EA.hy926 cells on the basal side of the Transwell® insert was isolated and analyzed by qPCR for mRNA regulation as compared to sham control.

qPCR analysis revealed that FOXO1 and FOXO3 expression were upregulated in a dose-dependent manner (figure 5.28A,B). Furthermore, a ca. two-fold increase of the GADD45 gene could be noted even for the lowest dose (figure 5.28C) and SOD2 was upregulated in a dose-dependent manner reaching a ca. two-fold upregulation for the highest dose of 6.4 µg Ptx/cm^2 (figure 5.28D).

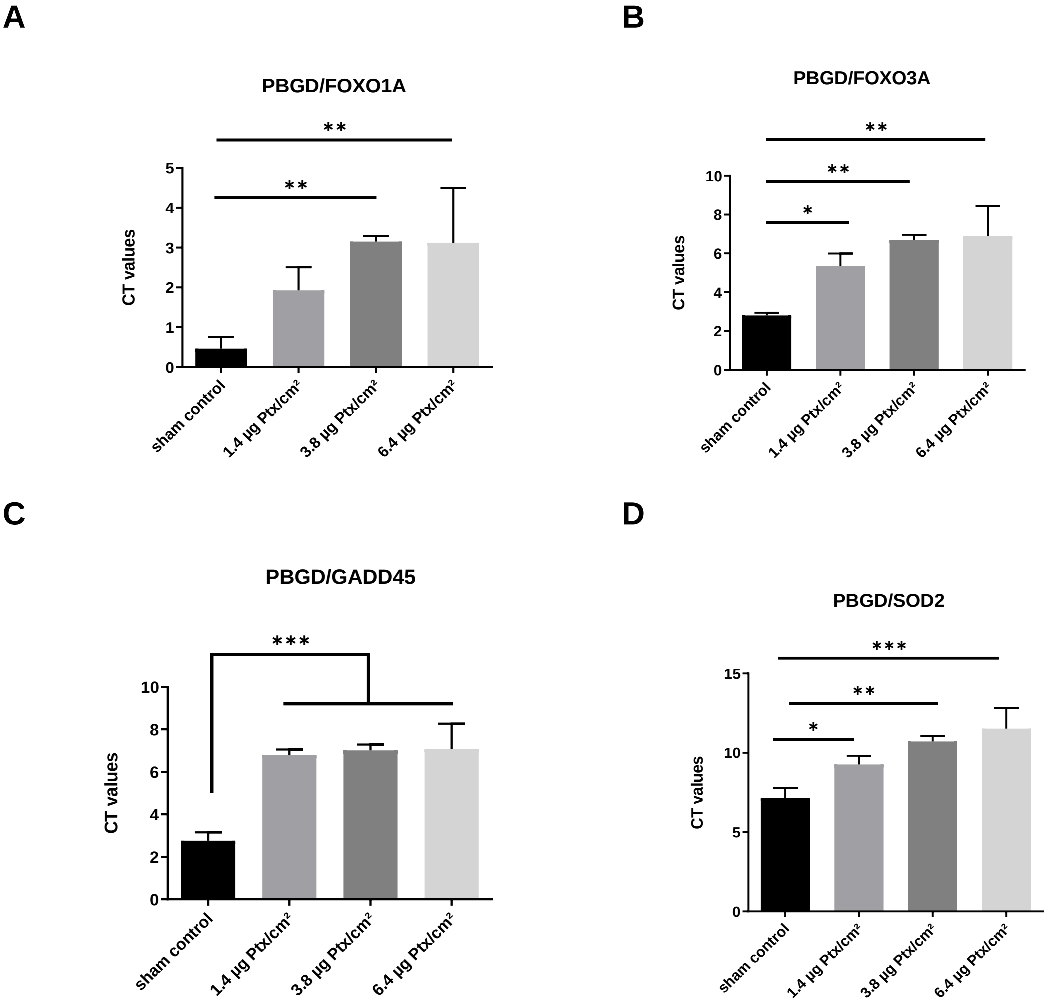

Figure 5.28: qPCR analysis of EA.hy926 RNA isolated from the coculture model (all values are presented relative to PBGD as housekeeping gene). **Panel A, B**: FOX transcription factors were activated by the treatment with slow-releasing Ptx-NP. **Panel C, D**: Furthermore, pro-apoptotic genes were upregulated. Data are expressed as mean ± SEM (n = 3 independent experiments). * $p \leq 0.05$, ** $p \leq 0.01$, *** $p \leq 0.001$

5.4.8 Comparison of transbarrier transport rates at submerged and ALI conditions

All studies with Ptx-NP were carried out at ALI conditions. However, most pre-clinical *in vitro* studies are performed under submerged culture conditions, i.e., the cells are completely covered with medium on the apical side. While for poorly polarizing cells such as A549 cells, this is likely not affecting the drug efficacy and toxicity if the dose is expressed in terms of mass per surface area (as done here; Lenz et al., 2014 [89]), it has been shown that cell culture conditions can substantially affect the biokinetics of both molecular [74], and nanocarrier based drugs [68].

Similar to the Ptx-NP biokinetics study described above, slow-releasing Ptx-NP were nebulized onto A549-Luc(IL-8) at ALI conditions and the cell deposited dose was assessed by the QCM (7 µg Ptx/cm^2; 4.8% loading efficiency of Ptx-NP. The same dose was pipetted and mixed into the apical medium of A549-Luc(IL-8) cultured at submerged conditions. A graphical depiction of both approaches is presented in figure 5.29A.

Both setups showed remarkable differences in the transport profile. At submerged conditions, only (10 ± 11)% of the total Ptx reached the basal compartment, indicating that the majority of Ptx-NP (74 ± 19)% remained in the apical medium (figure 5.29B). At ALI conditions, where Ptx-NP were nebulized on the cells, (51 ± 21)% of the total Ptx reached the basal compartment after 24 h. Consequently, the apical-to-basal transport of Ptx after aerosolization was enhanced by a factor of 5 as compared to submerged conditions. This could at least in part be due to the fact that nanoparticles are suspended in a relatively thick column of cell culture medium (here 0.48 cm) as compared to ALI conditions (ca. 25 µm [68]), and may not reach the cells within the available incubation time.

To explore this issue, an *in silico* sedimentation, diffusion and dosimetry (ISDD) model described by Hinderliter et al. (2010) [164] was used to calculate the cell delivered dose fraction of Ptx-NP. Assuming an effective particle density of 1.25 g/cm^3 for Ptx-NP [165] and a volume mean diameter of 260 nm, this model predicted that only 25% of the Ptx-NP, which are suspended in the apical medium, actually reach the cells within 24 h (figure 5.29C). With this information, the dependence of cell metabolic activity (WST-1) on cell-delivered dose could be determined for both ALI and submerged culture conditions. At submerged conditions, a dose of 9.2 µg Ptx/cm^2 was necessary to reduce the viability by 50% (figure 5.29D). On the other hand, a cell-delivered dose of 3.5 µg Ptx/cm^2 decreased the metabolic activity of ALI cultured cells by 50%. This shows that Ptx-NP are 2.6-fold more toxic under ALI conditions.

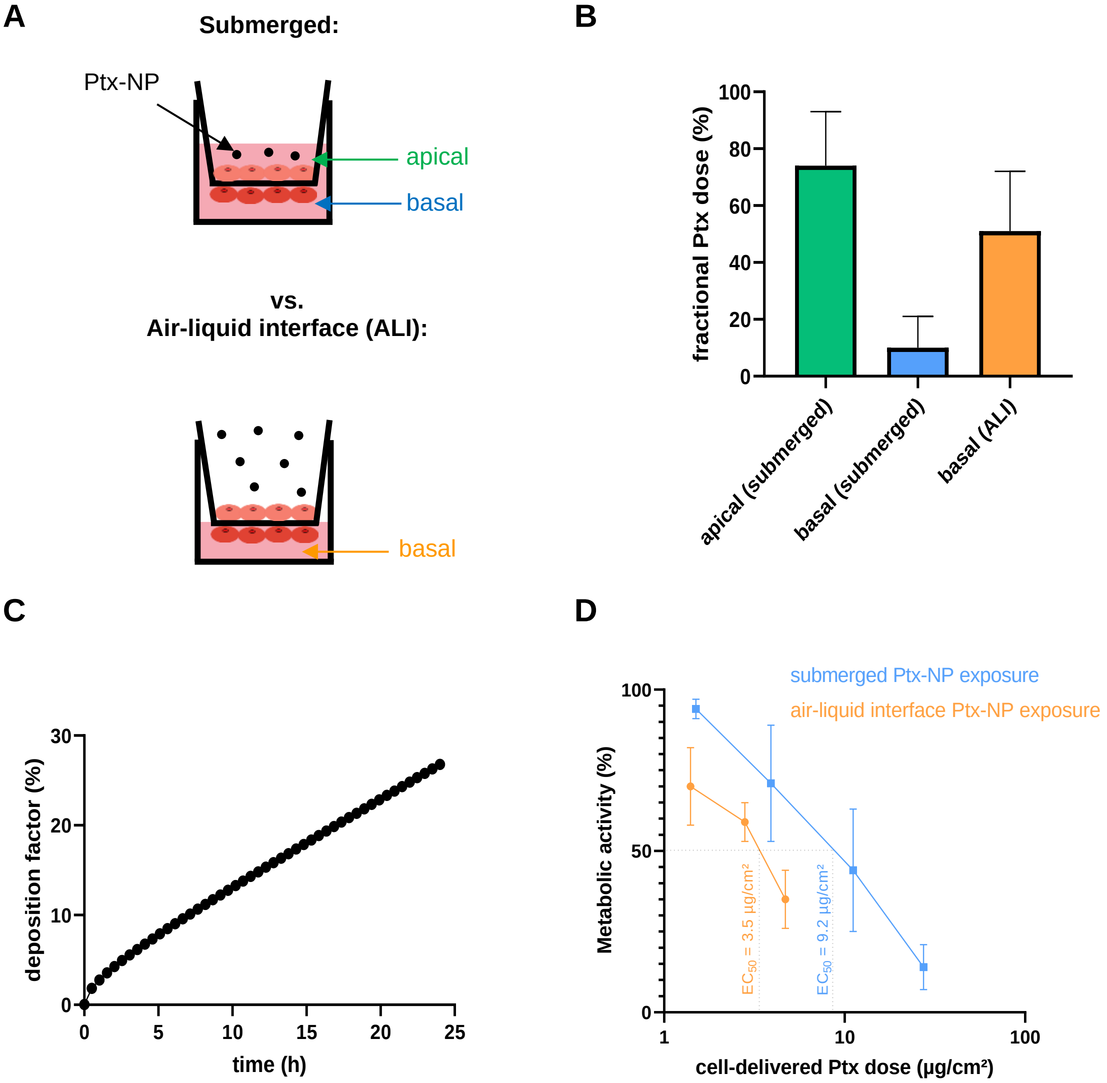

Figure 5.29: Comparison of slow-releasing Ptx-NPS transport across A549-Luc(IL-8) cultured at submerged and ALI conditions. **Panel A:** At submerged conditions, cells were covered with growth medium containing Ptx-NP (dose = 7 µg Ptx/cm²). In contrast to this, the same dose of Ptx-NP was aerosolized onto cells at ALI conditions. **Panel B:** Assessment of the fractional Ptx dose showed a weak transport of Ptx-NP (10 %) to the basal compartment at submerged conditions after 24 hours. On the other hand, the corresponding dose at ALI conditions was 5-fold higher. Data are normalized to the total Ptx dose (29.8 µg). **Panel C:** The deposition fraction at submerged conditions was modeled by an *in silico* sedimentation, diffusion, and dosimetry model (ISDD) [164]. Assuming an effective particle density of 1.25 g/cm³ for Ptx-NP [165] and a volume mean diameter of 260 nm, only 25% of the total (nominal) Ptx-NP in the apical medium deposited on the cells within 24 h. **Panel D:** Dose-response curve for metabolic activity (WST-1) at ALI and submerged conditions (taking this low cell-delivered dose fraction of 25% of nominal dose into account) The dose to achieve a 50% loss in metabolic activity (EC$_{50}$) was 3.5 µg$_{Ptx}$/cm² and 9.2 µg/cm² at ALI and submerged conditions, respectively. Data in panels B and D are expressed as mean ± SEM (n = 2 (panel B) – 3 (panel D) independent experiments).

5.4.9 Transbarrier transport of Ptx-NP in an *in vitro* PH disease model

All of the *in vitro* data presented above are based on healthy cell models of the lung without induced disease phenotype. On the other hand, in clinical settings, drugs are inhaled by patients. Hence, it is important to also perform *in vitro* drug testing in *in vitro* disease models.

For Ptx-NP, the relevant disease model is pulmonary arterial hypertension (PAH). To establish an *in vitro* PAH disease model, which is as described in the literature [19], the endothelial cell line EA.hy926 was challenged with TNF-α for 24 h prior to co-culturing it with healthy epithelial cells (A549-Luc(IL-8)) as described in the methods section (4.1). This TNF-α treatment of EA.hy926 cells leads to proinflammatory stimulation, which results in a decrease of TEER values and an increase of permeability [177].

For characterization of the effect of TNF-α challenge on endothelial barrier integrity, this issue was investigated prior to adding the A549-Luc(IL-8), i.e. immediately after the 24 h incubation with TNF-α and 2 h attachment to the basal side of the Transwell® insert. TNF-α challenge significantly disrupted the endothelial barrier integrity as evidenced by the dose-dependent increase in the endothelial paracellular permeability reaching a 2.7-fold increase (relative to TNF-α = 0) at the highest dose of 18 ng/cm² TNF-α (figure 5.30A). On the other hand, the metabolic activity of EA.hy926 cells was not substantially impaired due to TNF-α challenge (figure 5.30C), which is essential for the conduction of reliable biokinetics studies.

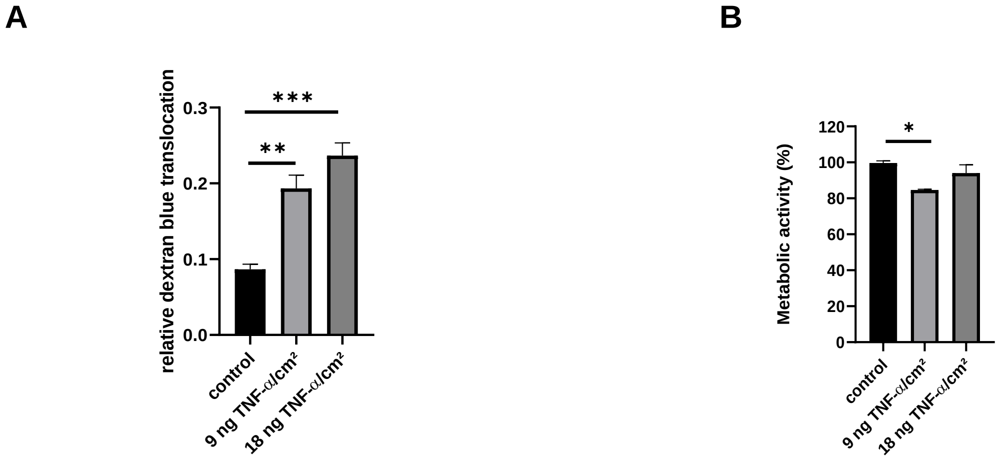

Figure 5.30: PAH-like modeling of endothelial dysfunction *in vitro* using a TNF-α challenge model described in the literature. **Panel A**: Dose-dependent increase of endothelial paracellular permeability one day after TNF-α treatment was observed. **Panel B**: TNF-α did not decrease the metabolic activity of the cells in a dose-dependent manner. Data are expressed as mean ± SEM (n = 3 independent experiments). * $p \leq 0.05$, ** $p \leq 0.01$, *** $p \leq 0.001$

The changes in endothelial barrier integrity were also substantiated by Actin-DAPI staining and fluorescence microscopy. Contrary to the control (no TNF-α addition), 18 ng/cm² TNF-α treatment led to a loss in the cellular connectivity as evidenced by the less intense and less sharp actin signal at cell-cell contacts (figure 5.31).

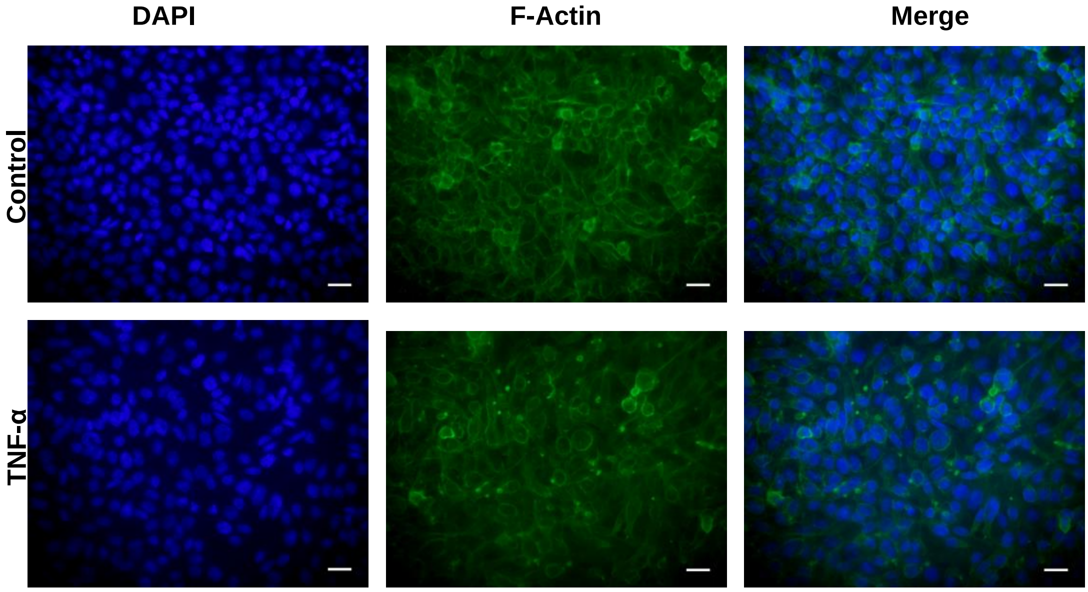

Figure 5.31: Fluorescence imaging of Actin-DAPI stained of EA.hy926 cells 24 h after TNF-α addition (18 ng/cm²) that led to morphological changes and a loss of cellular connectivity (less sharp actin signal at cell-cell contacts) in contrast to the control. Actin (cytoskeleton): green; DAPI (nucleus): blue Scale bar: 10 µm

For conduction of Ptx-NP biokinetics studies, the TNF-α challenged endothelial cells were integrated into a coculture system with "healthy" A549-Luc(IL-8) cells as described in the methods section (see section 4.1). Similar to the dextran blue (dye) analysis of inflammatory stimulated (TNF-α challenged) EA.hy926 cells alone, quantitative fluorescence spectroscopy was used to monitor translocation of the dye across the diseased coculture barrier model. The analysis revealed an even more pronounced dose-dependent increase of paracellular permeability by a factor of 2.5 and 5.8 for 9 ng/cm² and 18 ng/cm² TNF-α, respectively (figure 5.32A). This is consistent with the PAH-phenotypic feature of increased "leakiness" of the air-blood barrier [178].

To investigate possible effects of disease state on the biokinetics of Ptx-NP, slow-releasing Ptx-NP were aerosolized on the diseased coculture (cell-delivered dose 135.3 µg/cm², which corresponds to 5.8 µg Ptx/cm²), and the Ptx concentration in each compartment was assessed via HPLC for an incubation period of 24 h. This showed that there was no statistically significant effect of disease state on the apical/cell-associated Ptx dose during the various time points during the observation period of 24 h (figure 5.32B). Hence, in spite of up to 5.8-fold enhanced paracellular transport for the disease model (figure 5.32A), no increase in Ptx transport out of the apical/cell into the basal compartment (= 1 – apical/cell dose fraction) was observed for any of the investigated time points. This implies that also the transbarrier transport of Ptx was not affected by the disease state.

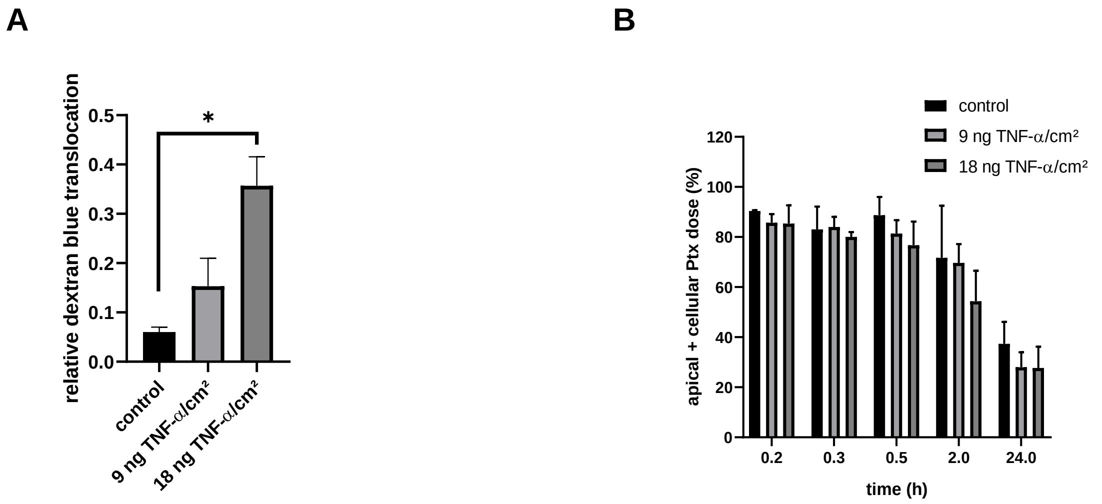

Figure 5.32: Assessment of barrier integrity of and (slow release) Ptx-NP biokinetics across the diseased (TNF-α challenged) epithelial-endothelial coculture (control = endothelial EA.hy926 cells without TNF-α challenge). **Panel A:** Relative dextran blue translocation after 24 h. The paracellular permeability of the diseased coculture model was significantly (up to 5.8-fold) increased as compared to healthy control. **Panel B**: Biokinetics of slow-releasing Ptx-NPS. No statistically significant reduction in Ptx storage in the combined apical and cell compartment could be measured for the diseased coculture, which also implies that the basal Ptx dose (trasnbarrier transport) is not affected by the disease state. Data are normalized to the delivered Ptx dose per Transwell® insert ((24 ± 1) µg) and expressed as mean ± SEM (n = 3 independent experiments). * $p \leq 0.05$

5.5 Application of the *in vitro*-based *in silico* PBPK model for the prediction of the *in vivo* PK of Ptx

In section 5.1.4, two *in silico* PBPK models were described, which showed predictive capacity for the CsA concentration in the blood of post-lung transplantation patients (PK profile), if the lung-to-blood transport rate was determined experimentally with our *in vitro* ALI epithelial cell barrier model (A549 cells) combined with aerosolize L-CsA delivery. The simple discrete model is now applied to predict the PBPK profile of inhaled Ptx-NP in clinical settings based on the *in vitro* biokinetics data for Ptx reported in chapter 5.4.3. Analogous to the L-CsA study, the following model structure was used:

1) Lung compartment with Ptx-NP deposition after inhalation
2) Blood compartment with lung-to-blood transport rate for Ptx, leading to an influx of Ptx into the blood
3) Loss (removal) compartment inducing depletion of Ptx in the blood as a result of metabolic Ptx degradation and/or excretion

For step 1), typically observed peripheral lung deposition values were used (10%, 20%, and 40% relative to an assumed nominal dose of 10 mg in the inhaler) to assess how patient- and device-specific uncertainties in lung-deposited dose fraction affect the predicted c_{max} levels.

For step 2), k_{LB} was calculated for each time layer by dividing the fractional change in basal Ptx dose of adjacent measurement points by the corresponding time interval, analogous to the L-CsA study. Transport rates (table 5.3) were derived from a fit curve through the Ptx-NP biokinetics as presented in chapter 5.4.3 (Ptx-NPF: $t_b = (0.5 – 11.9) * \exp(-0.6*t) + 11.9$, $r^2 > 0.98$; Ptx-NPS: $t_b = (-1.3 - 5.5) * \exp(-1.9 * t) + 5.5$, $r^2 > 0.99$).

Table 5.3: Transport rates for both Ptx-NP formulations, calculated from figure 5.23A,C.

time (h)	k_{LB} for Ptx-NPF (1/h)	k_{LB} for Ptx-NPS (1/h)
0	0.000	0.000
0.25	0.567	0.300
0.5	0.472	0.410
1	0.346	0.227
2	0.317	0.063
4	0.175	0.005
8	0.036	0.000
12	0.003	0.000
24	0.000	0.000

These transport rates were then used to calculate the lung to blood transported Ptx dose. To describe the depletion of Ptx in the blood compartment as a result of metabolic Ptx degradation and/or excretion for step 3), a Ptx PK study conducted by Huizing et al. (1995) was used, where Ptx was administered intravenously to patients [179]. Here, a mean fractional loss rate k_{loss} of 0.41/h was derived from the PK. A summary of the applied parameters is provided in figure 5.33A.

The modeled PK profile predicts a c_{max} level of (17.6 ± 5.4) ng/mL after inhalation of 10 mg fast releasing Ptx-NPF and a peripheral lung deposition of 10% (figure 5.33B). For the slow-releasing Ptx-NPS, the model predicts c_{max} levels of 9.3 ± 2.8) ng/mL assuming a lung deposition fraction of 10% and a nominal dose of 10 mg (figure 5.33C). For both of the formulations, a 20% and a 40% peripheral lung deposition led to 2-fold and 4-fold, respectively, increased c_{max} level (figure 5.33D), which indicates that the nominal dose is a linear determinant of c_{max} levels.

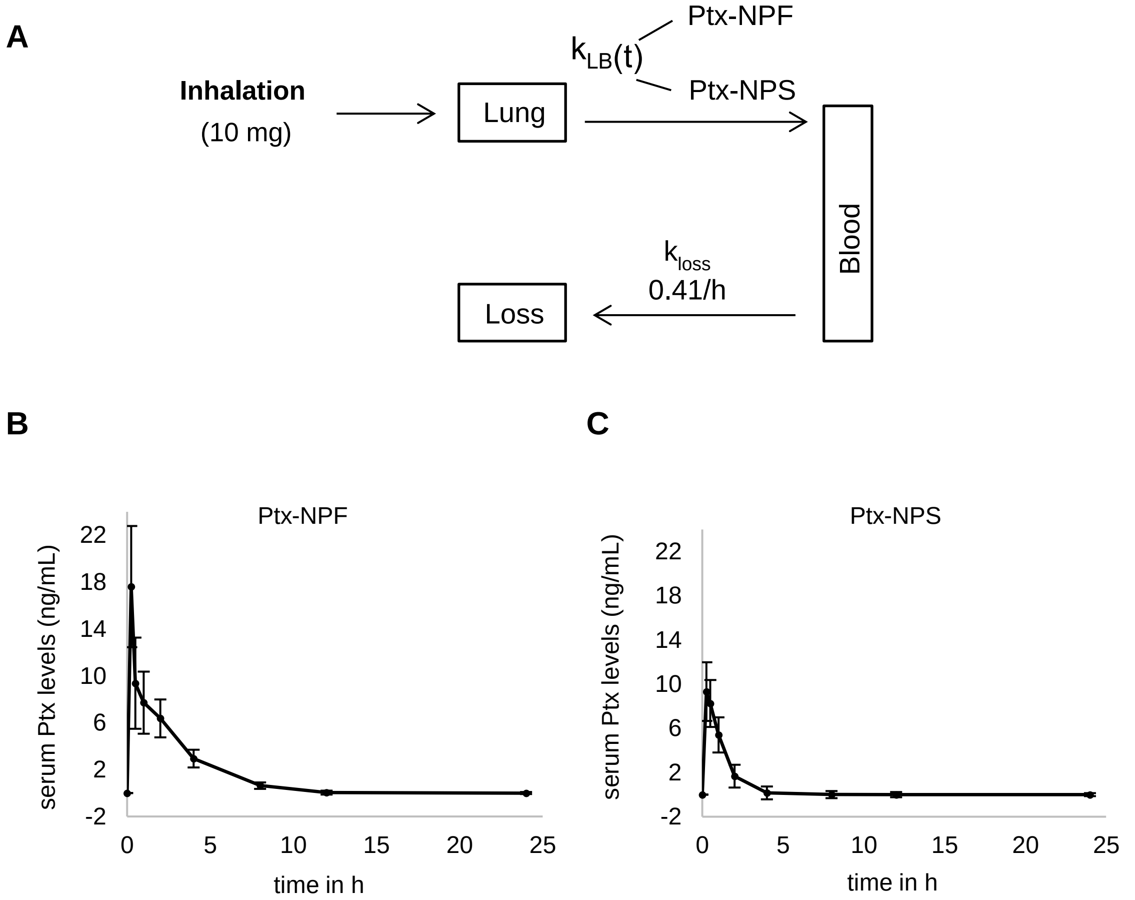

D

Lung deposition fraction	c_{max} for Ptx-NPF (ng/mL)	c_{max} for Ptx-NPS (ng/mL)
0.10	17.6 ± 5.2	9.3 ± 2.8
0.20	35.2 ± 10.3	18.7 ± 5.3
0.40	70.5 ± 20.7	37.3 ± 10.6

Figure 5.33: Application of the *in vitro*-based *in silico* PBPK model for the prediction of the *in vivo* PK of Ptx. **Panel A**: Scheme of our simple discrete PBPK model introduced in section 5.1.4. Experimentally determined *in vitro* transport rates (k_{LB}) of both types of inhaled Ptx-NP formulations were used to calculate the Ptx PK profile in humans. **Panel B, C**: Predicted Ptx PK levels (dots) for a nominal Ptx-NP dose of 10 mg and an assumed peripheral lung deposition of 10% based on our simple discrete *in silico* model, which includes *in vitro* cellular transport rates of Ptx-NP. Inhalation of fast-releasing Ptx-NPF led to 1.9-fold increased systemic Ptx levels as compared to slow-releasing Ptx-NPS. **Panel D**: c_{max} linearly scales with the lung deposition fraction for both types of inhaled Ptx-NP.

Error bars for the modeled data were calculated applying Gaussian error propagation on the *in vitro* Ptx-NP transport rates (figure 5.23).

6 Discussion

The human lung presents an interface between air and blood. From a clinical point of view, this provides a significant advantage as lung diseases can directly be targeted by inhalation therapy. However, several clearance processes in the lung decrease the dose of inhaled drugs, e.g., lung-to-blood transport of drugs by the lung epithelium. Consequently, epithelial permeability for drugs is one of the parameters, which influences the lung retained dose and determines the success of inhalation therapy.

To assess epithelial permeability *in vitro*, Transwell® insert-cultured lung cell epithelial lines are a prominent model, where the apical compartment represents the side of the lung, which is exposed to inhaled drugs, and the basal side the blood. Recent studies have shown that this model can be utilized to deliver relevant results, which bridge the gaps between *in vivo* and *in vitro*, and show the potential to ensure “the principles of the 3Rs (replacement, refinement, reduction)” of animal experiments [24]. For example, the model could be used to find optimized drug formulations in terms of increased lung tissue retention [73]. Further, *in vitro* apical-to-basal transport rates of gold nanoparticles were successfully combined with PBPK modeling to ultimately predict the gold nanoparticle levels in various rat organs [52]. Moreover, it was shown that the drug distribution in the different compartments (apical, cells, and basal) of the model after drug exposure can serve as an estimation of the drug dose in the lung after inhalation [68].

Overall, these studies significantly increased the clinical relevance of Transwell® insert models in terms of expectable dose ranges *in vivo and* selection of superior formulations for inhalation therapy. However, up to now, they do not provide quantitative *in vivo* translation of dose-response curves. We utilized the model to translate apical-to-basal transport rates of two nanodrugs (liposomal Ciclosporin A (L-CsA) and Paclitaxel-laden co-polymeric nanoparticles (Ptx-NP)) into pharmacokinetics profiles (human), aiming to answer:

- How do nanodrugs interact with lung epithelial cells and how are they transported?
- How do inflammatory conditions in the lung affect the transport of nanodrugs?

- How do different culture conditions (air-liquid interface vs. submerged cell culture) affect the efficacy and toxicity of the nanodrugs?

In the following, the obtained results to answer the questions will be discussed. The discussion will highlight the importance of air-liquid interface cell culture to simulate inhalation therapy *in vitro*, will clarify the interactions of L-CsA and Ptx-NP with lung epithelial cells, and, overall, will discuss the clinical relevance of our results.

6.1 ALI culture conditions are more physiological than submerged conditions

Traditionally, *in vitro* cell models of the lung have been cultured under submerged conditions. While this may be acceptable for interstitial cell types, it is not physiologic for lung epithelial cells, which form the air-tissue/liquid barrier in the lung [31].

The more biomimetic features of ALI models of the air-blood barrier have been discussed extensively in the literature [62, 63, 180]. Among others, ALI conditions allow the setup of more complex up and realistic to quadruple coculture models (e.g., macrophages, epithelial cells, fibroblasts, dendritic cells and/or endothelial cells) [78, 181], maintenance of epithelial lining fluids (e.g., lung surfactant) [79], aerosolized drug delivery directly onto the epithelium, and real-time measurement of the cell-delivered drug dose (e.g., quartz crystal microbalance) [88, 89, 93]. Especially the latter two aspects are highly relevant for biokinetics studies of nanodrugs as performed here since rapid and direct contact between nanodrugs and epithelial cells mimics the exposure scenario during inhalation therapy and cannot be obtained under submerged cell culture conditions where the nanoparticles (nanodrugs) are suspended in the medium for an extended period of time (more than 24 h depending on particle size, density, and medium height) due to low diffusivity and settling speed of nanodrugs in cell culture medium [164]. Albeit there have been comparisons of transbarrier transport and toxicity/efficacy of molecular drugs and nanoparticles under submerged and ALI culture conditions [74, 89, 182, 183], not much evidence has been provided for pharmacokinetics, efficacy and toxicity studies with nanodrugs, yet.

We found significant differences in the nanodrug transport between both culture conditions. Ptx-NP were not reaching the cells as rapidly as molecular Ptx due to the high diffusivity of molecules (< 10 nm in diameter) as compared to > 100 nm NPs. This was confirmed by combined DLS (size) measurement and ISDD particokinetics modeling described by Hinderliter et al., 2010 [164]. The model was used to predict the deposition fraction of Ptx-NP on submerged cultured cells. After 24 h, only 25% Ptx-NP deposited on the cells, indicating strong interactions with media ingredients. On the other hand, ALI cell exposure enabled direct deposition of the Ptx-NP onto the epithelial cells allowing immediate nanodrug-cell contact as experience during inhalation therapy in the lung. This will result in higher transbarrier transport rates for nanodrugs. This can be seen by comparing the transport rate and duration of transport of L-CsA reported for ALI conditions (this study) with those under submerged cell culture conditions compartment [73]. The transport rate and duration of L-CsA transbarrier transport at ALI is 1.42/h and 2 h, respectively, as compared to 0.007/h and > 24 h (largest observed time point) reported for submerged culture conditions [73]. Thus, ALI conditions provide 200-fold higher dose rates and much shorter transbarrier transport periods. This phenomenon is often referred to as a “burst-like” transport profile (high rate, short duration), which is consistent with the L-CsA PK profile observed in clinical settings [17, 68, 166].

Another difference in ALI vs. submerged culture conditions concerns the onset of toxicity after Ptx-NP exposure. In this study, A549-Luc(IL-8) cells responded more vulnerable to Ptx-NP under ALI conditions (2.6-fold lower EC_{50} value for WST-1 assay) as compared to pipetted Ptx-NP at submerged conditions. This may be due to the strong interactions of Ptx-NP with media ingredients under submerged conditions, which could prevent direct nanodrug-cell interactions.

Thus, ALI cell culture conditions are crucial for both pharmacokinetics as well as efficacy/toxicity studies.

6.2 Evaluation of dose-controllable delivery of aerosolized nanodrugs

To transfer *in vitro* results into the clinical setting (dose finding), assessment of the cell-delivered drug dose is an essential step. In standard submerged cell culture systems, typically the nominal drug concentration in the medium is reported, which can be readily converted into dose by multiplication with the volume of the cell culture medium. This approach is correct for molecular drugs, since drug molecules are small (<10 nm in diameter) and highly diffusive [86], which gets them into contact with the cells almost immediately (within minutes). For ca. 100 nm nanodrugs, their mobility due to diffusion (and sedimentation) is extremely slow resulting in only ca. 25% of the administered drug dose reaching the cells within 24 h (figure 5.29C). Hence, preclinical testing of nanodrugs is difficult with standard submerged cell culture systems, since the cell-delivered dose is highly uncertain.

To overcome this issue, we used the VITROCELL® Cloud 6 technology to deliver L-CsA and Ptx-NP to the *in vitro* cell-models in aerosolized form. Previous studies have shown that the VITROCELL® Cloud 6 QCM can be used for accurate measurement of the cell-delivered doses of various types of nanoparticles with an accuracy of 3.4% [93]. We also found that the QCM of the Cloud system could reliably measure the cell-delivered drug dose. For both types of drugs, there was a linear correlation ($r > 0.98$) between QCM-measured cellular dose and nanodrug concentration in the nebulizer (for a constant volume of nanodrug suspension) over a wide dose range (1 – 70 µg/cm² for L-CsA, 4.5 – 113 µg/cm² for Ptx-NP). Consequently, the desired cell-delivered nanodrug dose can be selected by adequate dilution of the nanodrug suspension.

However, for Ptx-NP, a large difference of 45% between analytically (HPLC) determined drug dose on the cells (in the Transwell® insert) and QCM-derived molecular drug dose was found, which is larger than typically reported 10 – 20% difference for fluorescent tracers or nanoparticles [93]. This is due to the fact that with nanocarriers additional uncertainties are introduced, especially a relatively large uncertainty in nanocarrier loading and efficiency. Based on previous work at the HMGU (Schmid lab), we estimate the upper limit of systematic errors in the following key experimental parameters: loading efficiency (10%), combined QCM and HPLC measurement accuracy (10%), deviation between insert- and QCM deposited dose (15%), and retrieval efficiency of Ptx from the three compartments of the insert (20%). Based on this, the upper limit for experimentally observed differences between QCM and insert dose of Ptx is 55%, i.e., the measured difference of 45% is still within acceptable experimental uncertainties.

Hence, it can be concluded that the QCM is capable of measuring the cell-delivered dose of drugs loaded into nanocarrier systems, albeit with potentially relatively low accuracy. All in all, QCMs allow real-time measurement of the cell-delivered drug dose, which enhances data quality and alleviates the need for more complex dosimetric analyses such as HPLC-MS/MS measurements.

6.3 *In vitro* cellular uptake and transbarrier transport of L-CsA and Ptx-NP

After the dose-controllable aerosolized delivery of the nanodrugs was ensured, we performed dose-controlled particokinetics studies with an *in vitro* cell-model of the air-blood barrier consisting of alveolar type II-like A549-Luc(IL-8) cells, which are expected to behave identically to the more widely used regular A549 cells (without luciferase reporter) [184]. Here, we started with L-CsA. L-CsA is one of the very few substances, which are suitable for the establishment of validated *in vitro* physiologically-based *in silico* pharmacokinetics models for inhaled nanodrugs, since two clinical PK studies for L-CsA have been reported in the literature, one of them with actual measurement of the pulmonary L-CsA dose and one of them starting as early as 15 min after inhalation with monitoring the CsA blood levels ([17, 166]).

The physiological relevance of an alveolar type II cell barrier is questionable since most of the human alveolar surface is covered by alveolar type I cells (92.9%) [31]. Recent advances towards providing a readily available alveolar type I cell model include the HAELVi cell line (InSCREENeX GmbH, Germany). This is an immortalized primary lung epithelial cell line, which represents some of the main characteristics of alveolar type I cells, namely the formation of tight junctions associated with high trans-epithelial electrical resistance

(> 1000 Ω*cm²), low permeability of hydrophilic markers, the presence of caveolae, expression of caveolin-1, and absence of surfactant protein C [70]. While these characteristics are highly relevant for *in vitro* transport studies, this cell line was not available when we needed to decide on the most suitable cell type for this study. The recently introduced EpiAlveolar cell model (Matek, USA) was also not commercially available a few years ago, and is not established for *in vitro* transport studies [82]. Hence, for lack of an established more physiologic cell culture model of the alveolar air-blood barrier, A549-Luc(IL-8) cells were used here.

The L-CsA particokinetics study showed an almost constant lung-to-blood transport rate of k_{LB} = 1.42/h, which only decreased sharply at 4 h, reaching zero at 8 hours after the end of aerosol exposure. At first sight, k_{LB} appears to be substantially (2.6-fold) higher than the 0.55/h reported by Schmid et al. (2017)[68] for the very same cell model and type of aerosol exposure chamber, albeit with a somewhat different L-CsA formulation (calculated from Table 2: k_{LB} = 0.0022/(min*cm^2)*60 min/h*4.2 cm^2 = 0.55/h). If the bias due to partial retainment of L-CsA by the membrane of the Transwell® insert is accounted for (only 68.5% L-CsA can pass through the Transwell® insert without cells, figure 5.2B), the transport rate increases to 0.80/h (0.55/h/0.685), which is 1.8-fold smaller than the value reported here (1.42/h). Albeit this difference is still not negligible, it is probably justifiable by variabilities in cell characteristics (e.g., barrier tightness) and differences in L-CsA formulation. This also demonstrates that for *in vitro* transbarrier transport measurements with nanodrugs, artefacts due to the membrane of the Transwell® insert should be accounted for by including a membrane-only control (insert without cell).

Since the transbarrier transport of L-CsA by A549 cells was measured by HPLC analysis of the CsA concentration in the basal compartment (and in the other compartments of the Transwell® insert cell model), it was first unclear whether the CsA molecules are transported across the cell barrier as part of the intact liposomal carrier or as free molecular drug released from the carrier. To gain more insights into this issue, fluorescently labeled liposomes (FRET liposomes) were manufactured according to Li et al. (2018)[160] and used to clarify cellular uptake and transport after nebulization. The ability to discriminate between intact and dissolved FRET liposomes was demonstrated by the reduction of initial total FRET fluorescence intensity to < 7% after Triton-X100 digestion of the liposomes. The relatively larger remainder of < 20% as seen from the biokinetics experiments combined with the absence of intact liposomes using DLS analysis indicates that an effective detergent such as Triton-X can destroy all of the liposomes, but it cannot dissolve all fragments of the lipid bilayer of the liposomes, still leaving some of the two FRET dyes in close proximity yielding a detectable FRET fluorescence signal. Hence, it is conceivable that any of the transbarrier transport across a cell barrier does also not completely eliminate the FRET signal [160]. This could explain the rapidly reached (1 h), constant FRET signal of ca. 20% in the basal medium in spite of the absence of intact liposomes in the basal medium (DLS measurements).

As prerequisite for using aerosolized delivery of FRET liposomes, it is important to note that nebulization of liposomes did not deteriorate the structural integrity of the FRET liposomes. This can be concluded from the fact that nebulization did not result in appearance of a sub-liposomal size fraction in the DLS size distribution. This is consistent with previous studies reporting morphological deformations after nebulization with a vibrating mesh nebulizer (somewhat elongated rather than perfect spherical liposomes), but no complete loss of structural integrity of the liposomes [68].

Our mechanistic cellular uptake study with mechanism-specific inhibitors revealed that caveolae-mediated endocytosis was found to be involved in active uptake of FRET liposomes by A549 cells, but not clathrin-mediated endocytosis and pinocytosis. Endocytosis is a well-known pathway of cellular nanoparticle uptake [185, 186]. It is also well known that the relevance of different endocytic uptake can depend on particle size [62]. This size-dependence of uptake mechanism was also observed for liposome uptake by Caco-2 cells by Andar et al. (2014), where caveolae-mediated endocytosis was involved in the uptake of 40.6 and 72.3 nm liposomes, while clathrin-mediated endocytosis governed the uptake of 97.8 and 162.1 nm liposomes [187]. It is evident from our study, that for A549 cells the caveolae-mediated size region is shifted to larger sizes (130 nm).

In addition to active cellular uptake, also passive drug transport due to fusion of the lipid bilayer of liposomes with the cell membranes was reported in HeLa cells (human cervix epithelial cells) [188]. As this passive fusion process does not require cellular activity, it is likely to be fast and independent of cell type. While it is unclear, if membrane fusion leads to separation of the two FRET dyes (DiI and DiD) and to a subsequently reduced FRET fluorescence signal, it is likely that membrane fusion is not affected by the presence of uptake inhibitors, since these inhibitors are not a detergent and will therefore not destroy the lipid bilayer of the liposomes. In any case, fusion may introduce some residual FRET signal in the basal medium [160], but this will be independent of the presence or absence of any uptake inhibitor and will therefore not interfere with the effect of uptake inhibitors on FRET-based cellular uptake.

The kinetics of transbarrier transport of liposomes with hydrophobic loading (e.g., DiI-DiD FRET dyes or CsA stored within lipid bilayer of liposomes) with and without inhibition of caveolae-mediated endocytic uptake (Filipin) strongly suggests that both a fast-passive and a slower-active transport process are involved in transbarrier transport of hydrophobic drugs carried by liposomes. For both CsA and FRET liposomes at 0.1 h after the aerosol delivery, ca. 50% of the cell-delivered dye/drug has left the apical compartment independent of the presence of uptake inhibitors, while 80 - 95% of the delivered drug has reached the basal compartment at 2 h (independent of endocytic uptake inhibition). Only at 0.8 h, there was a statistically significant reduced transbarrier transport under the influence of inhibition of endocytosis (for FRET liposomes; no data for CsA). Thus, endocytic uptake cannot explain the fast initial transbarrier transport, but affects the transport kinetics at ca. 1 h. For later time points (2 h), the activity of the inhibitor has ceased so that there was not statistically significant difference in transport kinetics w/o inhibitor at 2 h (5 - 20% remains in the apical compartment for FRET dyes and CsA).

Taken together, this suggests that for liposomes loaded with a hydrophobic drug (here: CsA or DiI-DiD FRET dye), which is integrated into the liposomal bilayer, the following mechanistic and kinetic conclusions can be drawn:

i) Paracellular transport does not play a significant role in transbarrier drug transport, since no intact or fractions of liposomes were found in the basal compartment (DLS measurements). This implies that all of the CsA in the basal medium is available in its molecular form (not liposomal form).

ii) Between 40% and 60% of the delivered drug is rapidly transported (< 0.1 h) across the A549 cell barrier likely due to a passive transport process such as liposomes-cell membrane fusion [188]

iii) Active cellular uptake due to caveolae-mediated endocytosis is slower (ca. 0.8 h – 2 h) and experienced by 30 to 45% of delivered drug

iv) 5% - 20% of the drug remains in the apical/cell compartment for at least 24 h.

v) The apical-basal (lung-blood) transport coefficient is constant within experimental uncertainties during the entire significant transport period (< 2 h) at k_{LB} = 1.42/h.

It is important to note that similar *in vitro* particokinetics results have been found for both slow- and fast-release co-polymeric NPs loaded with (hydrophobic) Paclitaxel (Ptx-NP). Using A549-Luc(IL-8) cells as barrier model, we found:

i) Paracellular transport does not play a significant role in transbarrier transport of Ptx-NP

ii) Between 14% (fast-releasing Ptx-NPF) and 26% (slow-releasing Ptx-NPS) of the delivered drug is rapidly transported (< 0.2 h) across the A549 cell barrier, likely due to a passive transport process [188]

iii) Active cellular uptake due to caveolae-mediated endocytosis is slower (ca. 0.3 h – 0.8 h) and experienced by 40% to 50% of delivered drug (slow-releasing Ptx-NPS)

iv) 33% (fast-releasing Ptx-NPF) - 70% (slow-releasing Ptx-NPS) of the drug remains in the apical/cell compartment for at least 24 h.

v) The apical-basal (lung-blood) transport coefficient is decreasing by 45% for the fast-releasing Ptx-NPF formulation during the entire period of significant apical-basal transport (< 2 h). For the slow-releasing formulation, a decrease by 80% was observed 2 h after the nebulization. This indicates that the storage of Ptx in the lung compartment is superior to the lung-blood transport for both formulations.

This degree of similarity between the two types of nanodrugs investigated here is particularly interesting if we consider that liposomes (lipid vesicle) and copolymeric NPs are fundamentally different in terms of material type and rigidity (liposomes: soft; NP: hard), but very similar with respect to size range (L-CsA: 40 – 100 nm; Ptx-NP: 140 – 200 nm). Thus, size is possible more relevant characteristics than material and rigidity for cellular uptake and transbarrier transport of (hydrophobic) drugs. We add as a caveat that the situation may be different for hydrophilic drugs, since – at least for liposomes - hydrophilic drugs are stored within the vesicle and not in the lipid bilayer as for hydrophobic drugs [189].

Based on the *in vitro* results, the following conclusions can be drawn for the fate of liposomes after inhalation *in vivo*. First, it is likely that passive L-CsA transport will determine the lung-to-blood transport after inhalation at a similar rate and possibly at an even larger relative magnitude (> 50%), since passive transport processes may be quite similar independent of the complexity of the barrier. On the other hand, active endocytic uptake and transbarrier transport may be somewhat slower in humans due to the more complex air-blood barrier in the lung. This issue will be investigated below when comparing transport across an epithelial monoculture as compared to an epithelial-endothelial coculture model. Secondly, CsA (and Ptx) in the blood will be available in its molecular form (not encapsulated in liposomes) as DLS measurements confirmed the absence of intact nanocarriers in the basal medium.

A few other aspects, which are likely to affect transbarrier drug transport, should be considered and explored for relevance in the future. Lung surfactant has been shown to increase cell-association of nanodrugs [79]. Also, the effect of primary cell culture models such as immortalized alveolar type I cells (hAELVI [70]) as well as the transport of these nanodrugs across published breathing-induced cyclic stretch models ([190]) should be explored.

6.4 Advanced cell culture models and their effect on particokinetics

We further aimed to study L-CsA and Ptx-NP particokinetics in scenarios, which are more realistic *in vivo*.

One strategy, which was applied in the present work, was the investigation of L-CsA transport under inflammatory conditions. It has been observed that, *in vivo*, inflammatory processes lead to enhanced epithelial permeability due to disrupted tight junctions [119]. To transfer this observation to the *in vitro* model in the present study, TNF-α was added into the basal compartment of Transwell® insert cultured A549-Luc(IL-8) cells 24 h before the exposure to L-CsA. Dextran blue assay 24 h after TNF-α incubation revealed that epithelial permeability was increased by a factor of 4 for a TNF-α dose of 16.1 ng/cm², indicating increased possibility for paracellular transport of L-CsA. However, L-CsA transport analysis revealed constant CsA doses in the apical/cell compartment over the entire monitoring period. Together with the DLS results (no intact particles in the basal compartment), this further confirmed that paracellular transport does not play a significant role in transport of nanodrugs. From a clinical point of view, this demonstrates a significant advantage for the use of liposomal nanocarriers in the treatment of lung diseases such as bronchiolitis obliterans (BOS). The incorporation of CsA into liposomes can based on the *in vitro* results, prevent a fast clearance through the paracellular route and finally lead to an improved lung retained dose in inflammatory conditions. Further, the *in vitro* results are consistent with two reported *in vivo* studies. Patel et al. (2016)[191] administered lipid nanocarriers with an incorporated radioactive label to LPS-treated mice and the respective saline control group. Assessment of the radioactive label in all organs revealed that there was no faster clearance of the lipid nanocarriers under inflamed conditions [191], indicating that the lung-retained dose of the nanocarriers remained constant in inflammatory conditions. Arppe et al. (1998)[46] found equal CsA levels in healthy and inflamed lungs after the administration of CsA-liposomes to mice. Consequently, the lung clearance of CsA incorporated into liposomal nanocarriers was not enhanced under inflammatory conditions [46]. On the other hand, severe outcomes may have to be expected for hydrophilic drugs as the translocation of the hydrophilic paracellular tracer dye dextran blue increased by a factor of 4 for 16.1 ng/cm² TNF-α. One example for a drug, which is transported by the paracellular transport route, is Tobramycin [192]. *In vivo*, Omri et al. (1994)[193] investigated the lung retention of Tobramycin after administration to rats (healthy vs. infected (bacterial infection) lungs). They found that the Tobramycin concentration in the infected (bacterial infection) lungs was below the detection limit already 0.25 h after application. In the healthy control group, Tobramycin was detectable 2 h after the application. More importantly, the administration of Tobramycin as a liposomal formulation allowed the detection in both groups even after 16 h [193]. This confirms that liposomal drug formulations prevent a fast depletion of the lung retained dose by the paracellular route.

Another strategy, which was applied to increase the relevance of the *in vitro* model of A549-Luc(IL-8) cells, was the addition of EA.hy926 endothelial cells on the basal side of the Transwell® insert for the Ptx-NP studies. This did not increase the barrier resistance against particle transport, as the Ptx dose in the basal compartment after Ptx-NP exposure was either comparable to the monoculture of A549-Luc(IL-8) cells (fast-releasing Ptx-NPF) or even increased (slow-releasing Ptx-NP). Moreover, TEER values and dextran blue translocation between the mono- and the coculture were comparable, which is in line with previously reported results [78, 83]. One initial hypothesis for the accelerated transport of Ptx-NP by the coculture model was that EA.hy926 led to opened tight junctions of A549 cells, e.g. via cross-talk [194]. However, it has been observed that Ptx is hardly transported by the paracellular route of epithelial cells [195]. Another hypothesis was additional transport by either the endothelial paracellular or the endothelial transcellular route. Both transport pathways for Ptx are described for endothelial cells [196, 197]. Thus, it can be hypothesized that both (para- and transcellular) pathways accelerated Ptx transport after addition of endothelial EA.h926 cells to the *in vitro* model. Consequently, our results confirm that the addition of EA.yh926 cells lead to accelerated transport of nanodrugs (slow- and fast-releasing Ptx-NP) and dextran blue. However, the impact of increased paracellular permeability of coculture models *in vivo* has not been clarified yet [198].

As Ptx-NP are in preclinical development for the treatment of pulmonary arterial hypertension (PAH), another strategy to enhance the clinical relevance of the co-culture model was the investigation of Ptx-NP transport by a diseased *in vitro* PAH model. One of the characteristics in the development of PAH is an impaired lung endothelium, which is among others initiated by inflammatory conditions [178, 199-201]. TNF-α was found to play a prominent role as it promotes a PAH phenotype [202] and is, in addition, considered as a target for the treatment of PAH [203]. To establish an *in vitro* PAH disease model, EA.hy926 cells were challenged with TNF-α for 24 h prior to establishment of a coculture with A549-Luc(IL-8) cells. This demonstrated a higher permeability, which led to an increase of the paracellular transport marker dye dextran blue. In comparison to the approach by Hermanns et al. (2004), who added TNF-α into the basal compartment leading to activation of both cell lines in an epithelial-endothelial co-culture model representing the pulmonary air-blood barrier [204], the enhanced permeability could directly be attributed to endothelial cells in the present work. The diseased coculture model was then exposed to Ptx-NP. Although the paracellular permeability was increased due to challenged EA.hy926 cells, the transbarrier transport of Ptx-NP, which were aerosolized on the epithelial cells on the apical side, was non-significantly changed and the cellular association of Ptx remained constant. This suggests that the interaction of aerosolized Ptx-NP with the epithelium outweighed the transport of Ptx by challenged endothelial cells. Further, it promises a significant advantage for the use of co-polymeric nanocarriers in the treatment of PAH, as the increased endothelial permeability did not significantly decrease the cell-association of Ptx.

All in all, the applied strategies confirm the potential of drug carrier systems in the therapy of lung diseases associated with inflammatory conditions as a fast clearance via the paracellular route is avoided.

6.5 Evaluation of the *in vitro* physiologically-based *in silico* pharmacokinetics

Another goal of this thesis was to increase the clinical relevance of the L-CsA and Ptx-NP particokinetics studies by predicting the pharmacokinetics (PK) in human based on the obtained A549-Luc(IL-8) cellular nanodrug transport rates. Here, we applied the concept introduced by Bachler et al. (2015), who assessed A549 cellular transport rates of gold nanoparticles (*in vitro*) and combined the rates with PBPK modeling (*in silico*) to predict organ doses for the same set of gold nanoparticles in mice *(in vivo)* [52]. However, we focused on one compartment only (blood) and predicted the dose as a function of time to ultimately obtain the pharmacokinetics. All in all, three steps were introduced to translate the L-CsA particokinetics into pharmacokinetics.

First, the lung deposited L-CsA dose for the clinical PK study has to be obtained. In general, this can either be accomplished by using computational aerosol-lung deposition models (e.g. MPPD model, Miller et al. (2016)[205]), by estimating this from known average aerosol deposition fractions for the specific nebulizer used (here: eFlow® nebulizer, Pari Pharma GmbH, Germany; ca. 20 – 40% of the invested dose), or by using dosimetry data from a comparative study. The latter is the case here since in the L-CsA inhalation study, which is reported by Behr et al. (2009) [17], the peripheral lung deposition of CsA was determined from radiometric measurements as 22% of the nominal dose.

Secondly, the dose, which is transferred from the lung into the blood, has to be obtained. Here, we used the results from the L-CsA particokinetics studies to express the transported dose as the parameter k_{LB}. Interestingly, also cell-free models have recently been introduced to represent the air-blood barrier *in vitro* and to simulate lung-blood transport. One example is the DissolvIt technology, which uses a polycarbonate membrane to resemble the *in vivo* air-blood barrier *in vitro* [206]. It was shown that the absorption of inhalable drugs by the membrane could successfully be transferred into pharmacokinetics in patients by PBPK modeling [207]. However, our goal for this study was to clarify the fate of nanodrugs after cellular transport and to enhance the *in vivo* relevance of Transwell® insert models – hence, we used the insert model.

Thirdly, the depletion rate of CsA in the blood as a result of metabolic CsA degradation and/or excretion has to be obtained. In general, one can use reference clinical studies to describe the elimination and excretion of the drug from the blood ([52, 61, 208, 209]) or one can use software such as PK-Sim ([208, 210]), which summarize parameters that contribute to elimination and excretion of commonly used drugs in the blood. In the present work, a published[166] L-CsA PK profile was utilized to describe the depletion of CsA in the blood and finally expressed as the *in silico* input parameter k_{loss}.

The combination of the three steps showed that the modeled and published PK data agreed within experimental and modeling uncertainties, and showed that the combination of *in vitro* and *in silico* approaches demonstrates excellent potential to deliver *in vivo* relevant results.

The concept was also applied to predict the Ptx PK in human after inhalation of slow- and fast-releasing Ptx-NP. In comparison to the CsA PK, Ptx c_{max} levels were 2.8-fold (fast-releasing) and 5.1-fold (slow-releasing), respectively, reduced for a comparable lung deposition fraction since max. k_{LB} values for both Ptx-NP formulations (Ptx-NPF: $k_{LB,max}$ = 0.56/h, Ptx-NP: $k_{LB,max}$ = 0.30/h) were significantly lower than for L-CsA (1.42/h).

From the predicted PK profiles, the following conclusions can be drawn:

i) The nominal dose is a linear determinant of the maximum serum level (as seen for the Ptx-NP model)

ii) The model promises low systemic Ptx levels after inhalation of Ptx-NP. As comparison: Intravenous application of 10 mg Ptx would lead to 10-fold increased c_{max} levels of ca. 250 ng/mL (reference studies: [211] or [179])

iii) Lung-to-blood transport of aerosolized nanodrugs is the main factor, which leads to a reduction of the lung-associated drug dose after inhalation. The model did not consider clearance of nanodrugs by alveolar macrophages, which are typically involved in clearance and metabolism of inhaled nanoparticles [21]. It can thus be concluded that macrophages do not interfere in the lung-blood transport of liposomal and polymeric drug formulations. This can be explained by the fact that phagocytosis by alveolar macrophages typically occurs for sizes > 1 µm [212], and the nanodrugs were below this threshold.

iv) Transwell®-insert cultured epithelial cells are an efficient model to predict the pharmacokinetics of aerosolized drugs. For Ptx-NP, k_{LB} values for a more physiological model (A549-Luc(IL-8) epithelial cells and EA.hy926 endothelial cells) were available. However, L-CsA

> modeling showed that A549-Luc(IL-8) cellular transport rates are sufficient enough to show a match to clinical L-CsA data. Hence, we used epithelial rates for the modeling of the Ptx pharmacokinetics.

All in all, A549-Luc(IL-8) cells were successfully used as *in vitro* model for the pulmonary air-blood barrier. This allowed the calculation of the CsA and Ptx pharmacokinetics, which was successfully validated for CsA by comparison with published clinical profiles.

6.6 Comparison of clinical pharmacokinetic parameters for various drugs

The role of the nominal dose as linear determinant of c_{max} levels was confirmed by analyzing maximums serum levels of published inhalation studies. The comparison of c_{max} levels of various drug formulations (L-CsA, liposomal Amikacin, mixture of free and liposomal Ciprofloxacin, Levofloxacin, and Tobramycin) after inhalation as a function of the nominal dose showed a correlation of 92%. This is surprising as the correlation includes drugs with and without drug carrier systems, patients with different diseases (cystic fibrosis, bronchiolitis obliterans, and non-cystic fibrosis bronchiectasis), and different types of nebulizers. However, it is important to mention that the antibiotic Levofloxacin was excluded from the correlation as it showed a more than 2-fold higher c_{max} level as compared to the fit. This can be a consequence of high variabilities in lung deposition, which directly influence c_{max} levels [213]. Especially for inhalable antibiotics used for the therapy of cystic fibrosis, high “between-subject variabilities” [214] are common, i.e., 50% - even 100% of the mean c_{max} value [169]. Taking this variability into account, it can be assumed that the 2-fold increased c_{max} level of Levofloxacin is non-significant compared to the correlation of the other investigated drugs.

Focusing on L-CsA, the correlation suggests that CsA molecules are released once the liposomes reach the epithelial barrier as the slope of the linear curve describing c_{max} after inhalation of CsA and L-CsA ($c_{max} = 1.7 * 10^{-6}$ mL^{-1} * nominal dose), respectively, was similar to the one derived from all of the drugs (c_{max}

= (2.7 ± 1.1) (2 SD) * 10^{-6} mL^{-1} *nominal dose). This hypothesis is supported by our *in vitro* L-CsA transbarrier studies. They showed the absence of intact liposomes in the basal compartment and confirmed an initially high transport of CsA into the basal medium (blood). On the other hand, the liposomal nanocarriers majorly remained cell-associated. Consequently, an initial burst of the liposomes occurred, typical for aerosolized nanocarriers [215]. Transferring this result to the *in vivo* side, it can be suggested that liposomes majorly burst after lung deposition, leading to high drug dose, which is transported into the blood circulation in a similar way as the inhalation of the free drug counterpart.

However, the ultimate goal of inhalation therapy is to target the lung – but there are challenges to characterize the fate of liposomes *in vivo* after inhalation. Currently, two methods are majorly used to evaluate the lung deposition of inhaled drugs in human. One of them is to estimate the lung deposition of inhaled drugs indirectly via comparing the PK of the drug in the blood [213]. However, the initial burst of drugs entrapped in nanocarriers and the comparable c_{max} values, as observed in correlation to the nominal dose, make it challenging to highlight the advantages of nanocarrier systems. In other words, prolonged interactions at the lung side do not necessarily result in reduced systemic drug levels [216]. However, c_{max} can be used to evaluate effective lung deposition, according to Strong et al. (2018)[216]. If this value is achieved within 5 – 30 min, it can be concluded that the drug was sufficiently distributed in the lungs [216]. The other method to estimate the lung deposition is γ-scintigraphy [213], which images lung deposition of nanocarriers modified by radioactive labels [51] [17]. For liposomes, however, this method demonstrates the disadvantage that the fate of the liposomal shell can be tracked, but not the fate of the active incorporated drug. Scintigraphy, however, can be applied to image the distribution pattern of inhaled drugs [217].

The FRET technology shows the potential to give more insights into the fate of nanocarriers in the lung tissue as it can track the direct interactions with liposomal shells [174]. This also might give an enhanced view, which barrier in the lung opens the liposomes and where exactly the drug is released.

6.7 Evaluation of Ptx-NP as a therapeutic option for pulmonary hypertension (PAH)

Besides the pharmacokinetics, we also aimed to evaluate the efficacy of Ptx-NP with the physiological cell model of the pulmonary air-blood barrier consisting of A549-Luc(IL-8) and EA.hy926 cells as Ptx-NP are currently in the preclinical development for the therapy of PAH. Two significant findings in the present work confirmed the potential of the model to test the efficacy of aerosolized drugs for PAH treatment.

First, the addition of endothelial EA.hy926 cells significantly increased the intracellular Ptx levels (figure 5.25) in comparison to the control setup, where only A549-Luc(IL-8) cells were exposed to Ptx-NP. As endothelial cells are target cells of pulmonary hypertension [200], cellular Ptx association is in favor.

Secondly, genes, which are downregulated in PAH [19], were upregulated in EA.hy926 cells after Ptx-NP exposure of the *in vitro* model, most importantly FOXO1 and FOXO3. Moreover, SOD2 was upregulated in endothelial cells after Ptx-NP exposure, which is in favor of the observations made with SOD2 in PAH. Single nucleotide polymorphism analysis of SOD2 in a study carried out by Xu et al. (2017) showed that reduction of SOD expression, which is linked to increased oxidative stress, was associated with the development of pulmonary hypertension [218]. In addition, SOD2-deficient myeloid cells were shown to promote the hyper-proliferative PAH phenotype of human arterial smooth muscle cells [219]. Likewise, the activation of GADD45 confirmed the therapeutic potential of Ptx-NP. The DNA-damage inducible GADD45B gene was found to be decreased in primary arterial endothelial cells isolated from pulmonary hypertension patients [220]. Furthermore, phosphorylation of the GADD45 protein was decreased in primary arterial smooth muscle cells isolated from PAH patients [221].

All in all, the results showed that the air-blood barrier *in vitro* model (A549-Luc(IL-8) cells as epithelium and EA.hy926 cells as endothelium) could be used to study the efficacy of Ptx-NP in the field of PAH. In terms of simplicity, this model is advantageous compared to approaches that rely on the use of primary human material [19].

6.8 Estimation of toxicity onset in rats based on *in vitro* data

Although Ptx-NP showed efficacy in terms of gene upregulation and cellular storage, toxicity was found, i.e., cell viability was reduced to about 50% for 6.4 µg Ptx/cm² (both formulations) and for 3.8 µg Ptx/cm² (slow-releasing only). The experiments with placebo Ptx-NP (fast-releasing) indicated that this could be attributed to the nanoparticles, not to the Ptx loading. As the next step in following preclinical studies would be the application of Ptx-NP to rats by inhalation or instillation, an estimation of the toxicity onset in rats based on *in vitro* data will be given. Moreover, this approach will also allow estimating the therapeutic window.

As mentioned, a decrease in metabolic activity was found for a dose of 6.4 µg Ptx/cm² or 118 µg Ptx-NP/cm², respectively. Ding et al. (2020) reported that a dose of 0.86 cm²/cm² zinc oxide (ZnO) (surface area/cell growth area) led to a decrease in the cell viability by 50% [93]. Schmid et al. (2016) reported an onset of inflammatory processes in rats after ZnO instillation for a dose of 15 cm²/g [222]. 1 g of a rat lung typically refers to a surface area of 3000 cm², taking into account a rat lung surface area of 4000 cm² and a lung weight of 1.3 g [167]. Therefore, 15 cm²/g refers to a ZnO dose per lung surface area of 0.005 cm²/cm². Thus, the onset of toxicity after ZnO exposure *in vitro* is achieved by a 172-fold increased dose as compared to *in vivo*. Based on these observations, an *in vitro*-*in vivo*-extrapolation (IVIVE) factor of 100 – 1000 can be estimated. With this IVIVE factor, a rat bodyweight of 300 g ([167]), and a rat lung surface area of 4000 cm² ([167]), an onset of adverse (inflammatory) effects may have to be expected for a dose of 1.6 – 16 mg/kg if Ptx-NP are administered via instillation into rats (e.g. by micro sprayer application).

This approach can also be applied to estimate the therapeutic window. The *in vitro* gene regulation profile of Ptx-NP was similar to that observed by a mouse model of idiopathic pulmonary arterial hypertension (IPAH) [19]. FoxO1 upregulation in EA.hy926 cells was found for a nominal dose of 1 – 3 µg/cm². Onset of therapeutic efficacy in rat PAH models can hence be expected for 0.34 – 3.4 mg/kg if Ptx-NP are administered via instillation. However, the *in vitro* data suggest that the therapeutic window of Ptx-NP may appear to be relatively narrow (1 – 3 µg/cm²). This would have to be further substantiated by exploring the onset dose for therapeutic efficacy in the following steps. Nevertheless, the applied approach has the potential to find starting doses for following preclinical studies with a focus on toxicity and onset of efficacy.

6.9 Comparison of polymeric and liposomal nanocarriers

As described, the two types of nanodrugs (L-CsA, Ptx-NP) showed a high degree of similarity with regard to particokinetics. However, some differences were obtained, which are summarized in table 6.1 and discussed below.

Table 6.1: Comparison of liposomal and polymeric nanocarriers

	Liposomal nanocarrier	Polymeric nanocarrier
Viability	No observation of toxicity[68]*	Observation of toxicity*
Adverse effects on the barrier integrity of the cells	No	No
Transport at ALI conditions	Burst-like	Burst-like
PDI after nebulization	Monodisperse 0.283	Monodisperse 0.100
Volume-based particle diameter	130 nm	160 – 200 nm
Asymptotic value (A549-Luc(IL-8) cells)	88%	30% (Ptx-NP slow) 65% (Ptx-NP fast)
Release in basal medium in intact form	No	No
Transport pathway (A549-Luc(IL-8) cells)	Caveolae-mediated Endocytosis	Caveolae-mediated endocytosis
Release of molecular drug required?	Yes	Yes

* With 15.1% (w/v), the L-CsA stock solution was even 3.8-fold higher concentrated as the Ptx-NP stock solution and consequently led to higher cell-delivered doses

While toxic effects were observed for polymeric nanocarrier, adverse effects of L-CsA on cellular viability were not reported by Schmid et al. (2017) [68].

Liposomes were characterized by smaller particle size as compared to the polymeric particles. Although nanocarriers show great advantages such as prolonged effects [15], the demonstration of non-toxic effects is the more important step in the development [223]. As shown, this can be evaluated by simple *in vitro* models of the air-blood barrier.

The transport profile obtained by A549-Luc(IL-8) cells demonstrated burst-like transport for both of the particles. Nevertheless, the asymptotic value (transport after 24 h) for the polymeric particles was below the value for the liposomes, indicating accelerated transport for liposomes.

Caveolae-mediated endocytosis was involved in the uptake of both nanocarriers. Interestingly, paracellular transport played a role for the drug loading of polymeric particles when the A549-Luc(IL-8) cell setup was extended to a coculture model with the endothelial cell line EA.hy926.

The Ptx-NP remained stable during the aerosolization process. In contrast to this, a slight degradation of liposomes was measured by an increase of the polydispersity index (PDI) (data not shown), which is a direct measure for the distribution of the particles [175]. However, the PDI after the nebulization was still in an acceptable range (< 0.3 [176]) for aerosolized delivery of liposomal drug formulations.

In summary, the transport profiles for both drug carrier systems showed remarkable similarities.

6.10 Limitations

Given limitations of this study include

a) Clarifying the contributions of each cell line on the transbarrier transport of the nanodrugs
b) *In vivo* validation of the observed higher paracellular transport kinetics for the epithelial-endothelial coculture
c) Limited tight junction expression by A549 cells
d) PK can be modeled with literature data but not predicted because of a missing loss compartment

These could be extended by

a) Aerosolization of the free drugs (CsA and Ptx) – however, this is challenging due to the limited drug solubility and the fact that they could bind to media ingredients, especially fetal calf serum, more preferentially.
b) PK studies in animal experiments. This thesis used epithelial transport rates to match the PK of a slow and a fast-releasing Ptx-NP formulation. If there are comparable c_{max} values after the application to animals, the enhanced paracellular permeability of the coculture has *in vivo* impact
c) Use of alternative cell lines. However, the nanodrugs were not transported by the paracellular transport pathway of A549 cells, but showed strong cell-association. Thus, A549 cells are a suitable cell line to match *in vitro* and *in vivo* PK. The successful use of A549 cells to predict relevant *in vivo* parameters has also been reported by Bachler et al. (2015) [52]
d) Use of microfluidic devices to simulate drug clearance *in vitro*, as described by Frost et al. (2020) [224]

7 Conclusions

Aerosolized delivery of nanodrugs to ALI cultured *in vitro* cell models of the alveolar air-blood barrier with the VITROCELL® Cloud 6 system revealed that

- Cellular transport studies on Transwell® inserts of nanocarriers need to include a membrane-only control (insert without cells)
- Cellular uptake of nanodrugs plays a significant role in transbarrier transport rates
- Dose finding with *in vitro* models of the air-blood barrier allows for estimating the therapeutic window of nanodrugs
- Cellular models can be used to estimate the onset of toxicity of aerosolized nanodrugs *in vivo*
- Cellular models can be used to select superior formulations of nanocarriers
- Cellular models can be combined with PBPK models to predict the *in vivo* PK of nanodrugs
- Cellular models can be used to confirm the potential of prolonged nanocarrier interaction on the target site, even in inflammatory conditions

8 Outlook

Dose-controlled, aerosolized delivery of drug-loaded nanocarriers focusing on cell-delivered dose at ALI cell culture conditions has the potential for quantitative prediction of therapeutic windows as well as pharmacokinetics and pharmacodynamics of drugs in animals and humans.

This can significantly reduce the risk of failure of drugs in both animal toxicology studies and clinical studies.

9 References

1. Kuzmov, A. and T. Minko, *Nanotechnology approaches for inhalation treatment of lung diseases.* J Control Release, 2015. **219**: p. 500-518.
2. de Jesus Valle, M.J., et al., *Pulmonary versus systemic delivery of antibiotics: comparison of vancomycin dispositions in the isolated rat lung.* Antimicrob Agents Chemother, 2007. **51**(10): p. 3771-4.
3. Garbuzenko, O.B., et al., *Intratracheal versus intravenous liposomal delivery of siRNA, antisense oligonucleotides and anticancer drug.* Pharm Res, 2009. **26**(2): p. 382-94.
4. Zhao, Y., et al., *Comparison of efficiency of inhaled and intravenous corticosteroid on pregnant women with COPD and the effects on the expression of PCT and hs-CRP.* Exp Ther Med, 2018. **15**(6): p. 4717-4722.
5. Borghardt, J.M., C. Kloft, and A. Sharma, *Inhaled Therapy in Respiratory Disease: The Complex Interplay of Pulmonary Kinetic Processes.* Can Respir J, 2018. **Volume 2018**.
6. Darquenne, C., et al., *Bridging the Gap Between Science and Clinical Efficacy: Physiology, Imaging, and Modeling of Aerosols in the Lung.* J Aerosol Med Pulm Drug Deliv, 2016. **29**(2): p. 107-26.
7. Lipworth, B.J., *Pharmacokinetics of inhaled drugs.* Br J Clin Pharmacol, 1996. **42**: p. 697-705.
8. Shteinberg, M. and J.S. Elborn, *Use of inhaled tobramycin in cystic fibrosis.* Adv Ther, 2015. **32**(1).
9. Doring, G., et al., *Treatment of lung infection in patients with cystic fibrosis: current and future strategies.* J Cyst Fibros, 2012. **11**(6): p. 461-79.
10. Larj, M.J. and E.R. Bleecker, *Therapeutic Responses in Asthma and COPD: Corticosteroids.* Chest, 2004. **126**(2, Supplement): p. 138S-149S.
11. Liang, W., et al., *Pulmonary Delivery of Biological Drugs.* Pharmaceutics, 2020. **12**(11).
12. Yildiz-Pekoz, A. and C. Ehrhardt, *Advances in Pulmonary Drug Delivery.* Pharmaceutics, 2020. **12**(10).
13. Verco, J., et al., *Inhaled Submicron Particle Paclitaxel (NanoPac) Induces Tumor Regression and Immune Cell Infiltration in an Orthotopic Athymic Nude Rat Model of Non-Small Cell Lung Cancer.* J Aerosol Med Pulm Drug Deliv, 2019. **32**(5): p. 266-277.
14. Trapani, A., et al., *Nanocarriers for respiratory diseases treatment: recent advances and current challenges.* Curr Top Med Chem, 2014. **14**(9): p. 1133-47.
15. Segura-Ibarra, V., et al., *Nanotherapeutics for Treatment of Pulmonary Arterial Hypertension.* Front Physiol, 2018. **9**(890).
16. Mitchell, M.J., et al., *Engineering precision nanoparticles for drug delivery.* Nat Rev Drug Discov, 2020.
17. Behr, J., et al., *Lung deposition of a liposomal cyclosporine A inhalation solution in patients after lung transplantation.* J Aerosol Med Pulm Drug Deliv, 2009. **22**(2): p. 121-30.

18. Iacono, A., et al., *A randomised single-centre trial of inhaled liposomal cyclosporine for bronchiolitis obliterans syndrome post-lung transplantation.* ERJ Open Res, 2019. **5**(4).
19. Savai, R., et al., *Pro-proliferative and inflammatory signaling converge on FoxO1 transcription factor in pulmonary hypertension.* Nat Med, 2014. **20**(11): p. 1289-300.
20. Murgia, X., C. de Souza Carvalho, and C.-M. Lehr, *Overcoming the pulmonary barrier: new insights to improve the efficiency of inhaled therapeutics.* European Journal of Nanomedicine, 2014. **6**(3).
21. Gaspar, M., et al., *Inhaled Liposomes-Current Strategies and Future Challenges.* J Biomed Nanotechnol, 2008. **4**(3): p. 245-257.
22. Comets, E., Zohar, S., *A Survey of the Way Pharmacokinetics are Reported in Published Phase I Clinical Trials, with an Emphasis on Oncology.* Clin Pharmacokinet, 2009. **48**(6): p. 387 - 395.
23. Bosquillon, C., et al., *A Comparison of Drug Transport in Pulmonary Absorption Models: Isolated Perfused rat Lungs, Respiratory Epithelial Cell Lines and Primary Cell Culture.* Pharm Res, 2017. **34**(12): p. 2532-2540.
24. EMA, *Guideline on similar biological medicinal products containing monoclonal antibodies - non-clinical and clinical issues (EMA/CHMP/BMWP/403543/2010).* 2012.
25. Chandel, A., et al., *Recent advances in aerosolised drug delivery.* Biomed Pharmacother, 2019. **112**: p. 108601.
26. Patton, J.S., C.S. Fishburn, and J.G. Weers, *The lungs as a portal of entry for systemic drug delivery.* Proc Am Thorac Soc, 2004. **1**(4): p. 338-44.
27. Simon, S.T., et al., *Acceptability and preferences of six different routes of drug application for acute breathlessness: a comparison study between the United Kingdom and Germany.* J Palliat Med, 2012. **15**(12): p. 1374-81.
28. Kreyling, W.G., *Nanoparticles in the lung.* Nat Biotechnol, 2010. **28**(2): p. 1275-6.
29. Forbes, B., et al., *Challenges for inhaled drug discovery and development: Induced alveolar macrophage responses.* Adv Drug Deliv Rev, 2014. **71**: p. 15-33.
30. Rubin, K., et al., *Pulmonary Metabolism of Substrates for Key Drug-Metabolizing Enzymes by Human Alveolar Type II Cells, Human and Rat Lung Microsomes, and the Isolated Perfused Rat Lung Model.* Pharmaceutics, 2020. **12**(2).
31. Gehr, P., M. Bachofen, and E.R. Weibel, *The normal human lung: ultrastructure and morphometric estimation of diffusion capacity.* Respiration Physiology, 1978. **32**(2): p. 121-140.
32. Labiris, N.R. and M.B. Dolovich, *Pulmonary drug delivery. Part I: physiological factors affecting therapeutic effectiveness of aerosolized medications.* Br J Clin Pharmacol, 2003. **56**(6): p. 588-99.
33. Agertoft, L. and S. Pedersen, *Lung deposition and systemic availability of fluticasone Diskus and budesonide Turbuhaler in children.* Am J Respir Crit Care Med, 2003. **168**(7): p. 779-82.
34. Brutsche, M.H., et al., *Comparison of pharmacokinetics and systemic effects of inhaled fluticasone propionate in patients with asthma and*

healthy volunteers: a randomised crossover study. The Lancet, 2000. **356**(9229): p. 556-561.

35. Okusanya, O.O., et al., *Pharmacokinetic and pharmacodynamic evaluation of liposomal amikacin for inhalation in cystic fibrosis patients with chronic pseudomonal infection.* Antimicrob Agents Chemother, 2009. **53**(9): p. 3847-54.
36. Dhand, C., et al., *Role of Size of Drug Delivery Carriers for Pulmonary and Intravenous Administration with Emphasis on Cancer Therapeutics and Lung-Targeted Drug Delivery.* RSC Adv, 2014. **4**: p. 32673 – 32689.
37. Verco, J., et al., *Pharmacokinetic Profile of Inhaled Submicron Particle Paclitaxel (NanoPac((R))) in a Rodent Model.* J Aerosol Med Pulm Drug Deliv, 2019. **32**(2): p. 99-109.
38. Chenthamara, D., et al., *Therapeutic efficacy of nanoparticles and routes of administration.* Biomater Res, 2019. **23**: p. 20.
39. Lee, W.-H., et al., *Inhalation of nanoparticle-based drug for lung cancer treatment: Advantages and challenges.* Asian Journal of Pharmaceutical Sciences, 2015. **10**(6): p. 481-489.
40. Dabbagh, A., et al., *Critical Parameters for Particle-Based Pulmonary Delivery of Chemotherapeutics.* J Aerosol Med Pulm Drug Deliv, 2018. **31**(3): p. 139-154.
41. Emami, F., S.J. Mostafavi Yazdi, and D.H. Na, *Poly(lactic acid)/poly(lactic-co-glycolic acid) particulate carriers for pulmonary drug delivery.* Journal of Pharmaceutical Investigation, 2019. **49**(4): p. 427-442.
42. Ungaro, F., et al., *Engineered PLGA nano- and micro-carriers for pulmonary delivery: challenges and promises.* J Pharm Pharmacol, 2012. **64**(9): p. 1217-35.
43. Ahmad, N., et al., *A comparative pulmonary pharmacokinetic study of budesonide using polymeric nanoparticles targeted to the lungs in treatment of asthma.* Artif Cells Nanomed Biotechnol, 2020. **48**(1): p. 749-762.
44. Takeuchi, I., Y. Koshi, and K. Makino, *Drug Delivery Properties of Nanocomposite Particles for Inhalation: Comparison of Drug Concentrations in Lungs and Blood.* In Vivo, 2020. **34**(2): p. 543-547.
45. Letsou, G.V., et al., *Pharmacokinetics of liposomal aerosolized cyclosporine A for pulmonary immunosuppression.* The Annals of Thoracic Surgery, 1999. **68**(6): p. 2044-2048.
46. Arppe, J., et al., *Pulmonary pharmacokinetics of cyclosporin A liposomes.* Int J Pharm, 1998. **161**: p. 205-214.
47. Khanna, C., et al., *Interleukin-2 Liposome Inhalation Therapy Is Safe and Effective for Dogs with Spontaneous Pulmonary Metastases.* Cancer, 1997. **79**(7): p. 1409 - 1421.
48. Hung, O., *Pharmacokinetics of Inhaled Liposome-encapsulated Fentanyl.* Anesthesiology, 1995. **83**(2): p. 277-284.
49. Marier, J.F., J. Lavigne, and M.P. Ducharme, *Pharmacokinetics and Efficacies of Liposomal and Conventional Formulations of Tobramycin after Intratracheal Administration in Rats with Pulmonary Burkholderia cepacia Infection.* Antimicrobial Agents and Chemotherapy, 2002. **46**(12): p. 3776-3781.

50. Saari, S.M., et al., *Regional lung deposition and clearance of 99mTc-labeled beclomethasone-DLPC liposomes in mild and severe asthma.* Chest, 1998. **113**(6): p. 1573-9.
51. Weers, J., et al., *A gamma scintigraphy study to investigate lung deposition and clearance of inhaled amikacin-loaded liposomes in healthy male volunteers.* J Aerosol Med Pulm Drug Deliv, 2009. **22**(2): p. 131-8.
52. Bachler, G., et al., *Translocation of gold nanoparticles across the lung epithelial tissue barrier: Combining in vitro and in silico methods to substitute in vivo experiments.* Part Fibre Toxicol, 2015. **12**(18).
53. Zhuang, X. and C. Lu, *PBPK modeling and simulation in drug research and development.* Acta Pharm Sin B, 2016. **6**(5): p. 430-440.
54. Jones, H. and K. Rowland-Yeo, *Basic concepts in physiologically based pharmacokinetic modeling in drug discovery and development.* CPT Pharmacometrics Syst Pharmacol, 2013. **2**(8).
55. El-Masri, H.A., et al., *Development of an inhalation physiologically based pharmacokinetic (PBPK) model for 2,2, 4-trimethylpentane (TMP) in male Long-Evans rats using gas uptake experiments.* Inhal Toxicol, 2009. **21**(14): p. 1176-85.
56. Weber, B. and G. Hochhaus, *A pharmacokinetic simulation tool for inhaled corticosteroids.* AAPS J, 2013. **15**(1): p. 159-71.
57. Walker, D.K., *The use of pharmacokinetic and pharmacodynamic data in the assessment of drug safety in early drug development.* Br J Clin Pharmacol, 2004. **58**(6): p. 601-8.
58. Boger, E. and O. Wigstrom, *A Partial Differential Equation Approach to Inhalation Physiologically Based Pharmacokinetic Modeling.* CPT Pharmacometrics Syst Pharmacol, 2018. **7**(10): p. 638-646.
59. Martin, A.R. and W.H. Finlay, *Model Calculations of Regional Deposition and Disposition for Single Doses of Inhaled Liposomal and Dry Powder Ciprofloxacin.* J Aerosol Med Pulm Drug Deliv, 2018. **31**(1): p. 49-60.
60. Campbell, J., et al., *A preliminary regional PBPK model of lung metabolism for improving species dependent descriptions of 1,3-butadiene and its metabolites.* Chem Biol Interact, 2015. **238**: p. 102-10.
61. Borghardt, J.M., et al., *Pharmacometric Models for Characterizing the Pharmacokinetics of Orally Inhaled Drugs.* AAPS J, 2015. **17**(4): p. 853-70.
62. Paur, H.-R., et al., *In-vitro cell exposure studies for the assessment of nanoparticle toxicity in the lung—A dialog between aerosol science and biology.* Journal of Aerosol Science, 2011. **42**(10): p. 668-692.
63. Upadhyay, S. and L. Palmberg, *Air-Liquid Interface: Relevant In Vitro Models for Investigating Air Pollutant-Induced Pulmonary Toxicity.* Toxicol Sci, 2018. **164**(1): p. 21-30.
64. Arumugasaamy, N., et al., *In Vitro Models for Studying Transport Across Epithelial Tissue Barriers.* Ann Biomed Eng, 2019. **47**(1): p. 1-21.
65. Yeste, J., et al., *Engineering and monitoring cellular barrier models.* J Biol Eng, 2018. **12**(18).
66. Bur, M. and C.M. Lehr, *Pulmonary cell culture models to study the safety and efficacy of innovative aerosol medicines.* Expert Opin Drug Deliv, 2008. **5**(6): p. 641-52.

67. Mathia, N.R., et al., *Permeability characteristics of calu-3 human bronchial epithelial cells: in vitro-in vivo correlation to predict lung absorption in rats.* J Drug Target, 2002. **10**(1): p. 31-40.
68. Schmid, O., et al., *Biokinetics of Aerosolized Liposomal Ciclosporin A in Human Lung Cells In Vitro Using an Air-Liquid Cell Interface Exposure System.* J Aerosol Med Pulm Drug Deliv, 2017. **30**(6): p. 411-424.
69. Salomon, J.J., et al., *The cell line NCl-H441 is a useful in vitro model for transport studies of human distal lung epithelial barrier.* Mol Pharm, 2014. **11**(3): p. 995-1006.
70. Kuehn, A., et al., *Human alveolar epithelial cells expressing tight junctions to model the air-blood barrier.* ALTEX, 2016. **33**(3): p. 251-60.
71. Grainger, C.I., et al., *Culture of Calu-3 cells at the air interface provides a representative model of the airway epithelial barrier.* Pharm Res, 2006. **23**(7): p. 1482-90.
72. Grainger, C.I., et al., *The permeability of large molecular weight solutes following particle delivery to air-interfaced cells that model the respiratory mucosa.* Eur J Pharm Biopharm, 2009. **71**(2): p. 318-24.
73. Trammer, B., et al., *Comparative permeability and diffusion kinetics of cyclosporine A liposomes and propylene glycol solution from human lung tissue into human blood ex vivo.* Eur J Pharm Biopharm, 2008. **70**(3): p. 758-64.
74. Meindl, C., et al., *Permeation of Therapeutic Drugs in Different Formulations across the Airway Epithelium In Vitro.* PLoS One, 2015. **10**(8): p. e0135690.
75. Barakat, A., et al., *In Vitro–In Vivo Correlation: Shades on Some Non-Conventional Dosage Forms.* Dissolution Technologies, 2015. **22**(2): p. 19-22.
76. Newman, S.P. and H.K. Chan, *In vitro/in vivo comparisons in pulmonary drug delivery.* J Aerosol Med Pulm Drug Deliv, 2008. **21**(1): p. 77-84.
77. Frohlich, E., *Biological Obstacles for Identifying In Vitro-In Vivo Correlations of Orally Inhaled Formulations.* Pharmaceutics, 2019. **11**(7).
78. Klein, S.G., et al., *An improved 3D tetraculture system mimicking the cellular organisation at the alveolar barrier to study the potential toxic effects of particles on the lung.* Part Fibre Toxicol, 2013. **10**(31).
79. Fizesan, I., et al., *In vitro exposure of a 3D-tetraculture representative for the alveolar barrier at the air-liquid interface to silver particles and nanowires.* Part Fibre Toxicol, 2019. **16**(14).
80. Rothen-Rutishauser, B.M., S.G. Kiama, and P. Gehr, *A three-dimensional cellular model of the human respiratory tract to study the interaction with particles.* Am J Respir Cell Mol Biol, 2005. **32**(4): p. 281-9.
81. Barosova, H., et al., *Multicellular Human Alveolar Model Composed of Epithelial Cells and Primary Immune Cells for Hazard Assessment.* Journal of Visualized Experiments, 2020. **159**: p. e61090.
82. Barosova, H., et al., *Use of EpiAlveolar Lung Model to Predict Fibrotic Potential of Multiwalled Carbon Nanotubes.* ACS Nano, 2020. **14**(4): p. 3941-3956.
83. Jud, C., et al., *Ultrathin Ceramic Membranes as Scaffolds for Functional Cell Coculture Models on a Biomimetic Scale.* Biores Open Access, 2015. **4**(1): p. 457-68.

84. Horvath, L., et al., *Engineering an in vitro air-blood barrier by 3D bioprinting.* Sci Rep, 2015. **5**(7974).
85. Nonaka, P.N., et al., *Lung bioengineering: physical stimuli and stem/progenitor cell biology interplay towards biofabricating a functional organ.* Respir Res, 2016. **17**(1).
86. Frost, T.S., et al., *Permeability of Epithelial/Endothelial Barriers in Transwells and Microfluidic Bilayer Devices.* Micromachines (Basel), 2019. **10**(8).
87. Ehrmann, S., et al., *Innovative preclinical models for pulmonary drug delivery research.* Expert Opinion on Drug Delivery, 2020. **17**(4): p. 463-478.
88. Lenz, A.G., et al., *A dose-controlled system for air-liquid interface cell exposure and application to zinc oxide nanoparticles.* Part Fibre Toxicol, 2009. **6**(32).
89. Lenz, A.G., et al., *Efficient bioactive delivery of aerosolized drugs to human pulmonary epithelial cells cultured in air-liquid interface conditions.* Am J Respir Cell Mol Biol, 2014. **51**(4): p. 526-35.
90. Ghio, A., et al., *Growth of human bronchial epithelial cells at an air-liquid interface alters the response to particle exposure.* Part Fibre Toxicol, 2013. **10**(25).
91. Mills-Goodlet, R., et al., *Biological effects of allergen–nanoparticle conjugates: uptake and immune effects determined on hAELVi cells under submerged vs. air–liquid interface conditions.* Environmental Science: Nano, 2020. **7**(7): p. 2073-2086.
92. Rohm, M., et al., *A comprehensive screening platform for aerosolizable protein formulations for intranasal and pulmonary drug delivery.* Int J Pharm, 2017. **532**(1): p. 537-546.
93. Ding, Y., et al., *Quartz crystal microbalances (QCM) are suitable for real-time dosimetry in nanotoxicological studies using VITROCELL(R)Cloud cell exposure systems.* Part Fibre Toxicol, 2020. **17**(44).
94. van Riet, S., et al., *In vitro modelling of alveolar repair at the air-liquid interface using alveolar epithelial cells derived from human induced pluripotent stem cells.* Sci Rep, 2020. **10**.
95. Pezzulo, A., et al., *The air-liquid interface and use of primary cell cultures are important torecapitulate the transcriptional profile of in vivo airway epithelia.* Am J Physiol Lung Cell Mol Physiol, 2010. **300**(1): p. 25-31.
96. Vermette, D., et al., *Tight junction structure, function, and assessment in the critically ill: a systematic review.* Intensive Care Med Exp, 2018. **6**(37).
97. Overgaard, C.E., L.A. Mitchell, and M. Koval, *Roles for claudins in alveolar epithelial barrier function.* Ann N Y Acad Sci, 2012. **1257**: p. 167-74.
98. Hartsock, A. and W.J. Nelson, *Adherens and tight junctions: structure, function and connections to the actin cytoskeleton.* Biochim Biophys Acta, 2008. **1778**(3): p. 660-9.
99. Sidhaye, V., et al., *Pulmonary epithelial barrier function: some new players and mechanisms.* Am J Physiol Lung Cell Mol Physiol, 2015. **308**: p. 731-45.

100. Thorley, A.J., et al., *Critical Determinants of Uptake and Translocation of Nanoparticles by the Human Pulmonary Alveolar Epithelium.* ACS Nano, 2014. **8**(11): p. 11778-89.
101. Engelberg, S., et al., *Cancer Cell-Selective, Clathrin-mediated Endocytosis of Aptamer-Decorated Nanoparticles.* Oncotarget, 2018. **9**(30): p. 20993–21006.
102. Auffinger, B., et al., *Drug-Loaded Nanoparticle Systems and Adult Stem Cells: A Potential Marriage for the Treatment of Malignant Glioma?* Oncotarget, 2013. **4**(3): p. 378-96.
103. Kiss, A.L. and E. Botos, *Endocytosis via caveolae: alternative pathway with distinct cellular compartments to avoid lysosomal degradation?* Journal of Cellular and Molecular Medicine, 2009. **13**(7): p. 1228-37.
104. Foroozandeh, P. and A.A. Aziz, *Insight into Cellular Uptake and Intracellular Trafficking of Nanoparticles.* Nanoscale Research Letters, 2018. **13**(1).
105. Hillaireau, H. and P. Couvreur, *Nanocarriers' entry into the cell: relevance to drug delivery.* Cellular and Molecular Life Sciences, 2009. **66**(17): p. 2873-2896.
106. Ahsan, F., et al., *Targeting to macrophages: role of physicochemical properties of particulate carriers — liposomes and microspheres — on the phagocytosis by macrophages.* J Control Release, 2002. **79**(1-3): p. 29-40.
107. Laksitorini, M., et al., *Pathways and progress in improving drug delivery through the intestinal mucosa and blood-brain barriers.* Ther Deliv, 2014. **5**(10): p. 1143-63.
108. Kuhn, D.A., et al., *Different endocytotic uptake mechanisms for nanoparticles in epithelial cells and macrophages.* Beilstein J Nanotechnol, 2014. **5**: p. 1625-36.
109. Rejman, J., et al., *Size-Dependent Internalization of Particles via the Pathways of Clathrin- and Caveolae-Mediated Endocytosis.* Biochem. J., 2004. **377**(Pt 1): p. 159-69.
110. Shang, L., et al., *Engineered nanoparticles interacting with cells: size matters.* J. Nanobiotechnology, 2014. **12**(5).
111. Alshehri, A., A. Grabowska, and S. Stolnik, *Pathways of cellular internalisation of liposomes delivered siRNA and effects on siRNA engagement with target mRNA and silencing in cancer cells.* Scientific Reports, 2018. **8**(1).
112. Wu, M., et al., *Antilung cancer effect of ergosterol and cisplatin-loaded liposomes modified with cyclic arginine-glycine-aspartic acid and octa-arginine peptides.* Medicine, 2018. **97**(33): p. e11916.
113. Wang, R.-H., et al., *Efficacy of dual-functional liposomes containing paclitaxel for treatment of lung cancer.* Oncology Reports, 2015. **33**(2): p. 783-91.
114. Sharma, R., C. Young, and J. Neu, *Molecular modulation of intestinal epithelial barrier: contribution of microbiota.* J Biomed Biotechnol, 2010. **2010**(305879).
115. Singh, A.B., A. Sharma, and P. Dhawan, *Claudin family of proteins and cancer: an overview.* J Oncol, 2010. **2010**.

116. Mazzon, E. and S. Cuzzocrea, *Role of TNF-alpha in lung tight junction alteration in mouse model of acute lung inflammation.* Respir Res, 2007. **8**(75).
117. Lin, X., et al., *beta1-Na(+),K(+)-ATPase gene therapy upregulates tight junctions to rescue lipopolysaccharide-induced acute lung injury.* Gene Ther, 2016. **23**(6): p. 489-99.
118. Eutamene, H., et al., *LPS-induced lung inflammation is linked to increased epithelial permeability: role of MLCK.* Eur Respir J, 2005. **25**(5): p. 789-96.
119. Wittekindt, O.H., *Tight junctions in pulmonary epithelia during lung inflammation.* Pflugers Arch, 2017. **469**(1): p. 135-147.
120. Ren, X., R.A. Johns, and W.D. Gao, *EXPRESS: Right Heart in Pulmonary Hypertension: From Adaptation to Failure.* Pulm Circ, 2019. **9**(3).
121. Lai, Y.C., et al., *Pulmonary arterial hypertension: the clinical syndrome.* Circ Res, 2014. **115**(1): p. 115-30.
122. Dabral, S., et al., *Notch1 signalling regulates endothelial proliferation and apoptosis in pulmonary arterial hypertension.* Eur Respir J, 2016. **48**(4): p. 1137-1149.
123. Ranchoux, B., et al. , *Molecular Mechanisms of Congenital Heart Disease and Pulmonary Hypertension*, ed. T. Nakanishi, et al. 2020, Singapore: SpringerOpen.
124. Taddei, A., et al., *Endothelial adherens junctions control tight junctions by VE-cadherin-mediated upregulation of claudin-5.* Nat Cell Biol, 2008. **10**(8): p. 923-34.
125. Dalmasso, A.P., et al., *Interleukin-4 induces up-regulation of endothelial cell claudin-5 through activation of FoxO1: role in protection from complement-mediated injury.* J Biol Chem, 2014. **289**(2): p. 838-47.
126. Jang, A.S., et al., *Endothelial dysfunction and claudin 5 regulation during acrolein-induced lung injury.* Am J Respir Cell Mol Biol, 2011. **44**(4): p. 483-90.
127. Pullamsetti, S.S., et al., *Inflammation, immunological reaction and role of infection in pulmonary hypertension.* Clin Microbiol Infect, 2011. **17**(1): p. 7-14.
128. Groth, A., et al., *Inflammatory cytokines in pulmonary hypertension.* Respir Res, 2014. **15**(1).
129. Soon, E., et al., *Elevated levels of inflammatory cytokines predict survival in idiopathic and familial pulmonary arterial hypertension.* Circulation, 2010. **122**(9): p. 920-7.
130. Budhiraja, R., R.M. Tuder, and P.M. Hassoun, *Endothelial dysfunction in pulmonary hypertension.* Circulation, 2004. **109**(2): p. 159-65.
131. Dutzmann, J., et al., *Emerging translational approaches to target STAT3 signalling and its impact on vascular disease.* Cardiovasc Res, 2015. **106**(3): p. 365-74.
132. Al Zaid Siddiquee, K. and J. Turkson, *STAT3 as a target for inducing apoptosis in solid and hematological tumors.* Cell Res, 2008. **18**(2): p. 254-67.
133. Zhou, C., *Endothelial hyperpermeability in severe pulmonary arterial hypertension: role of store-operated calcium entry.* Am J Physiol Lung Cell Mol Physiol, 2016. **311**: p. 560-69.

134. Guipaud, O., et al., *The importance of the vascular endothelial barrier in the immune-inflammatory response induced by radiotherapy.* Br J Radiol, 2008. **91**(1089).
135. Wallez, Y. and P. Huber, *Endothelial adherens and tight junctions in vascular homeostasis, inflammation and angiogenesis.* Biochim Biophys Acta, 2008. **1778**(3): p. 794-809.
136. Yun, J.H., et al., *Endothelial STAT3 Activation Increases Vascular Leakage Through Downregulating Tight Junction Proteins: Implications for Diabetic Retinopathy.* J Cell Physiol, 2017. **232**(5): p. 1123-1134.
137. Clark, P.R., et al., *Tumor necrosis factor disrupts claudin-5 endothelial tight junction barriers in two distinct NF-kappaB-dependent phases.* PLoS One, 2015. **10**(3): p. e0120075.
138. Mahler, G.J., E.J. Farrar, and J.T. Butcher, *Inflammatory cytokines promote mesenchymal transformation in embryonic and adult valve endothelial cells.* Arterioscler Thromb Vasc Biol, 2013. **33**(1): p. 121-30.
139. Yu, H., et al., *Interleukin-8 regulates endothelial permeability by down-regulation of tight junction but not dependent on integrins induced focal adhesions.* Int J Biol Sci, 2013. **9**(9): p. 966-79.
140. Kampan, N.C., et al., *Paclitaxel and Its Evolving Role in the Management of Ovarian Cancer.* Biomed Res Int, 2015. **2015**(413076).
141. Feng, W., et al., *Paclitaxel alleviates monocrotaline-induced pulmonary arterial hypertension via inhibition of FoxO1-mediated autophagy.* Naunyn Schmiedebergs Arch Pharmacol, 2019. **392**(5): p. 605-613.
142. Zhao, J., et al., *Effects of paclitaxel intervention on pulmonary vascular remodeling in rats with pulmonary hypertension.* Exp Ther Med, 2019. **17**(2): p. 1163-1170.
143. Koshkina, N., et al., *Paclitaxel Liposome Aerosol Treatment Induces Inhibition of Pulmonary Metastases in Murine Renal Carcinoma Model.* Clin Cancer Res, 2001. **7**(7): p. 3258-3263.
144. Joshi, N., et al., *Endogenous lung surfactant inspired pH responsive nanovesicle aerosols: pulmonary compatible and site-specific drug delivery in lung metastases.* Sci Rep, 2014. **4**.
145. Joshi, N., A. Kaviratna, and R. Banerjee, *Multi trigger responsive, surface active lipid nanovesicle aerosols for improved efficacy of paclitaxel in lung cancer.* Integr Biol (Camb), 2013. **5**(1): p. 239-48.
146. Alipour, S., H. Montaseri, and M. Tafaghodi, *Inhalable, large porous PLGA microparticles loaded with paclitaxel: preparation, in vitro and in vivo characterization.* J Microencapsul, 2015. **32**(7): p. 661-8.
147. Yuksel, H. and A. Turkeli, *Airway epithelial barrier dysfunction in the pathogenesis and prognosis of respiratory tract diseases in childhood and adulthood.* Tissue Barriers, 2017. **5**(4): p. e1367458.
148. Sato, M., *Bronchiolitis obliterans syndrome and restrictive allograft syndrome after lung transplantation: why are there two distinct forms of chronic lung allograft dysfunction?* Ann Transl Med, 2020. **8**(6): p. 418.
149. Lin, C.M. and M.R. Zamora, *Update on Bronchiolitis Obliterans Syndrome in Lung Transplantation.* Curr Transplant Rep, 2014. **1**(4): p. 282-289.
150. Hodge, S., et al., *Posttransplant bronchiolitis obliterans syndrome is associated with bronchial epithelial to mesenchymal transition.* Am J Transplant, 2009. **9**(4): p. 727-33.

151. Borthwick, L.A., et al., *TNFalpha from classically activated macrophages accentuates epithelial to mesenchymal transition in obliterative bronchiolitis.* Am J Transplant, 2013. **13**(3): p. 621-33.
152. Tsukita, S., et al., *Regulation of tight junctions during the epithelium-mesenchyme transition: direct repression of the gene expression of claudins/occludin by Snail.* J Cell Sci, 2003. **115**: p. 1959-1976.
153. Martin, T.A. and W.G. Jiang, *Loss of tight junction barrier function and its role in cancer metastasis.* Biochim Biophys Acta, 2009. **1788**(4): p. 872-91.
154. Bhat, A.A., et al., *Tight Junction Proteins and Signaling Pathways in Cancer and Inflammation: A Functional Crosstalk.* Front Physiol, 2018. **9**(1942).
155. Barker, A.F., et al., *Obliterative bronchiolitis.* N Engl J Med, 2014. **370**(19): p. 1820-8.
156. Kallen, J., et al., *X-ray Structures and Analysis of 11 Cyclosporin Derivatives Complexed with Cyclophilin A.* J Mol Biol, 1998. **283**(2): p. 435-49.
157. Kawasaki, H., et al., *Cyclosporine inhibits mouse cytomegalovirus infection via a cyclophilin-dependent pathway specifically in neural stem/progenitor cells.* J Virol, 2007. **81**(17): p. 9013-23.
158. Corcoran, T.E., et al., *Lung deposition and pharmacokinetics of nebulized cyclosporine in lung transplant patients.* J Aerosol Med Pulm Drug Deliv, 2014. **27**(3): p. 178-84.
159. Stoehr, L.C., et al., *Assessment of a panel of interleukin-8 reporter lung epithelial cell lines to monitor the pro-inflammatory response following zinc oxide nanoparticle exposure under different cell culture conditions.* Part Fibre Toxicol, 2015. **12**(29).
160. Li, D., et al., *Loss of integrity of doxorubicin liposomes during transcellular transportation evidenced by fluorescence resonance energy transfer effect.* Colloids Surf B Biointerfaces, 2018. **171**: p. 224-232.
161. Gessler, T., et al., *Biokompatible Nanopolymerpartikel mit Wirkstoffen für die pulmonale Applikation. WO2012/160085AI.* 2012.
162. Stoehr, L.C., et al., *Assessment of a panel of interleukin-8 reporter lung epithelial cell lines to monitor the pro-inflammatory response following zinc oxide nanoparticle exposure under different cell culture conditions.* Part Fibre Toxicol, 2015. **12**: p. 29.
163. Lehmann, A.D., et al., *Diesel exhaust particles modulate the tight junction protein occludin in lung cells in vitro.* Part Fibre Toxicol, 2009. **6**(26).
164. Hinderliter, P., et al., *ISDD: A computational model of particle sedimentation, diffusion and target cell dosimetry for in vitro toxicity* Part Fibre Toxicol, 2010. **7**(36).
165. Vauthier, C., et al., *Measurement of the density of polymeric nanoparticulate drug carriers by isopycnic centrifugation.* J Nanopart Res, 1999. **1**: p. 411-418.
166. Kappeler, D., et al., *Liposomal Cyclosporine A for Inhalation (L-CsA-i) to treat Bronchiolitis Obliterans Syndrome: Novel Formulation and Drug-Specific Delivery System Improve Tolerability. Orlando: ISHLT 39th Annual Meeting and Scientific Sessions. Available from: breath-therapeutics.com.* 2020.

167. Birnbaum, L., et al., *Physiological Parameter Values for PBPK Models*. 1994, Washington, DC: International Life Sciences Institute Risk Science Institute.
168. Yu, C.P. and C.K. Diu, *A Probabilistic Model for Intersubject Deposition Variability of Inhaled Particles.* Aerosol Science and Technology, 2007. **1**(4): p. 355-362.
169. Geller, D.E., et al., *Pharmacokinetics and safety of MP-376 (levofloxacin inhalation solution) in cystic fibrosis subjects.* Antimicrob Agents Chemother, 2011. **55**(6): p. 2636-40.
170. Geller, D., et al., *Efficiency of Pulmonary Administration of Tobramycin Solution for Inhalation in Cystic Fibrosis Using an Improved Drug Delivery System.* Chest, 2003. **123**(1): p. 28-36.
171. Touw, D.J., et al., *Pharmacokinetics of aerosolized tobramycin in adult patients with cystic fibrosis.* Antimicrobial Agents and Chemotherapy, 1997. **41**(1): p. 184-187.
172. Clancy, J.P., et al., *Phase II studies of nebulised Arikace in CF patients with Pseudomonas aeruginosa infection.* Thorax, 2013. **68**(9): p. 818-25.
173. Froehlich, J., et al., *Inhaled Liposomal Ciprofloxacin in Patients With Non-Cystic Fibrosis Bronchiectasis and Chronic Pseudomonas aeruginosa Infection: Pharmacokinetics of Once-Daily Inhaled ARD-3150.* Presented at the 2nd World Bronchiectasis Conference, 2017.
174. Chen, T., et al., *Application of Forster Resonance Energy Transfer (FRET) technique to elucidate intracellular and In Vivo biofate of nanomedicines.* Adv Drug Deliv Rev, 2019. **143**: p. 177-205.
175. Stetefeld, J., S.A. McKenna, and T.R. Patel, *Dynamic light scattering: a practical guide and applications in biomedical sciences.* Biophys Rev, 2016. **8**(4): p. 409-427.
176. Danaei, M., et al., *Impact of Particle Size and Polydispersity Index on the Clinical Applications of Lipidic Nanocarrier Systems.* Pharmaceutics, 2018. **10**(2).
177. Wei, F., et al., *Anti-inflammatory mechanism of ulinastatin: Inhibiting the hyperpermeability of vascular endothelial cells induced by TNF-α via the RhoA/ROCK signal pathway.* International Immunopharmacology, 2017. **46**: p. 220-227.
178. Morrell, N.W., et al., *Cellular and molecular basis of pulmonary arterial hypertension.* J Am Coll Cardiol, 2009. **54**(1 Suppl): p. S20-31.
179. Huizing, M.T., et al., *Pharmacokinetics of paclitaxel and three major metabolites in patients with advanced breast carcinoma refractory to anthracycline therapy treated with a 3-hour paclitaxel infusion: a European Cancer Centre (ECC) trial.* Ann Oncol, 1995. **6**(7): p. 699-704.
180. Wang, H., et al., *Establishment and comparison of air-liquid interface culture systems for primary and immortalized swine tracheal epithelial cells.* BMC Cell Biology, 2018. **19**(1).
181. Hilton, G., et al., *Leveraging proteomics to compare submerged versus air-liquid interface carbon nanotube exposure to a 3D lung cell model.* Toxicology in Vitro, 2019. **54**: p. 58-66.
182. Lenz, A.G., et al., *Inflammatory and oxidative stress responses of an alveolar epithelial cell line to airborne zinc oxide nanoparticles at the air-liquid interface: a comparison with conventional, submerged cell-culture conditions.* Biomed Res Int, 2013. **2013**: p. 652632.

183. Loret, T., et al., *Air-liquid interface exposure to aerosols of poorly soluble nanomaterials induces different biological activation levels compared to exposure to suspensions.* Part Fibre Toxicol, 2016. **13**(1): p. 58.
184. Oostingh, G.J., et al., *A high-throughput screening method based on stably transformed human cells was used to determine the immunotoxic effects of fluoranthene and other PAHs.* Toxicol In Vitro, 2008. **22**(5): p. 1301-10.
185. Frohlich, E., *The role of surface charge in cellular uptake and cytotoxicity of medical nanoparticles.* Int J Nanomedicine, 2012. **7**: p. 5577-91.
186. Li, Y., et al., *Lipid rafts-mediated endocytosis and physiology-based cell membrane traffic models of doxorubicin liposomes.* Biochim Biophys Acta, 2016. **1858**(8): p. 1801-11.
187. Andar, A.U., et al., *Microfluidic preparation of liposomes to determine particle size influence on cellular uptake mechanisms.* Pharm Res, 2014. **31**(2): p. 401-13.
188. Yang, J., et al., *Drug Delivery via Cell Membrane Fusion Using Lipopeptide Modified Liposomes.* ACS Cent Sci, 2016. **2**(9): p. 621-630.
189. Rudokas, M., et al., *Liposome Delivery Systems for Inhalation: A Critical Review Highlighting Formulation Issues and Anticancer Applications.* Med Princ Pract, 2016. **25 Suppl 2**: p. 60-72.
190. Doryab, A., et al., *A Bioinspired in vitro Lung Model to Study Particokinetics of Nano-/Microparticles Under Cyclic Stretch and Air-Liquid Interface Conditions.* Frontiers in Bioengineering and Biotechnology, 2021. **9**.
191. Patel, A., et al., *Lung inflammation does not affect the clearance kinetics of lipid nanocapsules following pulmonary administration.* J Control Release, 2016. **235**: p. 24-33.
192. Zambito, Y., C. Zaino, and G. Di Colo, *Effects of N-trimethylchitosan on transcellular and paracellular transcorneal drug transport.* Eur J Pharm Biopharm, 2006. **64**(1): p. 16-25.
193. Omri, A., et al., *Pulmonary retention of free and liposome-encapsulated tobramycin after intratracheal administration in uninfected rats and rats infected with Pseudomonas aeruginosa.* Antimicrob Agents Chemother, 1994. **38**(5): p. 1090-5.
194. Horvath, L., et al., *Engineering an in vitro air-blood barrier by 3D bioprinting.* Sci Rep, 2015. **5**: p. 7974.
195. Deng, F., et al., *Transmembrane Pathways and Mechanisms of Rod-like Paclitaxel Nanocrystals through MDCK Polarized Monolayer.* ACS Appl Mater Interfaces, 2017. **9**(7): p. 5803-5816.
196. Karyekar, C., et al., *Zonula Occludens Toxin Increases the Permeability of Molecular Weight Markers and Chemotherapeutic Agents Across the Bovine Brain Microvessel Endothelial Cells.* J Pharm Sci, 2003. **92**(2): p. 414-423.
197. Cox, D., et al., *Enhancing the permeation of marker compounds and enaminone anticonvulsants across Caco-2 monolayers by modulating tight junctions using zonula occludens toxin* Eur J Pharm Biopharm, 2001. **52**.
198. Klein, S.G., *Model development to evaluate the effects of environmental particles on the lung*, in *Raum- und Umweltwissenschaften*. 2016, Universität Trier: Trier.

199. Weissmann, N., et al., *Activation of TRPC6 channels is essential for lung ischaemia-reperfusion induced oedema in mice.* Nat Commun, 2012. **3**.
200. Humbert, M., et al., *Pathology and pathobiology of pulmonary hypertension: state of the art and research perspectives.* Eur Respir J, 2019. **53**(1).
201. Marinkovic, G., et al., *The Ins and Outs of Small GTPase Rac1 in the Vasculature.* J Pharmacol Exp Ther, 2015. **354**(2): p. 91-102.
202. Sydykov, A., et al., *Inflammatory Mediators Drive Adverse Right Ventricular Remodeling and Dysfunction and Serve as Potential Biomarkers.* Front Physiol, 2018. **9**.
203. Prins, K.W., et al., *Repurposing Medications for Treatment of Pulmonary Arterial Hypertension: What's Old Is New Again.* J Am Heart Assoc, 2019. **8**(1): p. e011343.
204. Hermanns, M.I., et al., *Lung epithelial cell lines in coculture with human pulmonary microvascular endothelial cells: development of an alveolo-capillary barrier in vitro.* Lab Invest, 2004. **84**(6): p. 736-52.
205. Miller, F.J., et al., *Improvements and additions to the Multiple Path Particle Dosimetry model.* Journal of Aerosol Science, 2016. **99**: p. 14-26.
206. Gerde, P., et al., *DissolvIt: An In Vitro Method for Simulating the Dissolution and Absorption of Inhaled Dry Powder Drugs in the Lungs.* ASSAY and Drug Development Technologies, 2017. **15**(2): p. 77-88.
207. Hassoun, M., et al., *Use of PBPK Modeling To Evaluate the Performance of DissolvIt, a Biorelevant Dissolution Assay for Orally Inhaled Drug Products.* Molecular Pharmaceutics, 2019. **16**(3): p. 1245-1254.
208. Stass, H., et al., *Inhalation of a dry powder ciprofloxacin formulation in healthy subjects: a phase I study.* Clin Drug Investig, 2013. **33**(6): p. 419-27.
209. Back, H.-m., et al., *Exposure-Response and Clinical Outcome Modeling of Inhaled Budesonide/Formoterol Combination in Asthma Patients.* Pharmaceutics, 2020. **12**(4).
210. Cordes, H., et al., *A Physiologically Based Pharmacokinetic Model of Isoniazid and Its Application in Individualizing Tuberculosis Chemotherapy.* Antimicrob Agents Chemother, 2016. **60**(10): p. 6134-45.
211. Kurata, T., et al., *Phase I and Pharmacological Study of Paclitaxel Given Over 3 h with Cisplatin for Advanced Non-small Cell Lung Cancer.* Jpn J Clin Oncol, 2001. **31**(3): p. 93-99.
212. Gharse, S., Fiegel, J., *Large Porous Hollow Particles: Lightweight Champions of Pulmonary Drug Delivery.* Curr Pharm Des, 2016. **22**(17): p. 2463-2469.
213. Chrystyn, H., *Methods to identify drug deposition in the lungs following inhalation.* Br J Clin Pharmacol, 2000. **51**: p. 289-299.
214. Stockmann, C., et al., *Development of levofloxacin inhalation solution to treat Pseudomonas aeruginosa in patients with cystic fibrosis.* Ther Adv Respir Dis, 2014. **8**(1): p. 13-21.
215. Loira-Pastoriza, C., J. Todoroff, and R. Vanbever, *Delivery strategies for sustained drug release in the lungs.* Adv Drug Deliv Rev, 2014. **75**: p. 81-91.
216. Strong, P., et al., *Current approaches to the discovery of novel inhaled medicines.* Drug Discov Today, 2018. **23**(10): p. 1705-1717.

217. Hochhaus, G., et al., *Pharmacokinetics of Orally Inhaled Drug Products.* AAPS J, 2015. **17**(3): p. 769-75.
218. Xu, M., et al., *Role for Functional SOD2 Polymorphism in Pulmonary Arterial Hypertension in a Chinese Population.* International Journal of Environmental Research and Public Health, 2017. **14**(3).
219. Fu, C., et al., *SOD2 ameliorates pulmonary hypertension in a murine model of sleep apnea via suppressing expression of NLRP3 in CD11b+ cells.* Respiratory Research, 2020. **21**(1).
220. Rhodes, C.J., et al., *RNA Sequencing Analysis Detection of a Novel Pathway of Endothelial Dysfunction in Pulmonary Arterial Hypertension.* American Journal of Respiratory and Critical Care Medicine, 2015. **192**(3): p. 356-366.
221. Perros, F., et al., *Smooth Muscle Phenotype in Idiopathic Pulmonary Hypertension: Hyper-Proliferative but not Cancerous.* International Journal of Molecular Sciences, 2019. **20**(14).
222. Schmid, O. and T. Stoeger, *Surface area is the biologically most effective dose metric for acute nanoparticle toxicity in the lung.* Journal of Aerosol Science, 2016. **99**: p. 133-143.
223. Moreno-Sastre, M., et al., *Pulmonary drug delivery: a review on nanocarriers for antibacterial chemotherapy.* J Antimicrob Chemother, 2015. **70**(11): p. 2945-55.
224. Frost, T.S., L. Jiang, and Y. Zohar, *Pharmacokinetic Analysis of Epithelial/Endothelial Cell Barriers in Microfluidic Bilayer Devices with an Air-Liquid Interface.* Micromachines (Basel), 2020. **11**(5).

Appendix

1. Simple discrete modeling

Simple discrete modeling was introduced to match *in vitro* Cyclosporine A transport rates with the clearance of CsA from the plasma after inhalation. Clinical data for L-CsA published by Breath Therapeutics GmbH were used to obtain the removal rate of CsA from the blood.

In detail, the translocation of L-CsA across A549-Luc(IL-8) cells after exposure in the VITROCELL® Cloud 6 system was used to calculate the fractional *in vitro* transport rate k_{LB} (A.1-1), i.e. the fraction of the drug transported across the alveolar barrier model per time for a given time layer (index i).

$$k_{LB_i} = \frac{(t_{b_{i+1}} - t_{b_i})}{(t_{i+1} - t_i)} \cdot \frac{1}{r_{(c+a)_i}} \qquad \text{(A.1-1)}$$

i:	index for time points at which data was collected, 0 – 24 h
k_{LB}:	*in vitro* fractional CsA transport rate, h^{-1}
t_b:	*in vitro* transbarrier transported CsA dose (i.e. dose in the basal medium), µg
r_{c+a}:	*in vitro* CsA dose in cell and apical compartment, µg

The fractional removal of CsA from the blood plasma was calculated from published PK studies with L-CsA as fractional loss rate k_{loss} (A.1-2).

$$k_{loss_i} = \frac{c_{i+1} - c_i}{0.5 \cdot (c_{i+1} + c_i)} \cdot \frac{1}{t_i - t_{i+1}} \qquad \text{(A.1-2)}$$

k_{loss}: *in vivo* fractional CsA loss rate from the blood, h^{-1}

c: concentration of CsA in the blood, ng/mL

t: time, h

With these parameters one can now calculate the time course of the drug dose in the lung, where we focus on the dose in the peripheral lung (L_i), which is most relevant for transport from the lung into the blood. At time point zero (directly after end of inhalation), L-CsA in the lung is the fraction of the (nominal) dose in the inhaler multiplied by the lung-deposited fraction ($L_0 = f_{dep}\ D_{nominal}$), which was experimentally determined by Behr et al. (2009) [17], was used where the peripheral L-CsA deposition was measured as 22% of the nominal dose. During each time step (i), the pulmonary dose (L_i) can be calculated from the initially deposited dose (L_0) subtracted by the CsA dose currently present in the blood (V_{Blood}*c_i), and the sum of all of the CsA dose removed from the blood (sum of V_{Blood}(k_{loss}*ci).

$$L_i = f_{dep} \cdot D_{nominal} - V_{Blood} \cdot c_i - \sum_{i=0\ h}^{24\ h} V_{Blood} \cdot (k_{loss} \cdot c_i) \qquad \text{(A.1-3)}$$

L: actual dose of CsA in the lung, µg

f_{dep}: peripheral L-CsA deposition fraction

$D_{nominal}$: L-CsA dose in the inhaler, mg

Similarly, the CsA dose transported from the lung to the blood (m_{LB}) at each time step can be calculated from the *in vitro* lung-blood transport rate (k_{LB}) and the lung dose L_i (from *in vivo* data using equation (A.1-3)).

$$m_{LB_i} = m_{LB_{i-1}} + k_{LB_i} \cdot \frac{r_{(c+a)_{i+1}}}{r_{(c+a)_{0.25h}}} \cdot L_i \cdot (t_i - t_{i-1}) \qquad \text{(A.1-4)}$$

Dividing this time series of CsA doses transported from the lung into the blood per time interval ($\Delta m_{LBi}/\Delta t$) by the total human blood volume finally resulted in the temporal PK profile (CsA serum concentration) of the inhaled drug. Comparison of $m_{LB,i}/V_{Blood}$ with the clinically measured serum concentration allows assessment of the predictive capacity of the *in vitro* transport rate in terms clinical outcome.

2. Advanced PBPK modeling

Blood compartment:

$$\frac{dm_{blood}}{dt} = k_{LB} \cdot m_{lung} - k_{loss} \cdot m_{blood} + k_{RB} \cdot m_{remainder} - k_{BR} \cdot m_{blood} \qquad \text{(A.2-1)}$$

Remainder compartment:

$$\frac{dm_{remainder}}{dt} = k_{BR} \cdot m_{blood} - k_{RB} \cdot m_{remainder} \qquad \text{(A.2-2)}$$

Lung compartment:

$$\frac{dm_{lung}}{dt} = \dot{m}_{dep} - k_{LB} \cdot m_{lung} \qquad \text{(A.2-3)}$$

Loss compartment:

$$\frac{dm_{loss}}{dt} = k_{loss} \cdot m_{loss} \qquad \text{(A.2-4)}$$

m_{lung}: dose in lung compartment after inhalation, mg

m_{blood}: dose in blood compartment after inhalation, mg

m_{loss}: dose in loss compartment after inhalation, mg

$m_{remainder}$: dose in loss compartment after inhalation, mg

$\dot{m}_{dep}$: inhaled dose as a function of inhalation time, mg/min

t: time, min

Table A: Overview on the PBPK parameters

	Value	***in vitro/in vivo***	**Aim**	**Reference**
Alveolar surface area (cm²)	143	*in vivo*	Initial L-CsA dose in the lung	Gehr et al. (1978)
Peripheral L-CsA deposition fraction	0.221	*in vivo*	Initial L-CsA dose in the lung	Behr et al. (2009)
Nominal L-CsA dose (dose in PARI eFlow® inhaler) (mg)	10	*in vivo*	Initial L-CsA dose in the lung	Kappeler et al. (2019)
CsA loss rate (1/h)	0.51	*in vivo*	Calculation of k_{loss}	Kappeler et al. (2019)
Clinical CsA data (serum) (ng/mL)	57.42 (c_{max})	*in vivo*	*in vitro-in vivo*-matching	*Kappeler et al. (2019)*
CsA dose in basal medium (µg)	0 – 10	*in vitro*	Calculation of k_{LB}	-
CsA dose in apical + cell compartment (µg)	10 - 0	*in vitro*	Calculation of k_{LB}	-
Remainder rates (1/h)	fit	*In vivo*	Calculation of k_{BR} and k_{RB}	-
Inhalation time (min)	9	*in vivo*	Calculation of m_{dep}	Behr et al. (2009)
Total human blood volume (mL)	5775	*In vivo*	Calculation of clinical PK data	Birnbaum et al. (1994) [167]

List of abbreviations

ALICE	ALI Cell Exposure
LCI	Live Cell Imaging
SEM	Scanning Electron Microscope
QCM	Quartz Crystal Microbalance
ALI	Air-Liquid Interface
CsA	Cyclosporine A
L-CsA	Liposomal Cyclosporine A
Ptx-NP	Paclitaxel-laden nanoparticles
Ptx	Paclitaxel
TNF-α	Tumor Necrosis Factor-alpha
PDI	Polydispersity Index
DAPI	4′,6-Diamidin-2-phenylindol
DLS	Dynamic Light Scattering
FRET	Fluorescence Resonance Energy Transfer
FCS	Fetal Calf Serum
LDH	Lactate Dehydrogenase
WST-1	Water Soluble Tetrazolium Salt 1
IL-8	Interleukin 8
DAPI	4',6-diamidino-2-phenylindole
BODIPY	Boron-dipyrromethene
PBS	Phosphate buffered saline
DMEM/F-12	Dulbecco’s Modified Eagle Medium/Ham’s F-12 Medium
Luc	Luciferase
f_{dep}	Deposition factor
A_{insert}	Area of the Transwell® insert, cm^2
k_{LB}	*in vitro* obtained lung to blood transport rate
k_{loss}	*in vivo* loss rate
k_{BE}	elimination rate of a drug in the blood
k_{BR}	transport of a drug from the blood into the remainder (rest of the body)
k_{RB}	reflux of the drug from the blood into the remainder

D_{tot}	Dose of an aerosolized drug per Transwell® inserts
r_m	Dose retained by the membrane
r_{c+a}	Dose of an aerosolized drug retained by the cells plus the amount of an aerosolized drug attached to the cells
t_b	transmitted dose into the basal compartment when cells are present
$t_{b,0}$	transmitted dose into the basal compartment for a membrane-only control
ISDD	*In vitro* Sedimentation, Diffusion and Dosimetry model
SD	Standard Deviation
SEM	Standard Error of the Mean
n	number of experiments

Acknowledgments

First of all, I would like to thank my thesis committee members Markus Rehberg, Anne Hilgendorff, Iris Augustin and Otmar Schmid. Your feedback was always very valuable for me and it helped me not only in my career development but also in my personal development. Many thanks go to my students Elias Richter and Ramona Walder. It was a pleasure supporting your projects and teaching you.

Many thanks go to my collaboration partners from the Max-Planck-Institut für Herz- und Lungenforschung and Universität Giessen.

I want to thank Prof. Dr. Iris Augustin who made it possible for me to teach Cell Biology at the University of Applied Sciences Weihenstephan-Triesdorf. It was a pleasure to work with students.

Then, I would like to thank all lab members of the iLBD at the Helmholtz Zentrum München, especially Paula Mayer, Andreas Schröppel, Anna Fuchs, Christina Hollauer, David Kutschke, Verena Häfner, Dr. Aicha Jeridi, Dr. Carmela Morrone, Dr. Tom Conlon and Miriam Kastlmeier for their support and great working atmosphere in the lab. Especially, I would like to thank Dr. Pramod Kumar, Dr. Ali Farnoud, Ali Doryab, and Dr. Yaobo Ding for their scientific feedback and support.

Last but not least, I would like to thank my parents and my sister.

Affidavit

LMU

LUDWIG-
MAXIMILIANS-
UNIVERSITÄT
MÜNCHEN

Promotionsbüro
Medizinische Fakultät

MMRS

Affidavit

Orak, Sezer
____
Surname, first name

Ingolstädter Landstraße 1
____
Street

85764 Munich, Germany
____
Zip code, town, country

I hereby declare, that the submitted thesis entitled:

Bridging gaps between *in vitro* and *in vivo* data in pulmonary aerosol delivery with focus on pharmacokinetics

is my own work. I have only used the sources indicated and have not made unauthorized use of services of a third party. Where the work of others has been quoted or reproduced, the source is always given.

I further declare that the submitted thesis or parts thereof have not been presented as part of an examination degree to any other university.

Munich, 28th October 2021 Sezer Orak
________________________ ________________________
place, date Signature doctoral candidate

Confirmation of congruency

LMU

LUDWIG-
MAXIMILIANS-
UNIVERSITÄT
MÜNCHEN

Promotionsbüro
Medizinische Fakultät

MMRS

Confirmation of congruency between printed and electronic version of the doctoral thesis

Orak, Sezer

Surname, first name

Ingolstädter Landstraße 1

Street

85764 Munich, Germany

Zip code, town, country

I hereby declare, that the submitted thesis entitled:

Bridging gaps between *in vitro* and *in vivo* data in pulmonary aerosol delivery with focus on pharmacokinetics

is congruent with the printed version both in content and format.

Munich, 28th October 2021

place, date

Sezer Orak

Signature doctoral candidate

Supervised projects

During my PhD, I supervised projects, which are not described in this thesis:

Walder, R. *Nebulizing Antifungals and Inducing Converting Enzymes of the Cholesterol Metabolism as Preliminary Experiments to Target COPD* – Biberach University of Applied Sciences, Biberach an der Riß, 2020.

Walder, R. *Inhibiting the Immunometabolism of Cholesterol as Novel Therapeutic Approach to Target COPD* – Biberach University of Applied Sciences, Biberach an der Riß, 2020.

Richter, E. *Experimentelle Charakterisierung eines optimierten Systems zur simulierten Inhalationstherapie für Lungenzellen* – University of Applied Sciences Weihenstephan, Freising, 2019.

List of publications

During my PhD, I contributed to this project, which is not described in this thesis:

Doryab, A., Taskin, M., Stahlhut, P., Schröppel, A., **Orak, S.**, Voss, C., Ahluwalia, A., Rehberg, M., Hilgendorff, A., Stöger, T., Groll, J. and Schmid, O.
A Bioinspired *in vitro* Lung Model to Study Particokinetics of Nano-/Microparticles under Cyclic Stretch and ALI Conditions. (2021) A Bioinspired *in vitro* Lung Model to Study Particokinetics of Nano-/Microparticles Under Cyclic Stretch and Air-Liquid Interface Conditions. Front. Bioeng. Biotechnol. 9:616830. doi: 10.3389/fbioe.2021.

Poster presentations*:*

Orak, S., Rothen-Rutishauser, B., Jud, C., Farnoud, A., Bucholski, A., Egle, R., Boerner, G., Denk, O., Schmid, O.
Towards Prediction of the PK of Inhaled Nanomedicine from Physiological Cell Models: A Case Study with Liposomal Cyclosporine A (L-CsA) using the VITROCELL Cloud System.
22nd ISAM Congress in Montreux, Switzerland, May 2019*

Farnoud, A., **Orak, S.**, Schmid, O.
Numerical Models of Respiratory Drug Deposition and PK: Application to Liposomal Cyclosporine A (L-CsA).
22nd ISAM Congress in Montreux, Switzerland, May 2019*

*Abstracts for these poster presentations were published in the Journal of Aerosol Medicine and Pulmonary Drug Delivery Vol. 32, No. 3

Orak, S., Rothen-Rutishauser, B., Jud, C., Farnoud, A., Bucholski, A., Egle, R., Boerner, G., Denk, O., Schmid, O.

Towards Prediction of the PK of Inhaled Nanomedicine from Physiological Cell Models: A Case Study with Liposomal Cyclosporine A (L-CsA) using the VITROCELL Cloud System.
Meeting of the German Center for Lung Research (DZL), Munich, July 2019